VCSEL-BASED MULTIMODE FIBER OPTICAL LINKS FOR HIGH CAPACITY INTERCONNECTS

A Dissertation
Presented to
The Academic Faculty

by

Justin Lavrencik

In Partial Fulfillment
of the Requirements for the Degree
Doctor of Philosophy in the
School of Electrical and Computer Engineering

Georgia Institute of Technology
[January 2020]

VCSEL-BASED MULTIMODE FIBER OPTICAL LINKS FOR HIGH CAPACITY INTERCONNECTS

Approved by:

Dr. Stephen E. Ralph, Advisor
School of Electrical and Computer Engineering
Georgia Institute of Technology

Dr. Paul D. Yoder
School of Electrical and Computer Engineering
Georgia Institute of Technology

Dr. Benjamin D. B. Klein
School of Electrical and Computer Engineering
Georgia Institute of Technology

Dr. Rick P. Trebino
School of Physics
Georgia Institute of Technology

Dr. Gee-Kung Chang
School of Electrical and Computer Engineering
Georgia Institute of Technology

Date Approved: [January 30, 2020]

To My Parents

ACKNOWLEDGEMENTS

I was privileged with the opportunity to attend Georgia Institute of Technology to work on my graduate degree in semiconductor physics. However, circumstances led to moving more towards photonics. I would like to thank Prof. Stephen Ralph for giving me a chance in his lab to work towards my Ph.D. and introducing me to optics and photonics. His supervising and advice over my years here, led to a deeper understanding of the fundamental physics behind optical communications and its practical implications making this research possible.

I would also like to thank Prof. Doug Yoder, Prof. Ben Klein, and Prof. G.K. Chang. Prof. Yoder for helping me to a better understanding in semiconductor physics and answering all my questions in office hours to help fill gaps in my knowledge from my undergraduate education. Prof. Klein for introducing me to laser diode fundamentals and our many conversations about VCSEL rate equations, modeling, and noise dynamics. And, Prof. G.K. Chang for his lectures over optical communication fundamentals and his encouragement and enthusiasm towards my research. I would also like to thank all the companies and universities who helped with parts and equipment for my research: OFS (with special thanks to Robert Lingle Jr.), Inphi, Thor Labs, Keysight (with special thanks to Gabe Martin and Scott Ferguson), Avago, Finisar, Chalmers University (with special thanks to Prof. Larsson), Technical University of Berlin (with special thanks to Jim Lott), and VI-Systems.

Thank you Prof. Ben Klein and Prof. G.K. Chang for being on my reading committee and Prof. Doug Yoder and Prof. Rick P. Trebino. for serving on my thesis.

committee. Your feedback on my research has been useful in improving both the content and presentation of this dissertation.

I would like to acknowledge my colleagues. Thank you for all the memories and lunches: Dr. Jie Pan, Dr. Pierre Isautier, Dr. Sriharsha Kota Pavan, Dr. Jerrod Langston, Dr. V.A. Thomas, Alirio Melgar, Siddharth Varughese, David Haupt, Christian Bottenfield, Ewa Simpanen, Patrick Goley, Patrick Caputo, Daniel Lippiatt, Daniel Garon, Gareeyasee Saha, Nick Ledenstov Jr., Patrick Decker, Kevin Anzalone, and recent colleagues. You made my learning experience more enjoyable and meaningful.

To the friends I made here, who are too many to name individually but especially: Yoni Gabbay, Anup Omprakash, Zachary Fleetwood, and Chris Farley, thank you for all your support and encouragement.

Lastly, to my parents, thank you for the unconditional support throughout my life; my sister for her encouragements and support; and my extended family for always being there.

TABLE OF CONTENTS

LIST OF TABLES

LIST OF FIGURES

LIST OF ABBREVIATIONS

AWG	Arbitrary Wave Generator
AWGN	Additive White Gaussian Noise
BER	Bit Error Rate
BLW	Baseline Wander
BW	Bandwidth
CD	Chromatic Dispersion
COV	Covariance
CSD	Cross-Spectral Density
DAC	Digital to Analog Converter
DFE	Decision-Feedback Equalizer
DMA	Differential Mode Attentuation
DMD	Differential Mode Delay
EA	Error Analyzer
EMBc	Calculated Effective Modal Bandwidth
ER	Extinction Ratio
FFE	Feed-Forward Equalizer
FIR	Finite Impulse Response
FP	Fabry-Perot
ISI	Inter-symbol Interference
MC	Mode Coupling
MCDI	Modal and Chromatic Dispersion Interaction
MD	Modal Dispersion
MLSE	Maximum Likelihood Sequence Estimation

MM	Multimode
MMF	Multimode Fiber
MN	Modal Noise
MPD	Mode Power Distribution
MPN	Mode Partition Noise
MS	Mode Set
MSB	Mode Spectral Bias
NRZ	Non-return to Zero
O-A	Ogawa-Agrawal Model
OMA	Optical Modulation Amplitude
OOK	On-off Keying
PAM	Pulse Amplitude Modulation
PD	Photodiode
PRBS	Power Spectral Density
PSD	Psuedo-Random Bit Sequence
RC	Raised Cosine
RIN	Relative Intensity Noise
SER	Symbol Error Rate
SM	Single Mode
SMV	Single Mode Variance
SMF	Single Mode Fiber
SNR	Signal-to-Noise Ratio
STDV	Standard Deviation
TE	Transverse Electric
TIA	Trans-impedance Amplifier

TM	Transverse Magnetic
TMC	Two Mode Correlation
UnS	Unshaped
VAR	Variance
VCSEL	Vertical-Cavity Surface-Emitting Laser
VOA	Variable Optical Attenuator
WBMMF (OM5)	Wideband MMF

CHAPTER 1.

VCSEL-BASED MULTIMODE FIBER OPTICAL INTERCONNECTS

Optical telecommunication systems play a significant, yet rarely visible role in delivering our information transmission needs. Fiber-optic communication systems form the backbone of mobile networks, where only the last link between the base station and the user is realized by radio transmission. The city, country and world spanning telecommunication networks are also based on the unique ability of guided light to transfer large amounts of data. Even the short reach networks in the data centers, which store online videos, our e-mails and other data, are dependent on optical communications. A plot of the

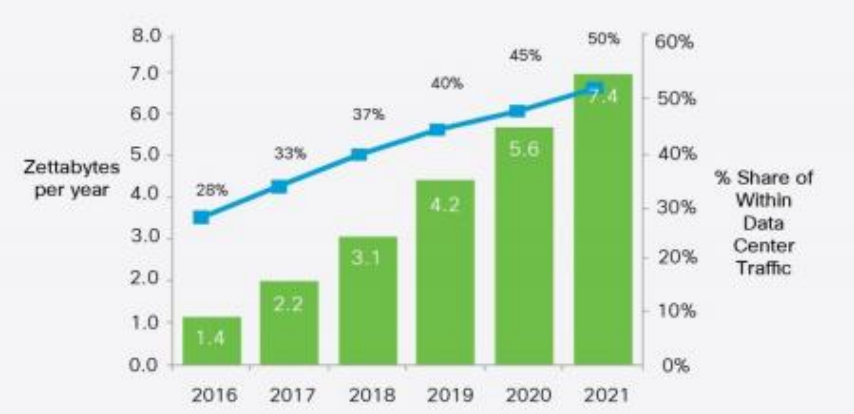

Fig. 1.1. Trend in the increase of data traffic and percentage in data centers

growth in data traffic with time, Fig. 1.1 [1], reveals that the data rates are predicted to steadily increase, while an increasing percentage of the traffic will be within the data center. In order to keep up with this increasing demand there is a need to increase the data rates, various standards have been developed by the IEEE 802.3 study group [2]. To answer the market demand, the speed of optical interconnects has been steadily increasing. So far, the improvement has been largely due to continued development of faster short-reach sources (vertical-cavity surface-emitting lasers [VCSELs]) and detectors. However, the

throughputs and transmission distances of single fiber in short-range networks are already limited by the low bandwidth distance product of multimode fibers (MMFs), which are commonly used in such applications. Replacement of the MMF with single mode fiber (SMF) could be a possible solution, but that would require single mode lasers, more precise packaging and connectors which would drive the cost up. A more practical solution is to use parallel optical links utilizing arrays of transmitters and receivers, along with ribbon cables, in which many MMFs are bundled together, as it is stated in the 40G/100G Ethernet standard [3]. The potential of such spatial multiplexing is however limited by the amount of space available in the transceiver, which is typically desired to be comparable in size to present small form-factor pluggable transceivers. Therefore, there is a need for an increased throughput and distance achievable with a single fiber in the short-range optical networking applications.

1.1 Types of Multimode Fiber

MMF is the most popular type of optical fiber in short-range optical interconnects today. The main advantage of the MMF is a large core area, which relaxes alignment tolerances in coupling, makes launching light from the transmitter easier and reduces costs. The disadvantages of MMF, compared to e.g. SMF are higher cost per meter and intermodal dispersion. The higher cost per meter is offset by the fact that in a data center with a large number of short links the connectorization is a bigger cost-driving factor. The intermodal dispersion causes pulse broadening at the end of the fiber and reduces the bandwidth-distance product. The typical MMF core diameter is between 50μm and 62.5μm. In most datacenters, OM3 and OM4 fiber dominate optical interconnects,

Table 1.1. Comparison of OM3, OM4, and OM5 fiber with standardized distances and *expected distances

	OM3	OM4	OM5
Core Size (μm)	50	50	50(30)
Modal Bandwidth (EMBc GHz-km)	>2@850nm	>4.7@850nm	>4.7@850nm >2.47@953nm
40GbE (distance)	100m	150m	150m
100GbE (distance)	70m	100m	100m
40G-SWDM (distance)	N/A	*350m	*440m
100G-SWDM (distance)	N/A	*100m	*150m

however, it is expected that OM5 will replace OM4 in newly built data centers. Table 1.1 shows some of the basic differences between OM3, OM4 and OM5 based MMF links.

1.2 High Capacity Optical Interconnects

The current IEEE 802.3bm standard uses 25G VCSELs over four or sixteen lanes of MMF at a data rate of 25.78125G to allow forward error correction (FEC) [4]. The 100G MMF and 400G MMF standard is in response to the need for higher density front panel interfaces and the need to reduce the cost and power of 100G optics and cabling. Due to their simplicity and lack of digital signal processing (DSP), VCSEL-MMF links are very sensitive to numerous penalties. The most important impairments in MMF links are due to the ISI effects such as chromatic dispersion (CD), modal dispersion (MD), non-ideal rise-time of the VCSEL, limited receiver bandwidth and noise impairments such as relative intensity noise (RIN) of the VCSEL, mode partition noise (MPN) due to VCSEL-MMF combination, thermal noise, electrical amplifier noise and shot noise at the receiver. While the CD is caused due to the wavelength dependence of the refractive index of the fiber, the MD arises out of the relative delays between the different optical paths in the fiber and is determined by the alpha profile of the graded index (GI) MMF.

MPN and RIN are related to the noise characteristics of a VCSEL. RIN represents intensity fluctuations in the composite power output of a VCSEL and is a power-dependent multiplicative noise. It is independent of the channel response. MPN on the other hand is caused due to a combination of the mode power fluctuations among different lasing modes in a VCSEL and the dispersive element in the link, typically the fiber. The correlated random fluctuations among the VCSEL transverse modes combined with the differential mode delays (DMD) due to the CD and MD of the MMF to cause random timing jitter in the received pulse. This bounded random jitter which is termed as MPN is then measured as intensity fluctuations at the sampling instant at the receiver [5].

The new standard in development is focusing on 400G MMF interconnects over fewer fibers using shortwave division multiplexing (SWDM). This incorporates standards for 26.5256Gbd PAM-2 and PAM-4, two lambda centered at 850nm and 910nm wavelengths, stronger forward error correction, and equalization at the receiver. The focus of this research will be to employ and evaluate strategies and techniques that have been used in long-haul links in low-complexity, low-power modems for VCSEL-MMF interconnects with the goal of increasing data rates and fiber capacity. This includes: MMF with sufficient bandwidth to support multiple wavelengths of VCSELs (OM5), advanced modulation formats and faster line rates, simple transmitter equalization, and few tap pulse shaping.

The rest of the thesis is organized as following: Chapter 2 will give a background on Multimode fiber VCSEL communication links. Chapter 3 will go into detail on the effects of VCSEL mode competition on fiber communication systems. Chapter 4 will introduce VCSEL data communication systems and DSP-enabled links for faster data rates. Chapter

5 will introduce shortwave division multiplexing for increasing fiber capacity. Chapter 6 will report on results using state-of-the-art equipment and VCSELs. And, Chapter 7 will give some conclusions and direction towards next steps.

CHAPTER 2.

MULTIMODE FIBER VCSEL COMMUNICATION SYSTEMS

In general, any communication system needs three basic components: a transmitter, a communication channel, and a receiver. The transmitter takes the incoming digital data and converts it into a signal which can be transmitted over the communication channel. The communication channel is a physical medium used to transport the signal. Any physical channel has a limited bandwidth, adds noise to the signal, and causes other impairments, e.g. due to non-linearities of the components. The task of the receiver is to recover the original data sent by the transmitter as accurately as possible. The two fundamental properties, which characterize any communications channel, are bandwidth and signal-to-noise ratio (SNR) in the receiver.

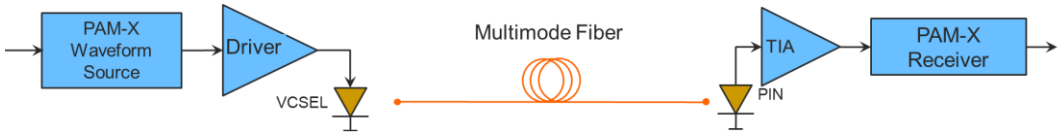

Fig. 2.1: Block diagram of a typical short reach VCSEL-MMF communication link

This chapter aims at providing a background in optics, photonics, and communications systems, required to understand, with minimal prior knowledge, the topics covered in this dissertation. This chapter does not claim to provide any novelty and heavily calls upon prior art from the synthetic work of Szczerba et al. [6], Agrawal et al. [7], Balemarthy et al. [8], Castro et al. [9], and Pavan et al. [10].

2.1 Vertical-Cavity Surface-Emitting Lasers

2.1.1 Directly Modulated Lasers

In this research, the optical link starts with the directly modulated semiconductor laser. These types of lasers are very power efficient [11], with overall power conversion efficiencies >50 % being fairly common. The word “laser” is an acronym for Light Amplification by Stimulated Emission of Radiation, which briefly summarizes the process. There are two components of any laser: an optical resonance cavity and an optical gain medium, which in this research is a semiconductor material. A photon travelling through the gain medium is able to generate an identical photon through stimulated emission, i.e. stimulating the recombination of an electron-hole pair. The emitted photon will have the same wavelength and phase (i.e. the same quantum state) as the stimulating photon. The resonance cavity provides a confinement of the photons, which leads to subsequent repetition of the light amplification process. The optical resonance cavity is usually formed between two mirrors, which can be built in numerous ways. To enable resonance, the cavity round-trip distance must be an integer number of wavelengths. The resonance can only happen for a discrete number of wavelengths and the separation between them is inversely proportional to the cavity length. The gain medium in an electrically pumped semiconductor laser typically consists of an intrinsic (undoped) layer of a semiconductor material, placed between p- and n- doped layers. This forms a semiconductor diode. When the diode is forward biased, charge carriers (electrons and holes) accumulate in the intrinsic layer. Electrons in the conduction band states can transit to lower energy states in the valence band, emitting the surplus energy as light. The transitions can be either spontaneous or stimulated. The bandgap of the semiconductor material used must correspond to the energy of photons at desired operation wavelength. As the current is increased, the number of carriers available for stimulated emission is increased, and

consequently the gain. When the gain exceeds the loss, which is due to absorption and cavity losses, the lasing threshold is reached. The current at which this happens is called the threshold current. For most optical communication systems, a low threshold current is desired. There are many varieties of semiconductor lasers, starting with multiple possibilities of forming resonance cavities in semiconductor lasers – from simple Fabry-Perot type of cavities formed by cleaving of the edges of the laser chip to distributed feedback reflectors (DFB) to external mirrors for tunable lasers. The choice of material for the laser is largely dictated by the required operation wavelength. For optical interconnects the wavelength of operation is standardized at around 850nm [12] and therefore GaAs-based materials are used. Longer wavelengths, such as 1060nm or 1090nm, will add an indium alloy to create an InGaAs based material. Light emitting diodes (LEDs) were used in the first short-range communication systems, but they do not have sufficient modulation bandwidth for modern applications. In short-range optical links the laser combines the functions of light source and modulator. In long reach systems directly modulated lasers are usually avoided, because of large chirp, which interacts with the chromatic dispersion and can increase or decrease the severity. This was not a major concern in short-range links until recently. A directly modulated VCSEL eliminates the bulky external modulators which often require high driving voltages and so it became the preferred transmitter for these short-reach communication links.

2.1.2 Vertical-Cavity Surface-Emitting Lasers

VCSELs were proposed over three decades ago by the Japanese scientist Kenichi Iga [13]. They gained popularity over the late 1990s and 2000s [14]. This type of laser emits radiation from the surface, in a direction perpendicular to the substrate. The main benefit

being that the lasers can be easily tested on a wafer, before dicing or packaging, which greatly reduces the production costs. The resonant cavity is most commonly formed by reflectors comprised of alternating layers of high and low refractive index material, parallel to the substrate, forming high quality distributed Bragg reflectors (DBRs). At least one of the reflectors must be partially transmissive to enable extraction of light from the laser. The resonance cavity is located between the reflectors. Lateral confinement can be provided by various means. In modern GaAs-based high-speed VCSEL designs, it is typically done with oxide apertures. The resonance cavity is perpendicular to the substrate and is very short and wide. This geometry supports a single longitudinal and multiple transverse optical modes. Light is emitted from the laser vertically, along the direction of the cavity. In the resonance cavity, there is a gain region formed by a p-i-n junction. The popularity of VCSELs can be attributed to some of their unique properties, like longitudinal single mode operation, large modulation bandwidth and high quality circular beams. The most important features are, however, low-cost fabrication and low power consumption [15]. Current state of the art (i.e. lowest) energy dissipation in a VCSEL used for data communication is below 100fJ per bit at 25Gbps [16, 17]. The basic static property of any semiconductor laser is how the optical output power P depends on the electrical current I driving the device. The optical output power is very small for currents below the threshold current, which typically ranges from 0.3mA to 1mA. The output power rapidly increases above the threshold current. The growth is linear at low currents, but it saturates at some point and begins to decrease with increased current. This happens due to thermal effects, since the increased current contributes to increased heating inside the device. Knowledge of the relation of the optical output power and voltage across the device as a function of

the bias current gives also insight into the laser power efficiency, which is given by $\eta = P/(IV)$, where P is the optical output power, I is the current and V is the voltage across the laser. The higher the efficiency the better, since less energy is wasted as heat. The high speed VCSELs used for data communications are usually low power devices, with maximum output powers rarely reaching over 10mW until recently [18].

2.1.3 Spectral Characteristics

VCSELs available today have a single longitudinal mode and single to multiple transverse modes. As each transverse mode has a slightly different wavelength, the result is a broad spectrum of the laser dependent on the amount of lasing mode groups. To make matters more complicated, the number of lasing modes can change with the bias current, with more modes possible at higher bias currents. It also worth noting, is that the laser spectrum is much broader than the bandwidth of the modulating signal. For example, a spectral width of 1nm at 850nm corresponds to a bandwidth of 415GHz, which is much higher than the typical modulation bandwidth. Therefore, the spectral efficiency of the modulation becomes irrelevant, since effects related to e.g. chromatic dispersion will be dominated by the spectral width of the laser itself. It was shown that VCSELs with fewer transverse modes and narrower spectral widths can enable longer transmission distances in MMF [19, 20, 21]. Standards dealing with short-range optical communications have recommendations on the root mean square (RMS) spectral width of the lasers used in the transmitters. For example, Ethernet specifies 0.6nm as the maximum spectral width for 10Gbps lanes [22, Sec. 6]. It is possible, however to make single mode VCSELs, with very narrow spectral widths, which will be investigated in Chapter 6. Transmitters with narrower spectral widths, such a single mode VCSELs, can yield higher bandwidth-

distance products. Single mode VCSELs can be made for example by using smaller oxide apertures e.g. as the ones used in [19, 20], or increasing the loss for higher order modes [21]. The result is a laser with narrower spectral width. This improves propagation in MMF and helps reach longer distances at high bit rates, while still retaining the ease of connectorization of multimode fiber.

2.1.4 Frequency Response

The frequency response of a VCSEL is one of the key parameters from the point of view of the system design. In general, the frequency response of a semiconductor laser is flat at low frequencies, possibly with a peak at the resonance frequency, and then it has a fast roll-off [11]. The frequency response depends not only on the laser design, but also on the bias current. The larger the bias current, the higher the resonance frequency. This relationship holds until thermal saturation effects take over in effect limiting the maximum bandwidth. The presence of a strong resonance peak also has a significant effect on data transmission, as it causes an overshoot on symbol transitions, and this can be detrimental for multilevel data transmission.

2.1.5 Laser Noise

Relative intensity noise (RIN) is caused by shot noise and the spontaneous emission coupled into lasing modes. This causes unwanted fluctuations of the optical power, thereby generating a noise current in the optical receiver circuit, which translates to an optical power penalty in the data link. RIN is measured with respect to a finite bandwidth optical system, and is thus quoted in terms of dB/Hz. Another source of optical power noise is the feedback of stray optical reflections into the laser. This is an unavoidable effect common

to all laser systems, and proper engineering of the optical assembly is required to minimize its effects. The optical power in a multimode VCSEL is partitioned between several lasing modes, so modal noise can occur when one of the modes is indirectly discriminated. Polarization-selective elements, such as beam splitters and some couplers, can also produce this kind of noise [23]. To minimize such effects as many VCSEL lasing modes as possible should be coupled into the fiber in order to prevent differential mode attenuation.

2.1.6 Mathematical Model

If we were to summarize the VCSEL behavior mathematically, the multimode spatiotemporal rate equations [24-31] for modeling a VCSEL can be listed as:

$$\begin{cases} \frac{\partial N(\boldsymbol{r},t)}{\partial t} = \frac{nj(r,t)}{eV} - \frac{N(\boldsymbol{r},t)}{\tau_N} + D_N \nabla^2 N(\boldsymbol{r},t) - v_g \sum_{ij} G_{ij}(\boldsymbol{r},t) S_{ij}(t) + F_N(t) \\ \frac{dS_{ij}(t)}{dt} = \Gamma_{ij}\beta_{ij} \frac{\int\int N(\boldsymbol{r},t)d\boldsymbol{r}}{\pi R^2 \tau_N} + \frac{\Gamma_{ij} v_g S_{ij}(t)}{\pi R^2} \int\int G_{ij}(\boldsymbol{r},t)d\boldsymbol{r} - \frac{S_{ij}(t)}{\tau_S^{ij}} + F_S(t) \end{cases} \tag{2.1}$$

where N(r,t), $S_{ij}(t)$, and j(r,t) are the carrier, photon, and injection current density in the active region of the VCSEL, respectively. The subscript ij denotes the IJ transverse mode. **r** and t denote the polar coordinates and time. $G_{ij}(\mathbf{r},t)$ is the modal gain. The carrier rate equation terms can be described as the injection current, depletion due to recombination, carrier diffusion into the device, and depletion due to stimulated emission in the ijth mode, from left to right. The photon rate equation can be described as the spontaneous emission due to carrier recombination, photons created due to stimulated emission in the ijth mode, and the photon lifetime in the cavity. $F_N(t)$ and $F_S(t)$ are the noise caused by spontaneous emission. Based on the equation set, a time domain model could be developed which takes mode competition, carrier diffusion losses, and RIN into consideration. However, if we

consider a communication link and just not the VCSEL, we need to transform the photons into an electric field to calculate all effects in the communication link. Therefore, we need to solve the rate equations in the form of:

$$E(t) = \sqrt{S}\exp(-i(\omega t + \phi)) \tag{2.2}$$

A laser diode oscillator has a finite linewidth due to phase fluctuation of the electric field cause by spontaneous emission. The phase fluctuation can be characterized as [24]:

$$\frac{d\phi_{ij}(t)}{dt} = \frac{\alpha}{2}\Gamma_{ij} v_g a_N [N(t) - N_{th}] \tag{2.3}$$

where α is a linewidth enhancement factor, $\phi_{ij}(t)$ is the phase of the output signal of the VCSEL, and $a_N = \partial G/\partial N$ is defined as differential gain.

The wavelength of each transverse mode is different [9]. A simple model of an oxide confined VCSEL could be a circularly symmetric step-index optical waveguide. Under the boundary conditions for a circularly symmetric step-index optical waveguide with a radial core, the eigenvalue equation [32] for the wave equation is as follows:

$$u\frac{J_{p-1}(u)}{J_p(u)} = -\omega\frac{K_{p-1}(\omega)}{K_p(\omega)} \tag{2.4}$$

Where u and ω represent the normalized frequencies in core and in the cladding respectively, and J represents the Bessel function of the first kind and K represents the Hankel function of the first kind. For a given mode, the normalized frequencies u and ω are represented as:

$$u_{ij} = r\sqrt{n_c^2 k^2 - \beta_{ij}^2} = k \cdot r\sqrt{n_c^2 - n_{eff,ij}^2} \tag{2.5}$$

$$\omega_{ij} = r\sqrt{\beta_{ij}^2 - n_{cl}^2 k^2} = k \cdot r\sqrt{n_{eff,ij}^2 - n_{cl}^2} \tag{2.6}$$

Where i represents the azimuth mode index and j is the radius mode index. n_c, n_{cl}, and $n_{eff,ij}$ are the core index, the cladding index, and the effective mode index of mode IJ. k is the wave vector of central wavelength in a vacuum. B is the propagation constant in the VCSEL cavity.

The wavelength of each transverse mode can be predicted by a simple effective index model [33]:

$$\frac{\Delta n_{eff,ij}}{n_c} = \frac{\Delta\lambda}{\lambda_c} \tag{2.7}$$

where λ_c is the central wavelength. $\Delta n_{eff,ij}$ is the difference between the core index n_c and the effective mode index n_{cl}. $\Delta\lambda$ is the wavelength shift with respect to λ_c.

Instead of solving for $n_{eff,ij}$ the phase parameter of the step index optical waveguide, B, can be used to calculate $\Delta n_{eff,ij}$. The phase parameter B of each IJ mode can be described as:

$$B_{ij} = \frac{\omega_{ij}^2}{u_{ij}^2 + \omega_{ij}^2} = \frac{n_{eff,ij}^2 - n_{cl}^2}{n_c^2 - n_{cl}^2} \tag{2.8}$$

In a weakly guided step-index waveguide, $n_c + n_{cl} \approx 2n_c$ and $\Delta n_{eff,ij}^2 \approx 0$. Therefore, $\Delta n_{eff,ij}$ can be represented as:

$$\Delta n_{eff,ij} \approx \frac{n_c^2 - n_{cl}^2}{2n_c}\left(1 - B_{ij}\right) + \Delta n_{eff,ij}^2 \approx (n_c - n_{cl})(1 - B_{ij}) \tag{2.9}$$

Substituting (2.9) into (2.7), the wavelength shift, $\Delta\lambda_{ij}$, relative to λ_c is obtained by:

$$\Delta\lambda_{ij} = \lambda_c \frac{n_c - n_{cl}}{n_c}(1 - B_{ij}) \tag{2.10}$$

Hence, the wavelength of each transverse mode is derived as:

$$\lambda_{ij} = \lambda_c - \lambda_c \frac{n_c - n_{cl}}{n_c}(1 - B_{ij}) \tag{2.11}$$

With these equations the VCSEL output can be written as an electric field. First, the mode power, S_{ij}, can be calculated by the rate equations. Second, the phase of each transverse mode ϕ_{ij} can be calculated by equation (2.3). Third, the center wavelength of each transverse mode λ_{ij} can be calculated by equation (2.11). The output of the optical signal in terms of E(t) is then:

$$E(t) = \sum_{ij} \sqrt{S_{ij}} \exp\left(-i\left(\omega_{ij}t + \phi_{ij}\right)\right) \tag{2.12}$$

where the mode frequency $\omega_{ij}=\lambda_{ij}/c$, and c is the speed of light. Note that the electric field of each mode $E_{ij}(t)$ is captured as well.

2.2 Multimode Fiber

Multimode Fiber (MMF) is the most popular type of optical fiber in short-range optical interconnects. The main advantage of the MMF is a large core area, which relaxes alignment tolerances in coupling, makes launching light from the transmitter easier, and reduced costs in the 2000s. This was very important in first systems using LED sources. The disadvantages of MMF, compared to e.g. single mode fiber (SMF) are higher cost per meter and intermodal dispersion. The higher cost per meter is offset by the fact that in a

data center with a large number of short links the connectorization is a bigger cost-driving factor. The intermodal dispersion causes pulse broadening at the end of the fiber and reduces the bandwidth-distance product.

2.2.1 Multimode Propagation

The typical MMF core diameter is between 50 μm and 62.5 μm. For comparison, a typical SMF has a core diameter of 9 μm. The light guiding mechanism in an MMF is the same as any other dielectric waveguide, a core of refractive index n_0 is surrounded by a cladding with a refractive index $n_1 < n_0$. Due to total internal reflection, the propagating light is trapped inside the core, as long as the incidence angle at the core-cladding interface is smaller than the critical angle (defined with respect to the fiber axis). This simple description does not, however cover the entire picture. The field of the propagating wave has to repeat itself as it reflects at the interface. The fields that satisfy this condition are called modes of the waveguide [34, Ch. 7]. The fields of the modes maintain the same transverse distribution and polarization along the waveguide. From a mathematical point of view, modes are a solution to the electromagnetic wave equation in the waveguide, and in this case, an MMF. The wave equation for weakly guiding dielectric waveguide, where $n_1 - n_0 \ll 1$ can be simplified to a scalar wave equation [35, Ch. 14],

$$(\nabla_t^2 + k_0^2 n^2(r) - \beta^2) E_t(r, \theta) = 0 \tag{2.13}$$

where E_t gives the transversal electric field profile defined in the cylindrical coordinate system normal to the fiber axis given by (r, θ), k_0 is the wavenumber, β is the propagation constant and n(r) gives the refractive index profile, which is assumed to be axially symmetric around the fiber axis. The solutions to this equation are the linearly polarized

modes, commonly denoted as LP_{ij} modes, with subscript indexing for the radial and azimuthal orders of the mode, respectively. The LP_{01} is the fundamental mode, and in SMFs it is the only mode of the fiber. The number of modes in a fiber can be calculated using the V parameter [34, Ch. 8],

$$V = 2\pi \frac{a}{\lambda} \sqrt{n_1^2 - n_0^2} \tag{2.14}$$

where λ is the wavelength of the light propagating in the fiber and a is the core diameter. For fibers with large V the number of modes can be approximated as

$$N_{modes} \approx \frac{4}{\pi^2} V^2 \tag{2.15}$$

given in [57, Ch. 8]. For fiber with a core diameter in the range between 50 μm and 62.5 μm, with a core refractive index of 1.5, and 1% index contrast between the core and the cladding, the number of supported modes is between 600 and 900. An arbitrary transverse electric field in a dielectric waveguide can be written as a superposition of guided modes possible for a given waveguide [34, Ch. 7],

$$E(x, y, z) = \sum_{i,j} a_{i,j} u_{i,j}(x, y)\, exp\left(-j\beta_{i,j} z\right) \tag{2.16}$$

where for each mode ij, $a_{i,j}$ is the mode amplitude, $u_{i,j}(x, y)$ is the mode distribution and $\beta_{i,j}$ is the propagation constant of each mode. The propagation constant is different for each mode, and since the group velocity v_g is dependent on the propagation constant β as

$$\frac{1}{v_{g,i,j}} = \frac{\delta \beta_{i,j}}{\delta \omega} \tag{2.17}$$

where ω is the angular frequency, the group velocity of each mode could be different. This translates to a differential mode delay between modes [36], and in effect causes the modal dispersion. Different launch conditions can excite different groups of modes, giving rise to unpredictable performance of the MMFs, particularly when older types of fiber designed for overfilled launch (i.e. exciting all modes) with LEDs are used with laser transmitters [37]. However, it has been demonstrated that under special coupling conditions the propagation reach in MMF can be dramatically increased [38]. It would seem, that given the amount of modes, the modal dispersion will be too large to achieve any reasonable transmission distance in MMF. There are however mode groups with identical or similar group velocities, and they can be grouped together in principal mode groups. Modes LP_{ij} belong to the same principal mode group m if they fulfill the condition [39]

$$m = 2j + i - 1 \tag{2.18}$$

The number of modes in a group increases with the group number m, with the lowest-order group containing on the fundamental mode [40]. Since the modes in a mode group have similar properties, they can be treated in terms of mode groups, rather than individual modes [41].

2.2.2 Graded Index Fiber

Given that there are many mode groups in an MMF, each with different group velocity, it is important to design the fiber in such a way, that it minimizes the spread in propagation between different modes. This is achieved when the refractive index is highest at the fiber axis and gradually decreases towards the cladding [42]. It is common for the

cores of graded-index fibers to follow power-law index profile (alpha profile) [41] given by [34, Ch. 8].

$$n^2(r) = n_a^2\left[1 - 2\left(\frac{r}{a}\right)^p\left(\frac{n_a^2 - n_1^2}{2n_a^2}\right)\right],\ r \le a \tag{2.19}$$

where n_a is the refractive index at the fiber axis, n_1 and p is the profile exponent. For an optimized value of the profile exponent, the differential mode delays (DMD) can be nearly eliminated [39]. The optimal profile exponent is dependent on fiber material and the wavelength of light which is supposed to be used. Note that the index profile can be optimized at only one wavelength. Apart from intermodal dispersion there is also chromatic dispersion. Multi-mode VCSELs have sufficiently broad spectrum to suffer from this problem [43]. Single-mode VCSELs operating at 850 nm and with sufficient output power and low manufacturing cost [44] could help to avoid it. The launch conditions are also important, as the number of excited modes and power distribution between the modes is going to influence the impulse response of the fiber.

2.2.3 Index Perturbations

Fiber manufacturers try to achieve the pure alpha profile for elimination of DMD, but process limitations result in small deviations. The set of perturbations, comprising 108-fibers, was first created by researchers at the University of Cambridge [45] and further modified by the IEEE 802.3aq Ethernet task force [46]. The almost quadratic shape in Fig. 2.2 corresponds to the pure alpha profile with a nominal value of $\alpha = 1.97$. Sometimes the α of the profile can vary across the fiber cross-section. The 108 fiber model divides the core region into two halves, each of which can independently have $\alpha = 1.89, 1.97, 2.05$. In

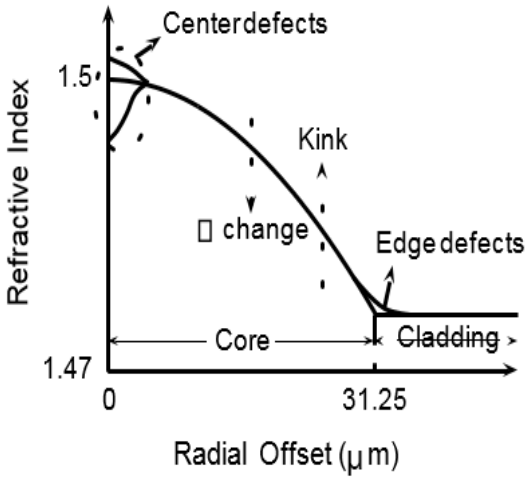

Fig. 2.2: Refractive index change in the fiber core

addition to the nominally smooth α profile at the center, dips and peaks are also observed in practice. The transition at the core and cladding interface can be abrupt or exponentially smooth. The final defect considered in the 108-fiber set is the kink which is effectively a perturbation in the gradient of the refractive index profile. The model considers both kink-free profiles and kinks at different locations. The model arrives at a total of 108 index profiles by considering all possible combinations of these perturbations. The parameters of these index perturbations are specified in [46]. Another widely prevalent fiber model is the Monte Carlo fiber set [47], which consists of approximately 5000 fibers whose modal delays are determined by empirically matching randomly generated delays to statistics of measured fiber parameters such as bandwidth and delay spread. The data about these measured fibers was provided by the top three fiber manufacturers in the world.

The 108-fiber set is considered to represent the worst 5% of the installed fiber base [45] whereas the Monte Carlo model is supposed to be representative of the entire installed base. The validity of both claims was highly debated in the IEEE 802.3aq task force discussions. Although the 108-fiber set was initially used by the task force, the final power

budgets and the receiver test impulse responses determined by the IEEE are based on the Monte Carlo fiber set. This is partly because the Monte Carlo set is indirectly based on fiber measurement data.

2.2.4 Modal Delays

Though the pure alpha profile minimizes the delay spread, actual fibers with these non-ideal refractive index profiles exhibit considerable delay spread in practice. Figure 2.3 illustrates this effect by showing the modal delays for the pure alpha profile, the center dip profile the center peak profile and finally a fiber with a kink in its refractive index profile. These perturbations have been chosen from the 108-fiber model.

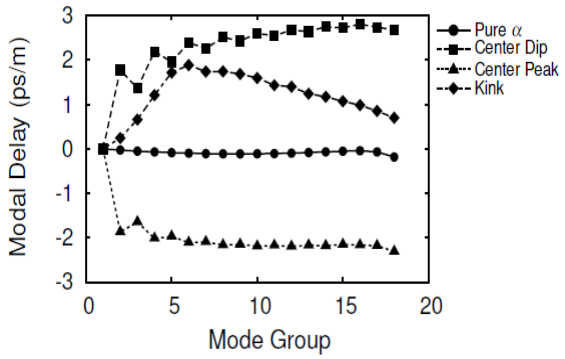

Fig. 2.3: Mode delay by fiber mode group

Although one cannot predict how the modal delays for a particular profile will behave without detailed simulations, the general trends can sometimes be estimated. For example, the center dip profile implies that the mode groups propagating closer to the axis, the lower-order mode groups (LOMs), travel faster than the mode groups away from the axis, the higher-order mode groups (HOMs). Therefore, the modal delays should increase with mode group in general, as verified by Figure 2.3.

2.2.5 Modal-Chromatic Dispersion Interaction (MCDI)

To expand on this idea, the effects of mode spectral bias (MSB) on the transmitted signal can be mathematically modeled assuming that the VCSEL normalized spectrum can be represented by:

$$S(\lambda) = \sum_{i=1}^{M} A_i \delta(\lambda - \lambda_i) \tag{2.20}$$

where *i*th denotes the VCSEL mode order, M the total number of VCSEL modes, λ_i the wavelength of each mode, δ() the Dirac delta function, and $A_i = h_n E\{a_i(t)\}$represents the normalized long term averaged power of the *i*th VCSEL mode with $E\{a_i(t)\}$ the time average function, $a_i(t)$ is the instantaneous power of each mode, and h_n a normalization factor that takes into consideration the duty cycle of the signal and the extinction ratio of the laser. For a modulated VCSEL that couples light into an MMF, the received signal after electronic conversion can be expressed as

$$y(t) = P_{OMA} \sum_{i}^{M} F_i(t) a_i(t) + n(t) \tag{2.21}$$

where P_{OMA} is the optical modulation amplitude (OMA) transmitted power, n(t) is the additive Gaussian white noise (AWGN) in the receiver, and $F_i(t)$ is the waveform for each mode after coupling to the fiber given by

$$F_i(t) = \sum_{g}^{Ng} C_{ig} f_i\left(t - L\Delta t_{ig}\right) \tag{2.22}$$

where *g*th is the MMF group mode number, N_g is the number of mode groups in the MMF, C_{ig} is the coupling matrix where each of its elements represent the coupling strength of the *i*th VCSEL mode to the *g*th MMF mode group, $f_i(t)$ is the waveform before coupling to the MMF fiber for a given bit sequence, L is the link length, and the term given by

$$\Delta t_{ig} = t_g - D(\lambda_i - \lambda_0) \tag{2.23}$$

is the length normalized temporal delay of each MMF mode centroid at λ_i, where $\lambda_i > \lambda_{i-1}, D$ is the chromatic dispersion parameter. The term t_g represents the differential mode delays (DMD) of the multimode fiber with any arbitrary index profile and unit length. For an alpha-profile MMF, t_g can be approximated by [48],

$$t_g(\lambda) = \frac{N_1(\lambda)}{c}\left[\Delta\left(\frac{\alpha-\alpha_{opt}(\lambda)}{\alpha+2}\right)\cdot\left(\frac{v_g}{v_T}\right)^{\frac{\alpha}{(\alpha+2)}} + \cdots\right] \tag{2.24}$$

where N_1 is the group refractive index, $\Delta \approx \frac{n_1-n_2}{n_1}, n_1$ is the refractive index on the axis of the fiber, c is the speed of light, n_2 is the refractive index in the cladding, v_g is the number of modes inside the mode group (MG) g, v_T is the total number of modes, and

$$\alpha_{opt}(\lambda) \approx 2 - \frac{2n_1}{N_1}\frac{\lambda}{\Delta}\frac{d\Delta}{d\lambda} \tag{2.25}$$

is the optimum alpha value that minimize group delay at the operational wavelength λ. The previous equation minimizes t_g to the first order in Δ [48]. Note that all temporal delays used here are relative values and the more negative the value the shorter the travelling time.

The main parameters that account for the MCDI effect in VCSEL-MMF channels, are the coupling terms C_{ig}, the chromatic dispersion, and the magnitude and sign of the mode delays expressed in the Δt_{ig} term. The coupling term quantifies the degree of MSB

Table 2.1: Mode spectral bias and chromatic dispersion effects.

MMF Mode Order	**MMF Mode Spectra**	**Mode Spectra Effect on Velocity**
Higher Order Modes (HOMs)	Shorter wavelengths of the VCSEL spectra	Reduce velocity
Lower Order Modes (LOMs)	Longer wavelengths of the VCSEL spectra	Increase velocity

in the MMF. Due to MSB and chromatic dispersion, changes in the speed of the mode groups are produced as summarized in Table 2.1. Changes in MMF mode delays can produce advantageous or detrimental effects in the channel bandwidth. In order to explain the bandwidth changes, it is required to classify the fibers based on the speed of their modes relative to its mode order. In [49] the MMFs are classified as: Left-tilted DMD MMF (L-MMF) and right-tilted DMD MMF (R-MMF). This classification is independent of their modal bandwidth.

In L-MMF high-order modes (HOMs) tend to travel faster than low-order modes (LOMs). Conversely in R-MMF LOMs tend to travel faster than HOMs. This characteristic can be better illustrated by using alpha-profile MMFs [48]. For example, L-MMFs have alpha parameter values slightly lower than the optimum alpha value computed. Utilizing this lower alpha value produces negative delays that increase their magnitude as the mode group index increases. Therefore, in this theoretical L-MMF all the HOMs travel faster than the LOMs. Conversely, for R-MMF alpha profile fiber the alpha parameter is slightly higher than the optimum alpha value (6) producing larger positive delays as the MG index increases. In the R-MMF all HOMs travel slower than LOMs.

The result of deploying these two fiber types in channels where VCSEL coupling results in an MSB, is that L-MMF tends to minimize channel dispersion since the MSB causes a reduction in velocity of the faster HOMs and an increase the velocity of the slower LOMs. The overall effect for a L-MMF is a reduction of the combined modal-chromatic dispersion. Conversely, in R-MMF the combined modal-chromatic dispersion increases. Experimental evidence of the reduction of modal-chromatic dispersion has been shown indirectly based on bit error rate (BER) measurements [49]. In the vast majority of the

tested VCSEL-MMF channels, the links using L-MMF outperform the channel links using R-MMF of equal modal bandwidth [49], [50]. It should be noted that MSB effect depends on the optics utilized to couple the light from the VCSEL to the MMF. Modeling using refractive optics elements shows predominant effects of MSB as shown in [49].

2.2.6 Impulse and Frequency Response

When the power distribution over the different modes and propagation delays of each mode are known, the impulse response of the fiber can be estimated. If the fraction of power in each of the LP_{ij} modes is denoted $C_{ij,}$ the impulse response of an MMF of length L can be expressed as

$$h(t)_{MMF} = \sum_{g}^{Ng} C_{ijg}\delta\left(t - \frac{L}{v_{g,i,j}}\right) \tag{2.26}$$

The frequency response can be readily obtained from the impulse response with a Fourier transform. The frequency response of the fiber is dependent on the source type and launch conditions into the fiber. For example LEDs usually excite all modes in the fiber and consequently for LED transmitters an over-filled launch (OFL) condition is used. The fiber bandwidth under OFL condition is usually given for fibers foreseen for use with LEDs. For fibers optimized for use with VCSELs the effective modal bandwith (EMB) is given [51, 52]. The EMB is calculated using (2.26) from the DMD which is measured by selectively exciting different mode groups. To measure the DMD a single mode fiber is used to launch short pulses at different radial offsets from the center. Usually, the entire range from the fiber axis to the cladding is scanned. The frequency response of the fiber can be conveniently measured by a vector network analyzer (VNA) using the same setup as for a

Table 2.2: Comparison of OM3, OM4, and OM5 fiber with standardized distances and *expected distances.

	OM3	OM4	OM5
Core Size (μm)	50	50	50(30)
Modal Bandwidth (EMBc GHz-km)	>2@850nm	>4.7@850nm	>4.7@850nm >2.47@953nm
40GbE (distance)	100m	150m	150m
100GbE (distance)	70m	100m	100m
40G-SWDM (distance)	N/A	*350m	*440m
100G-SWDM (distance)	N/A	*100m	*150m

VCSEL frequency response measurement. As an example the frequency response could be measured for a link including with a VCSEL and OM4 MMF, with various lengths of the fiber, Table 2.2 (same as Table 1.1). The OM4 fiber has a bandwidth-distance product of 4700 MHz-km, defined for laser launch, at the wavelength of 850 nm. At this wavelength the optimized index profile guarantees very low DMD, and a narrow spectral width reduces the effects of chromatic dispersion [50]. This was shown to work in practice, transmission over 1km of OM4 MMF with a single mode VCSEL was demonstrated in [19, 20]. On the other hand, long term reliability (i.e. lifetime) of single mode VCSELs is yet to be established [44, 53]. In most datacenters, OM3 and OM4 fiber dominate optical interconnects, however, it is expected that OM5 will replace OM4 in newly built data centers. Table 2.2 shows some of the basic differences between OM3, OM4 and OM5 based MMF links.

2.3 Signal Detection and Noise

2.3.1 Signal Detection

An optical receiver converts the incident optical power Pin into an electric current. The most common device performing this task is a p-i-n photodetector. The output current is directly proportional to the incident optical power, the relationship is given by $I = R_d P_{in}$, where the R_d is the responsivity of the photodiode and P_{in} is the square of the electric field. The phase information is lost in a direct detection system. The photodiode is usually followed by an electrical amplifier, which then is followed by a decision circuit or a more sophisticated demodulator. Two types of amplifier configurations are possible, a transimpedance amplifier (TIA) and a voltage amplifier. A TIA has ideally zero input impedance, the input signal is a current and the output signal is voltage [54, Ch. 14]. The other type is a voltage amplifier, which has voltage input and voltage output. Since a photodiode can be regarded as a current source [54, Ch. 14], a TIA is a better amplifier choice. The output of the photodiode contains also undesired noise. The performance of the system depends on the signal-to-noise ratio (SNR), which is defined as follows:

$$SNR = \frac{\bar{I}^2}{\sigma^2} \tag{2.27}$$

where $\bar{I}$ and σ are respectively, the average photocurrent and the root mean square noise current. It is important to note that the SNR is defined in the electrical domain and the noise is measured in the electrical domain after the detection of the optical signal. The performance of a system is given by the receiver sensitivity, which is the amount of optical power needed to operate below a specific bit error rate (BER). In direct detection systems, the electrical power is proportional to the square of the optical power (square law detection).

2.3.2 *Fiber Independent Noise Penalties*

There are three noise sources which are relevant in multimode intensity modulation direct detection (IM/DD) systems that are independent of fiber:

1. Shot Noise

2. Thermal Noise

3. Relative Intensity Noise (RIN)

The shot noise originates from the quantum nature of light and current. Even if constant optical power is incident on the photodiode, the photon absorption and electron-hole generation processes happen at random time intervals. This gives rise to a random variation of the signal current. The variance of the shot noise is:

$$\sigma_{shot}^2 = 2qI\Delta f \tag{2.28}$$

where q, I, and Δf are respectively the elementary charge, the photocurrent, and the receiver bandwidth [55, Sec. 5.1.1]. It is apparent, that the variance of the shot noise increases with the photocurrent (and thus with the average optical power).

The thermal noise comes from the fact that at any temperature above the absolute zero the electrons are moving inside the conductor and the thermal motion of the electrons manifests itself as current noise. The variance of the thermal noise is given by

$$\sigma_{thermal}^2 = 4k_B T\Delta f/R_L \tag{2.29}$$

where kB, T, and R_L are respectively, the Boltzmann constant, the temperature, the noise figure of the amplifier following the photodiode and the load resistance [55, Sec. 5.1.2]. This noise contribution is not dependent on the signal power.

The RIN originates in the laser. The carrier generation and recombination process in a semiconductor laser is random in its nature and gives rise to noise. The RIN spectrum is not white, it peaks at resonance frequency, and for multi-mode lasers also at low frequencies due to mode competition [56]. The noise variance of the RIN after the photodetector is:

$$\sigma_{RIN}^2 = S_{RIN} I^2 \Delta f \tag{2.30}$$

where S_{RIN} is the RIN value (often expressed in dB/Hz [55, Sec. 5.4.2]). It is worth noting, that the variance of the RIN is also dependent on the signal power, just as the shot noise, but in this case, the noise variance is proportional to the square of the photocurrent.

It is important to realize how much noise there is present and which noise sources dominate, as this determines the performance of the link and potentially also design of the modulation. The following parameters illustrate well the system used in the experiments

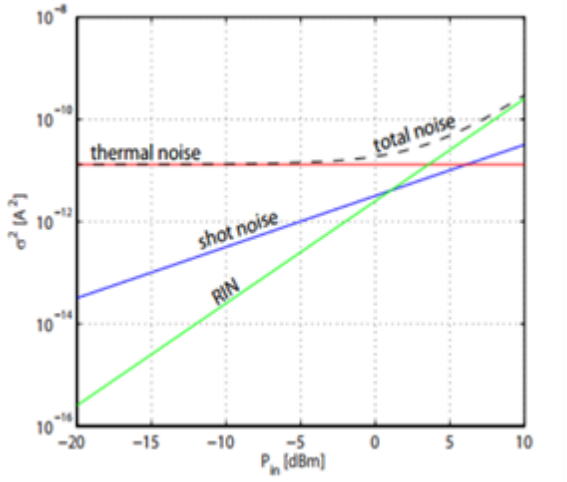

Fig. 2.4: Effects of different types of noise

presented in this work, R = 0.4A/W, T = 298K, R_L = 50Ω and S_{RIN} = −155 dB/Hz. To illustrate the relationship between the three noise contributions for the given parameters, they are plotted against received optical power P_{in} in Fig. 2.4.

The RIN and shot noise are stronger than the thermal noise only for received power levels greater than 3dBm. On the other hand, the photodetectors used in our experiments have saturation power levels at around 3dBm received optical power, so it is apparent that the system is always dominated by the thermal noise.

2.3.3 *Fiber Dependent Noise Penalties*

There is one noise source which is relevant in multimode IM/DD systems that are dependent of fiber:

Mode Partition Noise (MPN)

The MPN in VCSEL-MMF channels is caused by both the power fluctuation among VCSEL modes and the temporal separation of the VCSEL modes after propagating through the dispersive fiber. MPN is not typically the main limitation in VCSEL-MMF channels for reaches specified in IEEE 802.3 and Fiber Channel standards. However, as data rates increase, MPN can become a critical impairment to overcome for increasing or even maintaining reaches easily achieved at lower data rates. One reason for this is that MPN is dependent on optical power. Therefore, when MPN becomes the dominant noise penalty in a channel, its effect on the signal-to-noise ratio (SNR) degradation cannot be mitigated by simply increasing the transmitted power. Mode partition noise has been studied for single-mode fiber (SMF) channels using multi-longitudinal mode lasers [57–

59]. Simple analytic expressions have been derived to describe the dependence of MPN on the temporal separation of the laser modes due to chromatic dispersion and link length [59]. These models also illustrate the conditions for which bit error rate (BER) noise floors develop as a result of MPN. Although these SMF expressions are useful and have been adopted by standards organizations to determine VCSEL-MMF worst-case penalties, their derivation requires several assumptions that are not accurate for VCSEL-MMF channels.

A more general model, based upon [57], [60], [61], is shown here to accommodate for modal dispersion and the modal-chromatic dispersion interaction. The noise dependency on transmitted power can be derived from (2.21) when $a_i(t)$ is replaced by its long term average value, A_i, as follows:

$$y(t) = P'_{OMA} \sum_i^M F_i(t) A_i + n(t) + P'_{OMA} \eta(t) \tag{2.31}$$

where $P'_{OMA} = P_{OMA}/h_n$, and η(t) represents the OMA dependent noise of the system (see section 2.2.5). The OMA dependent noise term can have several components in VCSEL-MMF channels including MPN, relative intensity noise (RIN), modal noise (MN), and jitter intensity noise among others. Assuming MPN is predominant its normalized variance can be obtained using,

$$\sigma_T^2(t) = \overline{(\sum_{i=1}^M F_i(t) a_i(t) - \sum_{i=1}^M F_i(t) A_i)^2} \tag{2.32}$$

where $\overline{()}$ represents the ensemble average [50].

A simpler expression that does not require previous knowledge of the MPN statistics can be obtained from (2.32) using the method described in [57-59]. This method which can estimate the MPN standard deviation (STDV) for a simple alternating pattern in

SMF, has been extended to account for any arbitrary pattern transmitted using MMF [60], [61]. A general expression for MPN based on the Ogawa model [61] that accounts for modal chromatic interaction is given by

$$\sigma_{MPN}^2(t) = k_{MPN}^2[\sum_{i=1}^{M} F_i^2(t)A_i - (\sum_{i=1}^{M} F_i(t)A_i)^2] \quad (2.33)$$

where k_{MPN} is the mode partition noise coefficient that indicates the magnitude of the noise and relates the degree of correlation among the VCSEL modes. Several assumptions are required to obtain this, such as:

1) The temporal variations of $a_i(t)$ are slow compared with the bit rate.

2) The total power of all the modes at any instant, t, is constant, $\sum_{i=1}^{M} a_i(t) = constant$

3) The correlation of the power fluctuation among modes is given by $\overline{a_\iota(t)a_J(t)} = (1 - k_{MPN}^2)\overline{a_\iota(t)a_J(t)}$

4) The power fluctuation standard deviation can be estimated from, $\overline{\left(a_\iota(t) - \overline{a_\iota(t)}\right)^2} = k_{MPN}^2(a_i(t) - \overline{a_\iota(t)})$

5) The turn-on delays of laser modes are small compared with the bit period.

6) k_{mpn} is identical for all the VCSEL modes and it does not change among transmitted pulses.

7) There is linear power response of the fiber for each VCSEL mode.

8) The power in each transverse mode is caused by stimulated emission.

This model has been used to estimate the MPN at different temporal positions in a transmitted bit sequence [59]. The model predicts the MPN magnitude for different transmitted patterns as a function of length, spectral width of the laser, and k_{mpn}. The accuracy of this model depends on the assumptions shown above. The model predicts that σ_{mpn} is highly dependent on t where an arbitrary data sequence is transmitted. The modeled VCSEL has a Gaussian spectrum with spectral width of 0.3 nm, and $k_{mpn} = 0.3$.

Also, it should be noted that (2.32) already includes the MCDI effect due to selective coupling between VCSEL transverse modes to MMF modes. The MCDI is accommodated in F_i which depends on C_{ig}, the coupling matrix from each VCSEL mode to the each MMF. When a VCSEL is modulated, the power transmitted by each mode set (MS) varies. The power variation has deterministic and random components. By retransmitting a defined bit pattern and observing the detected signal after propagating through the MMF, it is possible to separate the deterministic and random fluctuations in the transmitted power.

For example, suppose a specific pattern was transmitted using a VCSEL into a short (5 m) section of high modal bandwidth (~4700 MHz-km) 50μm core diameter MMF. Five hundred waveforms were then captured using a sampling oscilloscope and their ensemble average waveform was computed. Refer to the total signal label in Fig. 2.5 (black trace).

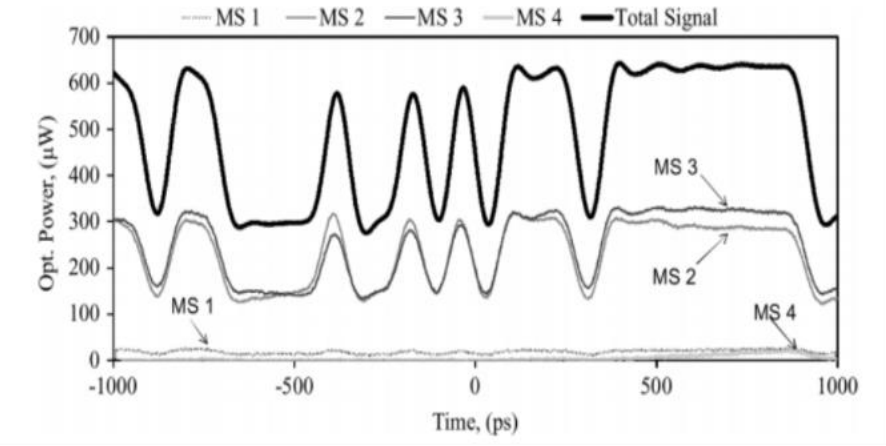

Fig. 2.5: Pattern in signal and each individual mode

The signal for each mode set (MS) was also captured using an optical filter. The ensemble average signal for each MS is shown in gray colored traces. For this VCSEL most of the power is transmitted by MS2 and MS3. The MS signal amplitude was corrected to compensate for the insertion loss through the optical filter.

Further operation on (2.33), when it is assumed a laser with a continuous spectrum and a single mode fiber channel, provides a simple analytical expression that estimates the level of MPN variance [57]

$$\sigma_{MPN} = \frac{k_{MPN}}{\sqrt{2}}(1 - e^{-\pi BLD\sigma_\lambda}) \tag{2.34}$$

where σ_λ is the spectral width of the Gaussian optical source. This expression, which utilizes few parameters of the channel such as σ_λ, k_{mpn} and L, has been used by standard organizations as a worst case estimator of MPN for SMF and MMF channels.

2.4 Fiber Optic Communication

2.4.1 *Communication Channel Model*

The physical description of the short-range communication system is interesting, but it is useful to present a simplified mathematical model, which can be used for modulation format design. Such a model, presented also in [62], is illustrated in Fig. 2.6. The modulator maps the symbols u(k), at an instant k to a waveform x(t). The received signal is y(t) and can be written as:

$$y(t) = x(t) + n(t) \tag{2.35}$$

where n(t) is the added noise. The demodulator uses y(t) to provide an estimate of u(k), which is denoted ˆu(k).

There is a non-negativity constraint on the signal x(t), since it is used to modulate the

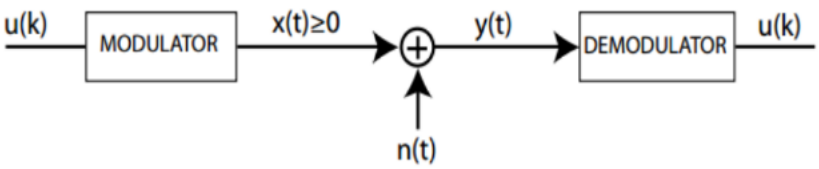

Fig. 2.6: Block diagram of a simplified channel

directly modulated laser. The laser operates only if it is forward biased, and thus the driving signal must be non-negative.

From 2.3.2, it follows that the main noise source is the thermal noise. This type of noise can be characterized statistically as AWGN [63, Sec. 1.3] and therefore the considered system can be treated as an AWGN channel with non-negativity constraint. It should be noted that there is no non-negativity constraint on y(t). This channel model has been analyzed in detail in the communications literature, e.g. [64, 65].

2.4.2 *Modulation*

As the baud rate of short-range optical connections increase, they become increasingly limited by the component bandwidth and modal dispersion in the MMF which limits the usable distances. In this case, the industry has turned to parallel interconnects, such as those defined in the IEEE 802.3 standard, in which 40Gbps and 100Gbps links are created by aggregation of 10Gbps and 25Gbps links. In effect, each link uses eight or twenty fibers in parallel, since a pair of fibers is needed for bi-directional communication. This has an advantage of keeping the transmission distances reasonably long, but it has the disadvantage of increasing the physical size of the interconnects. New designs reducing the size of the interconnects are being developed [66, 67]. Multilevel modulation formats can be used to increase the bit rate in each of the parallel lines, multiplying the achievable throughput. The increased spectral efficiency would primarily enable squeezing more data into the limited electrical bandwidth, without increasing the number of lasers, detectors, and drivers. There are, however, some constraints to consider the typical link power budgets and wall-plug power consumption are limited. This means, that a modulation format with high spectral efficiency, good sensitivity and low complexity is needed. It is very hard to optimize all the three conditions at the same time, especially in an IM/DD system, where the available signal space is limited by the non-negativity constraint. The problem becomes easier if restricted to two parameters at a time, for example spectral efficiency and complexity, or spectral efficiency and sensitivity. If implementation in the short term is considered, it is important to keep the modulation formats simple to design at high baud rates, given the constraints of today's electronics. It is interesting to consider beyond short term constraints and investigate what would be a good modulation format to

i.e. maximize the sensitivity, without keeping strict hardware constraints. While application of digital signal processing (DSP) at high speed is difficult and implies high power consumption today, Moore's law still applies and new possibilities might emerge in the future. Analog electronic equalization was discussed for short-range applications using both OOK [68] and was shown practically in [69], multilevel modulation formats were discussed in [70, 71], and electronic equalization is already used in active copper cable [72]. In the last example, the electronic equalization reduces the requirements for quality of the copper cabling, increases the transmission distance and reduces the cost. Once the complexity constraints on the electronic processing are moved into a background plane, we can consider optimization of more advanced modulation formats for improved sensitivity in IM/DD systems. In this work a few modulation formats are covered; simple modulation formats such as PAM, interesting for high-speed applications, and partial-response duobinary. These will be discussed separately throughout the thesis. Other signal spaces based on different basis functions are possible, as long as the non-negativity constraint is fulfilled. An example of such a modulation format is pulse position modulation, which is commonly used in wireless infrared communications [65]. This type of modulation is very power efficient, but has rather poor spectral efficiency, so prospects of use in links based on MMF are weak.

2.4.3 *Pulse Amplitude Modulation*

Pulse amplitude modulation is the simplest modulation format applicable for IM/DD systems, such as short-range optical communications. In fact, OOK (sometimes called NRZ) is a special case of PAM, with 2 modulation levels, each representing one bit.

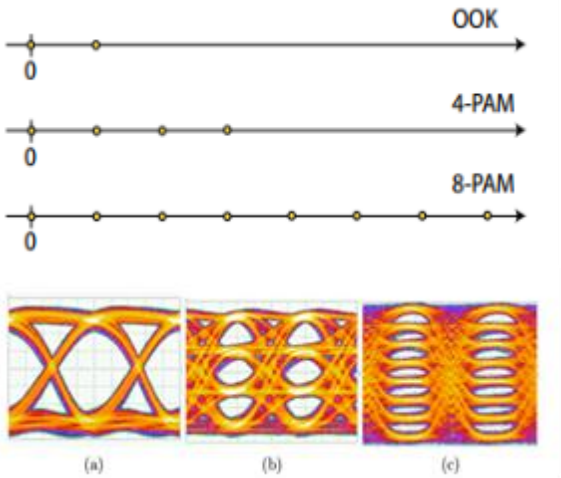

Fig. 2.7: Comparison of different PAM-M constellations and their eye diagrams; (a) OOK, (b) PAM-4, (c) PAM-8

There is only one basis function in PAM, in the simplest case it is just a rectangular (unshaped) pulse,

$$\Phi_0(t) = \frac{1}{\sqrt{T}} rect(t/T) \tag{2.36}$$

where T denotes symbol time duration. For an M-level PAM the symbol waveforms may be represented as

$$s_m = A_m \phi_0(t) \tag{2.37}$$

where 1 < m < M. Note that this describes the optical intensity profile of the pulse, rather that the electrical field amplitude. The non-negativity constraint means also that negative values of s_m are not allowed and therefore all A_m values must be positive. An illustration of constellation diagrams for OOK, PAM-4, and PAM-8 are shown in Fig. 2.7. Since there is only one basis function, the constellation diagram can be presented on one axis. For comparison, constellation diagrams of conventional PAM in systems without non-negativity constraint are included in Fig. 2.7. It is also easy to illustrate the PAM modulation in the time domain. Examples of experimental OOK, PAM-4 and PAM-8 eye

diagrams are illustrated in Fig. 2.7. Eye diagrams are simple and useful tools for getting a quick overview of signal quality and impairments in the system. Both SNR and timing jitter can be observed from eye diagrams. Lower SNR is manifested by broadened signal levels, and timing jitter is manifested by the widened eye crossings. It is also obvious from the eye diagrams that the more modulation levels there are, the higher is the required SNR to achieve error-free data transmission.

2.4.4 *Theoretical BER Calculation*

As the number of modulation levels is increased, the spectral efficiency increases. If the bit rate is kept fixed, the bandwidth of M-level PAM is reduced by a factor of $\log_2$ (M), compared to OOK [73]. Alternatively, the symbol rate and bandwidth can be kept fixed and the bit rate increased. In either case, PAM-M will require more optical power at the receiver to reach the same BER as OOK. It is useful to have an analytical expression for the expected system BER, as a function of the received optical power. Knowledge of the theoretically expected performance enables not only comparison with other modulation formats, but also proper evaluation of the experimental results and implementation penalties. If the SNR is high and the noise is Gaussian, the BER can be approximated as:

$$BER \approx \frac{M-1}{M} \frac{d_{avg}}{\log_2 M} erfc\left(\frac{I_{avg}}{(M-1)\sigma\sqrt{2}}\right) \tag{2.38}$$

where I_{avg} is the average photocurrent, σ is the noise variance and d_{avg} is the average Hamming distance between the labels of adjacent symbols. If Gray labeling is used, d_{avg} = 1. If natural labeling is used it is given by:

$$d_{avg} = 2 - \frac{\log_2(M)}{M-1} \tag{2.39}$$

In the case when the bit rate is fixed and the modulation order is increased the optical power penalty for using M-level PAM, compared to OOK, expressed in dB is:

$$P_{pb} = 10\log_{10}\left(\frac{M-1}{\sqrt{\log_2 M}}\right) \tag{2.40}$$

where M is the number of modulation levels [73]. If the symbol rate is fixed, the optical power penalty compared to OOK is [74]:

$$P_{ps} = 10\log_{10}(M-1) \tag{2.41}$$

There is a trade-off between power efficiency and bandwidth efficiency. However, if high speed components such as integrated photoreceivers are not available, then the penalty for use of photodetectors with voltage amplifiers, rather than transimpedance amplifiers outweighs the power penalty due to increased number of levels. Because of the relaxed bandwidth requirements on components, multilevel PAM modulation can be useful in extending the transmission distance. In fact, PAM was proposed also for increasing the transmission distance in SMF [73] and along with equalization for electrical backplane connections [75]. In short-range applications PAM, in particular with 4 levels has been discussed in the context of polymer fiber links [76, 77]. The possibilities of implementation, advantages and drawbacks of PAM applications in MMF and VCSEL based links were studied in [70, 78, 79].

One of the advantages of PAM is the simplicity of implementation. CMOS circuits operating at baud rates up to 56Gbaud have already been developed [80]. In a laboratory environment PAM signal can be generated in real time from binary signals. It is particularly simple for PAM-4 which can be generated by combining two clock aligned decorrelated

binary data streams. One of the streams must be half of the amplitude of the other to get PAM-4 at the output. Generation of PAM-4 signal with this method is difficult. Conceptually, only one more binary signal source is required. In reality, the signal quality generated with such a setup suffers from reflections in the power combiners. Precise signal phase control and amplitude is also required. A much better way to generate a PAM-4 or possibly PAM-8 signal is to use a dedicated circuit, such as an 8-bit digital to analog converter (DAC).

Experimental BER measurements can be also done in real time using a standard error analyzer designed for OOK. The decision threshold has to be set between the levels of PAM-4 and the error analyzer has to be programmed with a binary pattern corresponding to transitions of given PAM decision threshold. If the measured BER is low, it can be assumed that only symbol errors between neighboring levels occur. Thus, the calculation of the resulting BER can be greatly simplified. To calculate the theoretical BER values for PAM-M systems, consider the symbol error rate (SER) calculation. Assuming that all M symbols are equiprobable, the SER can be calculated in through:

$$SER = \frac{1}{M}\sum_{i=0}^{M-1}\sum_{j=0,i\neq j}^{M-1} P_{ij} \tag{2.42}$$

where P_{ij} is the probability of receiving symbol j when symbol i was transmitted [63, Ch. 4.2]. Assuming Gaussian noise, this probability is found as:

$$P_{ij} = \frac{1}{2} erfc\left(\frac{I_{th,j}-I_i}{\sigma_i\sqrt{2}}\right) - \frac{1}{2} erfc\left(\frac{I_{th,j+1}-I_i}{\sigma_i\sqrt{2}}\right) \tag{2.43}$$

Here, I_i denotes the photocurrent at symbol i, and $I_{th,j}$ is the threshold current, where $I_{th,0} = -\infty$, and $I_{th,M} = +\infty$. The remaining decision thresholds are located between the subsequent

symbols. The root mean square (RMS) value of the noise current at the symbol i level is denoted σ_i.

The BER is dependent on the labeling of the symbols. The Gray labeling usually provides the best performance [81], but sometimes in experiments it is easier to implement natural labeling. In general, the BER can be expressed as:

$$BER = \frac{1}{M}\sum_{i=0}^{M-1}\sum_{j=0,i\neq j}^{M-1}\frac{d_{ij}}{log_2(M)}P_{ij} \tag{2.44}$$

where the d_{ij} is the Hamming distance between the labels of symbols i and j [81]. Assuming that the thermal noise is dominating, all symbol levels are equally spaced, and the decision thresholds are equidistant from adjacent symbols, the SER can be expressed as:

$$SER = \frac{M-1}{M}erfc\left(\frac{I_{avg}}{(M-1)\sqrt{2}\sigma}\right) \tag{2.45}$$

where I_{avg} is the average photodetector current and $\sigma = \sigma_i$ for all i is the RMS noise current. For high signal to noise ratios (SNRs), it can be assumed that only errors between adjacent symbols occur. In that case, the BER can be approximated as:

$$BER_{approx} \approx \sum d_{ij}\frac{SER}{log_2(M)} \tag{2.46}$$

The BER can be calculated from the SER values, in high-SNR regime for the naturally coded PAM-4 signal [82]:

$$BER = \frac{1}{2}SER_{bot} + SER_{mid} + \frac{1}{2}SER_{top} \tag{2.47}$$

And for the Gray labeled PAM-4 signal [82]:

$$BER = \frac{1}{2}SER_{bot} + \frac{1}{2}SER_{mid} + \frac{1}{2}SER_{top} \quad (2.48)$$

An alternative to this method would be to use a real-time sampling oscilloscope to capture the received waveform and calculate the BER offline. The error analyzer based approach has the distinct advantage of enabling BER measurements down to 10^{-12}, which is important for data communications applications. The lowest BER that can be reached using off-line processing in a reasonable time (less than 24 hours) is around 10^{-7}. The ability to reach low BER is important because until recently FEC was not accepted in data communication applications. On the other hand, offline BER measurement would be advantageous in case higher-order PAM, with 8 and more levels, since the manual adaptation of the threshold for each measurement is time consuming.

2.4.5 *Effects of RIN on PAM-M*

It is clear how the BER depends on the received optical power, if the main noise source is the thermal noise, which in general is AWGN. However, it is not always the thermal noise that dominates. The system performance can be dominated by RIN originating in the laser, which is dependent on the received optical power. In this case, increasing the optical power into the receiver does not mean that a lower BER will be reached because the increase received signal power will be accompanied by higher noise power.

The effects of RIN can be evaluated analytically, by taking it into account in the noise variance when calculating the BER. Examples of BER curves for PAM-4, also with 30 GHz noise bandwidth, with RIN in range from −150dBm/Hz to −134dBm/Hz are included in Fig. 2.8. It was assumed that the decision thresholds are equidistant from the adjacent symbol levels.

As the RIN levels are increased, the BER curves start showing progressively higher error floors. Naturally, an increased number of levels reduces the RIN level that can be tolerated.

2.4.6 *Intersymbol Interference*

Intersymbol interference (ISI) occurs when one symbol interferes with subsequent symbols. The sampled received signal values have a form [63, Ch. 9.2]

$$y_k = I_k x_0 + \sum_{\substack{n=0 \\ n \neq k}}^{\infty} I_n x_{k-n} + v_k \tag{2.49}$$

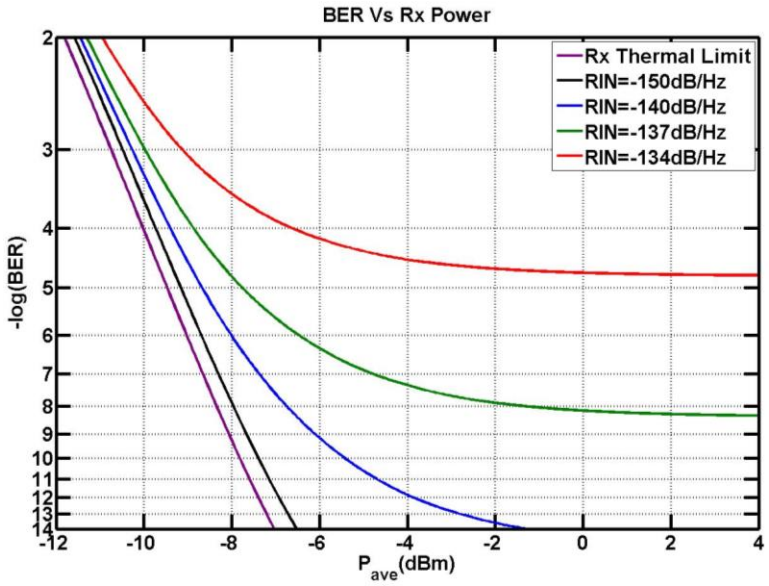

Fig. 2.8: Simulated BER curves of PAM-4 with varying RIN and extinction ratio of 4dB.

where I_n denotes the transmitted symbols, x_n denotes the response of the system, and ν_k is the noise variable. The desired term, corresponding to the transmitted symbol is represented by I_k, the term x_0 can be treated as a scaling factor. The second term on the right hand side is the undesired interference. The effects of ISI on PAM signals can be visualized using an eye diagram. An example simulated PAM-4 eye diagram after transmission through a channel with Gaussian impulse response with a 3dB bandwidth three times higher than the symbol rate is show in Fig. 2.9. For comparison, an eye diagram of the same format, but in a channel with 3 dB bandwidth equal to 0.6 of the symbol rate is shown in Fig. 2.9. There are two kinds of penalties introduced by the ISI, power penalty and timing penalty. Power penalty is due to the vertical eye closing, and the timing penalty is due to the horizontal eye closing.

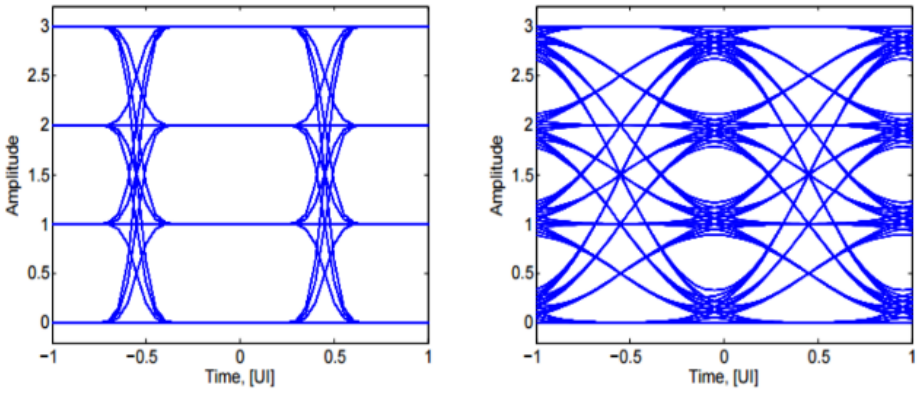

Fig. 2.9: PAM-4 Eye diagrams with different channel bandwidths.

The power penalty due to the ISI is well understood for OOK systems. The basic ISI penalty calculation methods, have been outlined in [83]. The ISI power penalty, expressed in dB, for any PAM formats is

$$P_{ISI} = 10\log_{10}\left(\frac{1}{1-E_m}\right) \tag{2.50}$$

where E_m is the worst case eye closure. In case of OOK it is approximated as

$$E_{m,OOK} = 1.425 \exp\left(-1.28\left(\frac{T}{T_c}\right)^2\right) \quad (2.51)$$

The bit period is denoted as T and the channel 10% – 90% rise-time is denoted as T_C. This ISI penalty calculation method, which is valid under assumption of a Gaussian channel response and rectangular input pulse, was given in [84]. It is used in the IEEE 802.3 link budget spreadsheet [85].

Methods of calculation of the 10% – 90% rise-time for a given system are described in [84]. The ISI penalty estimates can be extended to PAM-4. A PAM-4 eye diagrams contains three OOK eye diagrams stacked on top of each other.

Assuming that the channel response is Gaussian, it is easy to observe that for the same system rise-time and symbol rate, the eye closure in case of PAM-4 is twice as large as in the case of OOK. In general, for a PAM-M format the eye closure will be:

$$E_{m,PAM-M} = \frac{M}{2} 1.425 \exp\left(-1.28\left(\frac{T}{T_c}\right)^2\right) \quad (2.52)$$

In a simplistic view of a digital communication system if one wishes to increase the spectral efficiency, the only solution is to increase the number of modulation levels. In reality, it may be easier and cheaper to increase the signaling rate beyond the channel 3dB bandwidth and accept the resulting ISI penalty or to use equalizers. From the point of view of sensitivity, it is logical to switch to a higher order modulation format at the point when the ISI penalties for a lower order format are larger than the penalty for using more levels. This situation is illustrated in Fig. 2.10, where sensitivity penalties for OOK and PAM-4 are

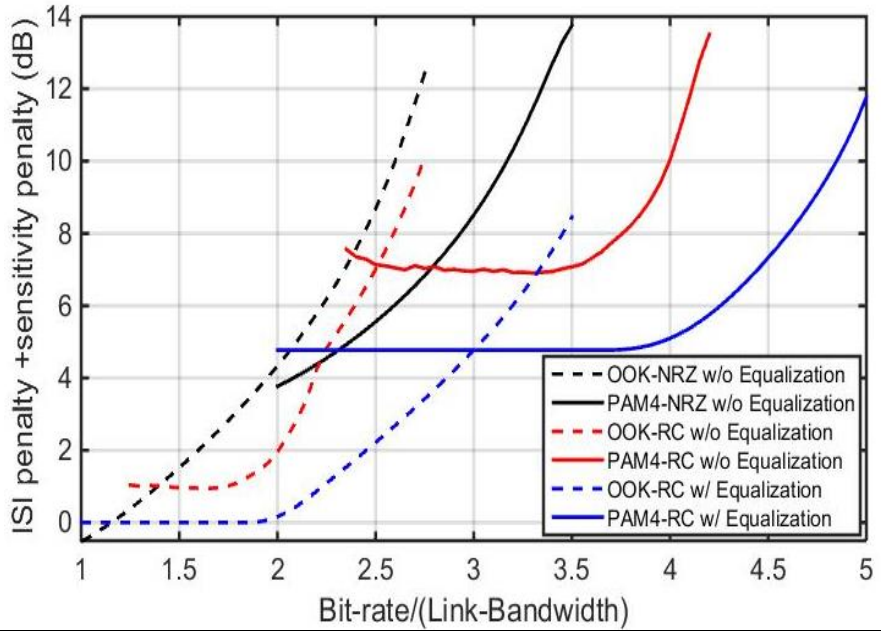

Fig. 2.10: ISI penalty for various modulation formats and transmit pulse shaping.

plotted against the ratio of the data rate to the channel 3dB bandwidth. The reference point for the power penalties is a sensitivity of and OOK system at data rate equal to the channel 3dB bandwidth. We examine systems with no equalization, equalization and equalization with raised cosine pulse shaping. The ISI penalties for OOK do not exceed the sensitivity penalty for going to PAM-4 until the point when the bit rate is two times larger than the system bandwidth. As more equalization is added to the system, it can take up to three times the system bandwidth before OOK exceeds the sensitivity of moving to PAM-4.

2.5 Equalization, Pulse Shaping, and Forward Error Correction

2.5.1 Equalization

Based on the VCSEL and fiber characterization, the power penalties due to ISI from CD, MD, laser bandwidth and laser-fiber interactions can be fairly significant. Owing to high attenuation values compared to silica-based optical links, the penalty due to the ISI

could be highly detrimental to the performance of MMF-based links. The power penalties due to the deterministic ISI effects can be compensated using a simple analog equalizer with modest number of taps. The tap-length of the equalizer is an indication of the complexity in analog circuitry required to implement the structure and hence of the cost of implementing the system [86], [77]. In this work, a digital implementation of the analog linear equalizer has been used to compensate for the dispersion-induced ISI. This can take place at the transmitter and/or receiver. The linear equalizer, also called a feed-forward equalizer, consists of a simple finite impulse response (FIR) structure whose tap weights are adjusted to compensate for the channel distortion [88], [89]. Typically, two kinds of FFE structures are available: 1) Symbol-spaced equalizer, where the filter taps are separated by one whole symbol period; and 2) Fractionally-spaced equalizer in which the tap-spacing is some fraction of the symbol period 'T'. The output of a T/K-spaced fractional feed forward equalizer is given by [8]:

$$y(t) = a_{-N}Rx\left(t + \frac{NT}{K}\right) + \cdots + a_{-1}Rx\left(t + \frac{T}{K}\right) + a_0Rx(t) +$$

$$a_1Rx\left(t - \frac{T}{K}\right) + \cdots + a_{+N}Rx\left(t - \frac{NT}{K}\right) \tag{2.53}$$

where a_{-N} … a_{-1}, a_0, a_1… a_{+N} are the filter tap weights, $Rx(t)$ is the unequalized received signal which is given as input to the FFE and 'K' represents the fractional delay between the taps. Note that +N does not have to equal –N, i.e. the filter needs not be symmetric. The filter tap weights are tuned adaptively to match the output to a known training sequence by least mean-squares (LMS) algorithm [83] with a given step-size. Once, trained the filter weights are static throughout the optic communication.

2.5.2 Pulse Shaping

Throughout the work presented in this thesis, raised cosine (RC) pulse shaping is investigated, where the frequency response $H_p(f)$ of the RC filter has the conventional form:

$$H_p(f) = \begin{cases} T, & |f| \le \frac{1-\beta}{2T} \\ \frac{T}{2}\left[1 + \cos\left(\frac{\pi T}{\beta}\left[|f| - \frac{1-\beta}{2T}\right]\right)\right], & \frac{1-\beta}{2T} < |f| \le \frac{1+\beta}{2T} \\ 0, & otherwise \end{cases} \quad (2.54)$$

In Eq. (2.54), T is the symbol period, while β is the roll-off factor. The ISI penalty is data rate dependent and is the ratio of the eye height without ISI to that with ISI. It represents the extent to which the signal power would have to be increased in order to compensate for the reduced noise margin, arising from an ISI induced closing of the eye. As stated before, the ISI penalty is [83]:

$$P_{ISI} = 10\log\left(\frac{1}{1 - E_m}\right)$$

where the eye closure penalty can also be expressed as:

$$E_m = M\left(1 - \int_{-\infty}^{-BW_{EQ}} H_p H_c H_r \exp(j2\pi f t_o)\, df \; - \right.$$

$$\left. \int_{-BW_{EQ}}^{BW_{EQ}} H_p H_c H_{E,Tx} H_{E,Rx} H_r \exp(j2\pi f t_o)\, df \; - \int_{BW_{EQ}}^{\infty} H_p H_c H_r \exp(j2\pi f t_o)\, df\right) \quad (2.55)$$

where t_o is the sampling instant and M is the number of levels in the signaling. One of the advantages of employing RC pulse shaping rather than unshaped (UnS) rectangular NRZ pulses is that its lower bandwidth requirement ensures a lower ISI penalty in a bandwidth constrained optical link. Hence, Eq. (2.55) may be simplified as follows:

$$E_m = M\left(1 - \int_{-BW_{EQ}}^{BW_{EQ}} H_p H_r \exp(j2\pi f t_o)\, df\right) \quad (2.56)$$

Thus, unlike the noise enhancement penalty, the ISI penalty does not depend on how equalization is split between the transmitter and receiver, but depends on the net equalization, namely it depends on $H_{E,Tx}H_{E,Rx}$. Employing higher modulation formats like PAM-4 additionally result in sensitivity penalty:

$$P_{mod} = 10\log(M-1) \tag{2.57}$$

Clearly, employing higher modulation formats are justified when the loss in sensitivity is compensated by the reduced ISI penalty owing to the lower signal bandwidth.

Unshaped NRZ pulse shaping with equalization, near-brick wall receiver filtering and optimum sampling at $t_o = 0$ results in an eye closure penalty of:

$$E_m = M\left(1 - \int_{-BW_{EQ}}^{BW_{EQ}} H_p df\right) \tag{2.58}$$

Eq. (2.58) shows $E_m < 0$ for certain low values of bitrate/(link-bandwidth), where this is due to the presence of an overshoot, as shown in the simulation results of. This occurs due to a concentration of the pulse energy at the center of the pulse for these values of bitrate/(link-bandwidth). It should be noted that this is never observed, because it is an artifact of the near infinite bandwidth of an ideal unshaped pulse.

The actual shape of the received nominally unshaped pulse depends on the total channel bandwidth. Therefore, we refer to these pulses as PAM-2 (VCSEL modulation is distinctly not OOK). Furthermore, we use our measured channel response and denote the received waveform after propagation through our channel as unshaped (UnS). Note that the IEEE 802.3 standard assumes the transmitter employs Gaussian pulse shaping and overall impulse response of the MMF link to be Gaussian shaped.

2.5.3 Equalizer Noise Enhancement

A drawback of using equalizers is that they enhance the system noise while correcting channel impairments. Consider the measured combined optical transmitter, fiber and optical receiver response, $H_c(f)$. The MMF link, which is dominated by the VCSEL response, is shown to be closely approximated by a Gaussian behavior, where the frequency response of an m[th] order Gaussian is exp $((f/f_o)^{2m})$. The noise penalty then needs to be determined with a receive filter $H_r(f)$, a noise spectral density N(f) and frequency responses $H_{E,Tx}$ and $H_{E,Rx}$ for the transmitter pre-emphasis and receiver post-equalization, respectively. Pre-emphasis and post-equalization jointly compensate for the channel response for frequencies up to some BW_{EQ} due to hardware or SNR limitations, i.e. equalization compensates such that $H_{E,Tx}H_{E,Rx} = \frac{1}{H_c}$ for frequencies up to BW_{EQ}.

The optical power penalty due to noise enhancement is the ratio of the noise power before and after receiver post-equalization [83]:

$$Penalty_{noise} = 5\log\left(\frac{\int_0^{BW_{EQ}} N_2|H_r|^2|H_{E,Rx}|^2 df + \int_{BW_{EQ}}^{\infty} N_2|H_r|^2 df}{\int_0^{\infty} N_1|H_r|^2 df}\right) \quad (2.59)$$

where,

$$N_1 = N_{thermal} + N_{RIN} + N_{ADC} + N_{DAC} \quad (2.60)$$

$$N_2 = N_{thermal} + N_{RIN} + N_{ADC} + \widetilde{N}_{DAC} \quad (2.61)$$

where N_{RIN} and N_{DAC} are Power Spectral Densities (PSDs) of the RIN and DAC quantization noise added at the transmitter, N_{ADC} is the PSD of the ADC quantization noise

added at the receiver, while $N_{thermal}$ accounts for the all the thermal noise added by the link shown. It should be noted that $\widetilde{N}_{DAC}$ is the PSD of the DAC quantization noise after pre-emphasis. In this theoretical analysis, the digital receive filter is presumed to have the same bandwidth limitation as the equalizer, i.e. BW_{EQ}, and an ideal low-pass filter shape. Hence the second term in the numerator of Eq. (2.59) is negligible.

A DAC (8-bit architecture) imposes significant white noise resulting in an effective number of bits (ENOB) of ~5.2. The RC pulse shaping and subsequent pre-emphasis are done in the digital domain with 8-bit resolution and prior to the DAC. Hence, any quantization noise added by this filtering process is overwhelmed by the white thermal noise imposed by the DAC and the subsequent link components.

Similarly, a typical ADC has an architecture of 8 bits and an ENOB of ~4.5-5, also exhibiting a white noise behavior. Modern wideband DACs and ADCs are typically dominated by thermal noise and that quantitation noise and jitter are not the limiting noise sources. Thus, these devices exhibit white noise and an ENoB that is essentially frequency independent.

Furthermore, it is reasonable to model RIN and shot noise as having white PSDs. Hence, the experimental link has a net noise which is not quantization noise limited and has a near-white PSD. Note that the minimum ENOB requirement to avoid a quantization penalty for a four level modulation format is ~3.8 [91]. Thus, the noise spectrum of Eq. (2.59) can be assumed to be white with $N_1 \approx N_2$.

Equations () reveal that if the link is not limited by the bit resolution of the DAC, then the DSP induced noise enhancement is mostly a result of the receiver post-equalization

and not transmitter pre-emphasis. In such a case, $H_{E,Rx} = 1$ and $H_{E,Tx} = \frac{1}{H_c}$. On the other hand, the noise enhancement is maximum (worse case noise enhancement) when the entire channel compensation is done at the receiver, i.e. when $H_{E,Tx} = 1$ and $H_{E,Rx} = \frac{1}{H_c}$.

2.5.4 Forward Error Correction

The Reed-Solomon (RS) codes, introduced in 1960 [92], are one of the most popular classes of error correcting codes, used in many communication technologies. Hardware implementations of RS codes have been studied and optimized over many years. The performance of RS FEC was investigated e.g. in [93].

The RS code with n-symbol-long codewords, each symbol of length q bits, can correct t = (n − k)/2 symbol errors, where k is the number of payload data symbols. The code rate is k/n. For the common RS(255,239) code, n = 255, k = 239, t = 8 and q = 8. The rate is 239/255 = 0.94 and the overhead is 16/239 = 6.7%. The error rate at the output of the decoder can be calculated as a function of the bit-error rate at the input of the decoder. Assuming that the error probability at the input BER_{in} is independent over all the bits in the FEC codeword, the incoming symbol error rate is:

$$SER_{in} = 1 - (1 - BER_{in})^q \tag{2.60}$$

Under assumptions that the decoder corrects all errors up to t symbols and detects all errors above t symbols, the symbol error rate at the output of the decoder is [94, Ch. 8]:

$$SER_{out} = \frac{1}{n}\sum_{i=t+1}^{n} i\binom{n}{i} SER_{in}^{i}(1 - SER_{in})^{n-i} \tag{2.61}$$

The output bit-error rate can be calculated from the output symbol error rate by inverting the step:

$$BER_{out} \approx 1 - (1 - SER_{out})^{1/q} \tag{2.62}$$

The overhead for a Reed-Solomon (RS) error correction has been included in the raw link speed. Several considerations are taken for choosing an appropriate FEC including: total latency, overclocking, and implementation penalty. We assume the RS (544, 514, 15, 10) FEC code will be implemented, which is in accordance with IEEE 802.bm standards for PAM-4 [95]. An over-clocking rate of 3 percent is included in all data that uses RS FEC. Since all equalization is not feed-forward (FFE), we count errors to ensure that they are random. The result is an effective coding gain of 6.5dB [95].

CHAPTER 3.

EFFECTS OF VCSEL MODE COMPETITION ON FIBER COMMUNICATION SYSTEMS

The growing demand for bandwidth in short reach optical links has resulted in a need to increase the data rates of multimode fiber links [96], [97]. As long-haul and metro fiber optic links have begun deploying 100GbE systems, the need to upgrade short-reach optical links for local and storage area networks to keep pace has prompted the development of 400G Gigabit Ethernet standards. One prominent standard developed is 400GBASE-SR16, utilizing 16 parallel ~25 Gbps lanes with vertical cavity surface emitting lasers (VCSELs) over multimode fiber (MMF). Some investigations on VCSEL-based MMF links have indicated that the MPN penalty is a limiting noise factor for realizing longer reaches of MMF links [61]. Currently, the IEEE 802.3bs standard link model uses a worst-case k_{mpn} parameter of 0.3 which makes the MPN penalty contribution significant to the total penalty of the link [2], and suggests that links of 50Gbps over >100m are nearly impossible due to the noise penalty. For this reason, it was important to study the noise characteristics of VCSELs and factors effecting it in more detail. MMF must be treated from a statistical perspective due to variations in modal bandwidth that result from the interaction of the VCSEL-launched fiber mode power distribution (MPD) with the fiber's differential modal delay (DMD), both of which exhibit significant variation while remaining within their respective specifications [45, 98].

The performance of VCSEL-based optical links is mainly limited by the penalty due to dispersion and penalty due to the noise in the VCSEL output. VCSEL noise has two

aspects to it: Fluctuations in the composite power output or the relative intensity noise (RIN) and random fluctuations of optical power among different transverse modes of the VCSEL. The multi-mode nature of VCSELs used in data centers and LANs results in random fluctuations among the different transverse modes due to mode competition [4, 57]. These random fluctuations manifest as a random timing jitter due to the wavelength-dependence of the group velocity which is different for different modes. This random jitter results in an amplitude variance at the optimal sampling instant, and is referred to as mode partition noise. Ogawa [57] proposed, using simplified assumptions, a simple model to estimate the variance due to MPN in single-mode and multi-mode fiber links which was then used by Agrawal [59] to derive closed-form expressions for the power penalty due to MPN under additional idealizing assumptions. This extended Ogawa-Agrawal (O-A) model is the basis for the model used by the IEEE standards group to estimate high-speed VCSEL-based MMF link performance [4]. It uses major assumptions which are listed in 2.3.3, but here we will focus on:

1) The composite power in all modes of a laser at any given instant in time is constant

$$\sum_{i=1}^{N} a_i = 1 \tag{3.1}$$

2) The cross-correlation parameter, γ_{cc} of the power fluctuations between any two modes of the laser is constant

$$\gamma_{cc} = \frac{\langle a_i a_j \rangle}{\langle a_i \rangle \langle a_j \rangle} = \text{constant for all } i \neq j \tag{3.2}$$

3) The power in a given mode remains constant throughout the duration of a bit period.

The variance for the normalized power in each mode is thus calculated by the O-A model in a heuristic manner following above assumptions [58] without any consideration of the physical basis of how the modes actually fluctuate inside a laser. For a VCSEL, however, the lasing transverse modes continuously compete for gain in the active region. Consequently, the extent of intensity overlap between the spatial distributions of any two modes is a primary factor determining the cross-correlation coefficient (r_{ij}) of those modes. Thus, the random fluctuations among different VCSEL modes result from a complicated interaction of mode profile and various mode-coupling mechanisms. Additionally, these correlations in the mode power fluctuations impact the value of RIN for the device. Thus, each of the assumptions 1) - 3) are violated when the standard MPN model is applied for VCSELs.

Another assumption in the O-A model for MPN is that the modes in a VCSEL are all anti-correlated. Our experiments [9] showed different k_{mpn} measured from the statistics in each transverse mode of an 850nm VCSEL, contrary to the standard model assumption. Similar experiments have measured the correlated fluctuations between polarization modes of a VCSEL [99], and correlations between transverse modes of an optically injected VCSEL [100]. However there has never been an experimental demonstration of accurately measuring the cross-correlations and determining the actual k_{mpn} parameter.

In this Chapter, we develop a novel method to measure the cross-correlations between transverse VCSEL modes. The cross-correlations are then used to recalculate k_{MPN}

values for two different VCSEL wavelengths. We then determine that the RIN of the laser is actually fiber dependent, and demonstrate how the RIN increases with fiber transmission. Based off these findings, we study how fiber effects VCSELs with different numbers of optical mode sets ranging from 3 to 10 and determine there could be an optimum number of modes for a VCSEL and thus an optimum aperture size.

3.1 Noise in VCSEL Based Links

Through a novel measurement system, we reported direct measurement of correlation properties of transverse modes for VCSELs of different wavelengths. We demonstrated that VCSELs have low k_{mpn} with all measurements <0.06, consistent with link experiments using multimode VCSELs coupled through multimode fiber. This finding demonstrates the use of k=0.3 is very conservative and a lower worst case of 0.15 is justified, as well as indicating that data rates beyond 50Gbps are possible. We investigate both 850nm and 900nm VCSELs

3.1.1 Covariance and Correlation Properties among VCSEL Modes

The full statistics of mode-fluctuations in a VCSEL lasing with 'M' transverse modes can be completely described by a covariance matrix (COV) of the normalized instantaneous mode powers $\{a_i\}_{i=1}^{M}$ having dimensionality (MxM) [14]:

$$COV\{a_i\} = \begin{bmatrix} var1 & cov12..cov1M \\ cov21 & var2\ ..\ cov2M \\ & . \\ & . \\ covM1 & covM2..varM \end{bmatrix} \tag{3.3}$$

Here, vari $= \langle a_i^2 \rangle - \langle a_i \rangle^2$ is the variance of the fluctuation from mean value of the ith VCSEL mode and covij $= \langle a_i a_j \rangle - \langle a_i \rangle \langle a_j \rangle$ is the covariance of modes i and j. Note that, unless stated otherwise, all references to modes in the rest of this paper refers to the transverse modes of the VCSEL. The notation $\{ai\}_{i=1}^{M}$ is the same as that used in O-A model with the exception that the instantaneous sum of the mode powers is no longer assumed constant, e.g., $\sum_{i=1}^{M} ai \neq 1$. Instead, we assume that $\sum_{i=1}^{M} \overline{\langle a_i \rangle} = 1$, i.e. the sum of the average mode powers is constant. The COV matrix completely captures the noise properties of a laser.

The cross-correlation of the noise can be calculated using the COV matrix and normalized statistical expression:

$$R_{ij}(\tau) = \frac{\langle a_i(t) a_j(t+\tau) \rangle - \langle a_i \rangle \langle a_j \rangle}{\sigma_i \sigma_j} = \frac{cov_{ij}(\tau)}{\sigma_i \sigma_j} \tag{3.4}$$

where $a_i(t)$ represents the normalized ($\sum \langle a_i \rangle = 1$) instantaneous optical power in the ith mode, $a_j(t+\tau)$ is the time-delayed version of the instantaneous power in the jth mode, $< >$ is the time average operator, and σ_i, σ_j are the standard deviations of the $a_i(t)$, $a_j(t)$. The resulting Rij(τ) ranges between -1 to 1, and is a measure of the correlation between noise in ith and jth modes, where -1 represents a pure anti-correlation and 1 represents a pure correlation.

It has been recognized that chromatic dispersion and DMD can act in a compounding or compensating fashion [9]. At these wavelengths, the fiber has normal chromatic dispersion (Dispersion parameter, D <0), with the higher order VCSEL modes (shorter wavelengths) exhibiting lower group velocity than the lower order VCSEL modes

(longer wavelengths). Additionally, higher order VCSEL modes tend to couple more efficiently to higher fiber modes leading to mode spectral bias. Thus, so called left sloped DMD (L-MMF, higher order fiber modes arriving earlier than lower order VCSEL modes) can experience a compensating effect between CD and DMD when a VCSEL with multiple modes is employed. Right sloped fiber (R-MMF) on the other hand tends to have both CD and DMD act to delay the higher modes (shorter wavelengths). Thus, we distinguish between these two types of fibers, which may be characterized by the same EMBc but still yield different net dispersion.

For both the 850nm and 900nm VCSELs, correlations were calculated from the measured variances and covariances for all mode pairs in a back to back link and with two different 100m multimode fibers, a 2.05GHz-km EMBc L-MMF and a 2.10GHz-km EMBc R-MMF. The two fibers have identical attenuation of 0.88dB including coupling loss.

The 850nm VCSEL modes exhibit mostly anti-correlations, which decrease in strength with increasing mode number difference. The cross-correlations Rij(t) for two example mode pairs of the 850nm VCSEL biased at 8mA (2.16mW) are shown in Fig. 3.1.

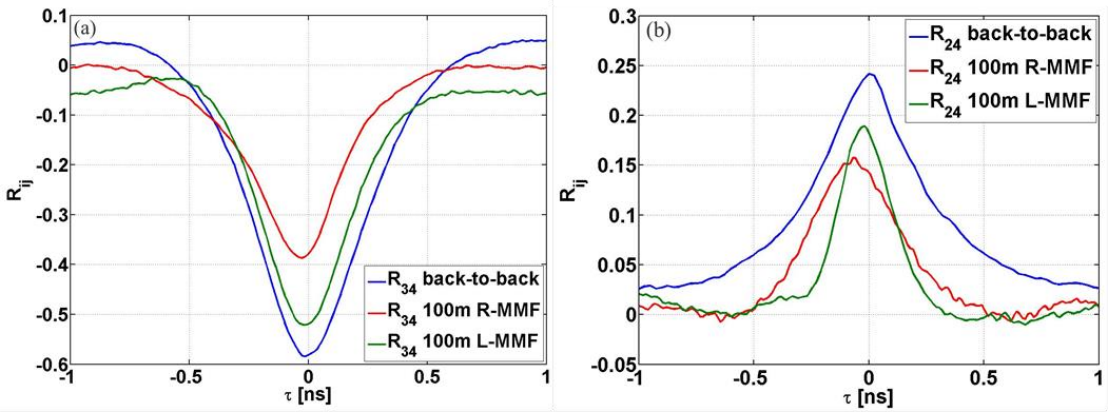

Fig. 3.1: (a) Cross-correlation of mode pair 3, 4 in back to back setup and after 100m of L-MMF and 100m of R-MMF; (b) Cross-correlation of mode pair 2, 4 in back to back setup and after 100m of L-MMF and 100m of R-MMF.

R_{34} exhibits anti correlation while R_{24} exhibits a positive correlation. For all back to back cases, the correlations peaked at the same t=0. The back to back (negligible dispersion) correlations decrease to ½ strength at t=0 within a few hundred picoseconds. This temporal duration of the correlation is related to the equilibration time of the gain medium.

Two observations from the measured correlations after fiber propagation were that firstly, the peak magnitudes shifted to t<0 and secondly the peak magnitudes were smaller. Following Eq (2), t<0 corresponds to the jth mode lagging the ith mode. Thus, when the correlation peaks at t<0 the jth VCSEL mode has experienced a slower average group velocity. The peaks themselves also decrease due to the net dispersion of the fiber. The R-MMF exhibit the most reduction, where this is consistent with the R-MMF having the larger net dispersion.

The temporal shift in peak correlation contributes to the decreased correlation experienced within any given symbol period since the symbol temporal width of 25Gbaud is small compared to the time scales of Fig. 3.1. In the case of the L-MMF, the peak cross-correlation shifts only slightly due to lower net channel dispersion from the counteracting DMD and CD effects. In contrast, the R-MMF has a significant shift due to the compounding effects of the DMD and CD. Mode 4 is seen to experience the largest average group delay.

Table 3.1 lists the τ=0 correlations for all mode pairs for btb and both L-MMF and R-MMF for the 850nm VCSEL. Each mode pair has its correlation reduced by at least 25% after propagation in 100m of fiber and in one case we observe that the mode pairs have become essentially uncorrelated. This decrease in correlation will necessarily impact the aggregate RIN which relies on anti-correlation between modes to reduce the RIN below

Table 3.1: 850nm Cross-Correlations (τ=0) at 8mA

	Back to Back	100m L-MMF 2.05 GHz-km	100m R-MMF 2.10 GHz-km
Modes	R_{ij}	R_{ij}	R_{ij}
1,2	-0.61	-0.58	-0.45
1,3	-0.16	-0.12	-0.04
1,4	-0.10	-0.07	~0
2,3	-0.25	-0.24	-0.10
2,4	0.24	0.18	0.15
3,4	-0.58	-0.52	-0.38

that of the sum of the individual variances and will be discussed in Section 3.1.3.

VCSEL and VCSEL-MMF behavior was also observed with 900nm VCSELs, Table 3.2, where 10mA (2.95mW) of bias was used to ensure 4 lasing VCSEL modes. For the 900nm VCSEL only the adjacent mode pairs are anti-correlated and all non-adjacent mode pairs are positively correlated. Mode pair 1, 4 is essentially uncorrelated. The additional positive correlations seen in the 900nm VCSEL will have an effect on the noise of the VCSEL and be discussed in Section 3.1.3. Similar to the 850nm VCSEL, we observe a reduction in correlation across all mode pairs after propagation through fiber with the R-MMF again yielding the larger reduction and both L-MMF and R-MMF producing a larger

Table 3.2: 900nm Cross-Correlations (τ=0) at 10mA

	Back to Back	100m L-MMF @850nm	100m R-MMF @850nm
Modes	R_{ij}	R_{ij}	R_{ij}
1,2	-0.44	-0.37	-0.29
1,3	0.20	0.13	0.06
1,4	0.01	~0	~0
2,3	-0.27	-0.19	-0.10
2,4	0.17	0.10	0.05
3,4	-0.25	-0.20	-0.14

reduction than that observed with the 850nm VCSEL. This is consistent with the expected larger net dispersion at 900nm in the MMF due to the anticipated larger DMD.

Higher capacity VCSEL-MMF links can be achieved using multi-level modulation while still retaining the simplicity of direct modulation and direct detection. Indeed, new deployments using PAM-4 are proposed [101, 102]. Each intensity level may have a different RIN and MPN resulting from the different photon density and different number of lasing modes. Therefore, we investigate the noise correlations over a wide range of bias to fully quantify the VCSEL noise properties and potential impact on link performance.

Using the 900nm VCSEL we determined the cross-correlations at 4 different bias points corresponding to 4 intensity levels of a PAM-4 format. The peak cross correlations of the 900nm VCSEL at these bias points are listed in Table 3.3. At the three lower bias

Table 3.3: 900nm Cross-Correlations at four Bias points

Back to Back	3.5mA	5mA	8mA	10mA
Modes	R_{ij}	R_{ij}	R_{ij}	R_{ij}
1,2	-0.28	-0.37	-0.63	-0.44
1,3	0.29	0.27	0.37	0.20
1,4	-	-	-	0.01
2,3	-0.49	-0.55	-0.60	-0.27
2,4	-	-	-	0.17
3,4	-	-	-	-0.25

currents 3.5mA, 5mA, and 8mA, only three modes exhibit measurable power. Furthermore, for these three modes, the anti-correlations and positive correlations increase as the bias increases and peak just as a fourth mode begins to lase. This drop in correlation with the introduction of the fourth mode is most likely linked to additional gain competition and spatial hole burning effects. Most importantly, the cross-correlations go through a

significant variation with bias indicating that there are large differences of MPN and RIN penalties among the different modulation levels.

3.1.2 K_{MPN} Calculations

The determination of kmpn as defined by O-A model is limited by our observations that VCSEL modes do not conform to the underlying assumptions of this model. However, we can estimate kmpn for those mode pairs that are anti correlated and can therefore provide an estimate of an effective kmpn that can be used to estimate link performance.

The O-A model enables kmpn to be calculated by two different methods [57]. First, as a two mode correlation (TMC) where in the MPN standard deviation is proportional to kmpn which can be written in terms of the back to back R_{ij} as:

$$k_{mpn}(\tau) = \sqrt{-R_{ij}(\tau = 0)}\sqrt{\frac{\sigma_i \sigma_j}{\langle a_i \rangle \langle a_j \rangle}} \tag{3.5}$$

Again, all modes are presumed anti-correlated [11], thus R_{ij} is presumed negative. The second square root represents the product of the standard deviations of modes i and j normalized to their respective powers. Ultimately, k_{mpn}, is a re-normalized correlation of the joint standard deviations of modes i and j. Lastly, the assumptions of the O-A model yield the same kmpn for all mode pairs used in Eq. (3.5). Clearly, for VCSELs this is not the case.

In the second method, kmpn is determined from the variance of a single mode (SMV). Originally derived heuristically by Ogawa, this is:

$$k_{mpn} = \sqrt{\frac{(\langle a_i{}^2 \rangle - \langle a_i \rangle^2)}{(\langle a_i \rangle - \langle a_i \rangle^2)}} \tag{3.6}$$

where the numerator represents the variance in the ith mode. In this form the real time data a_i must be free of all correlated noise. Thus we remove the receiver noise (thermal and shot) and the measured aggregate RIN contribution. The denominator was calculated from measured time averaged power spectrum, $\{a_i\}$. The variance is then weighted with the $\{\langle a_i \rangle\}$. We include this method since it is the most commonly used to determine kmpn because it is experimentally convenient and allows for kmpn measurements with modulation.

Table 3.4: k_{mpn} for 850nm and 900nm VCSELs

Modes	k_{mpn} (TMC) 850nm	k_{mpn} (TMC) 900nm	Mode	k_{mpn} (SMV) 850nm	k_{mpn} (SMV) 900nm
1,2	0.052	0.038	1	0.040	0.031
1,3	0.024	-	2	0.050	0.029
1,4	0.020	-	3	0.057	0.017
2,3	0.035	0.019	4	0.026	0.028
2,4	-	-	-	-	-
3,4	0.059	0.024	-	-	-

The calculated kmpn for both the 850nm at 8mA and 900nm at 10mA are listed in Table 3.4. The absence of an entry in Table 3.4 indicates a mode pair that is uncorrelated or positively correlated. We observe that, although kmpn varies by method, mode pair and mode number, all determinations of k_{mpn} are less than 0.06 for both the 850nm and 900nm VCSELs. Thus, despite the variations of the k_{mpn}, all of the estimates are substantially lower than the worst case k_{mpn} of 0.3 used in the 802.3 IEEE standard and fiber channel standard [4]. In some cases, the k_{mpn} is less than 0.03. We also examined additional VCSELs at both wavelengths and observed similar results with kmpn never exceeding 0.062. Importantly, these low kmpn are consistent with our previous link experiments as well as with other published link results [103, 104].

We also calculated the kmpn for the 900nm VCSELs at the four biases previously described. Using the cross-correlations listed in Table 3.3 the k_{mpn} for the various methods and modes are listed in Table 3.5. In all cases kmpn is strictly less than 0.06.

Table 3.5: k_{mpn} for 900nm VCSEL at Various Bias

900nm VCSEL	Modes	k_{mpn} (TMC)	Mode	k_{mpn} (SMV)
3.5mA	*1,2*	0.042	1	0.045
	2,3	0.047	2	0.040
	-		3	0.034
5mA	*1,2*	0.044	1	0.037
	2,3	0.037	2	0.041
	-		3	0.029
8mA	*1,2*	0.050	1	0.022
	2,3	0.040	2	0.059
	-		3	0.047
10mA	*1,2*	0.038	1	0.031
	2,3	0.019	2	0.029
	3,4	0.024	3	0.017
	-	-	4	0.028

We also observe a noticeable decrease in kmpn when the fourth VCSEL mode lases at 10mA bias. This follows the decreased correlation already identified in Table 3.3. Again, these kmpn are much lower than the currently assumed worst case value used for standards efforts. The decreased kmpn associated with four lasing modes compared to 3 lasing modes may be expected to yield a performance improvement, however, it is likely that the extreme modes, 1 and 4 or 1 and 3 may dominate the MPN limited performance since these modes are most likely to be dispersed to the symbol edges first. However it is noted that the extreme mode pair 1, 4 is always weakly correlated. It is not clear if it is more beneficial to have fewer mode pairs with lower k_{mpn}, but experimentally it does not appear that one level of PAM-4 degrades faster as more fiber length is introduced. Therefore, the change in k_{mpn} between different biases of a VCSEL may not be significant.

3.1.3 RIN Measurement from Correlations

The directly measured variance and covariance allows us to calculate the effective RIN without making additional measurements or assumptions. Furthermore, the effective RIN can be determined in any link configuration, back to back or over varying lengths of fiber. The effective RIN is calculated directly from the measured covariance matrix elements using:

$$10^{\frac{RIN\,(dB/Hz)}{10}} \cdot \Delta f = \sum_{i=1}^{N} var_i + \sum \sum_{i \neq j} cov_{ij} \tag{3.7}$$

where $\text{var}_i = \langle a_i^2 \rangle - \langle a_i \rangle^2$ and $cov_{ij} = R_{ij}(\tau = 0)\sigma_i \sigma_j$. Note that since the variance and covariance are in terms of a_i and a_j, the average power term is unnecessary as the averaged instantaneous power sums to 1, e.g. $\sum_{i=1}^{M} \langle a_i \rangle = 1$.

A significant difference from standard RIN measurements is that the VCSEL noise statistics are added together by mode and mode pair rather than measured as an aggregate power. Thus, terms from the individual modes mixing in the receiver photodiode are not included; however, the VCSEL transverse modes are generally >150GHz apart and lose coherence with each other after a short distance (<5cm). Therefore neglecting these terms should have little impact on the RIN.

Use of a RIN parameter suggests the RIN is white noise or the effects can be captured as an effective white noise. The frequency dependence of the RIN can be computed from the COV matrix by the Fourier transforms of the auto-correlations and cross-correlations of the modes and mode pairs respectively, however it is desirable to retain the simplicity of the RIN parameter as is commonly used.

Since the cross-correlations are primarily anti-correlated, the covariance terms of Eq. (5) generally subtract from the sum of the individual variances and result in a lower RIN. In other words, the strength of the anti-correlations are significant factor for obtaining a low RIN and any disruption of this results in a larger RIN. Since the anti-correlation strengths decrease after fiber propagation the effective RIN will increase.

From the cross-correlations of the 850nm VCSEL through fiber and the standard deviations of the modes measured at the end of the fiber, we estimate that the effective RIN increases by 1dB/Hz for 100m of L-MMF and 3dB/Hz for R-MMF compared to the back to back case. Similarly, the cross-correlations for the 900nm VCSEL (Table 3.2) and the standard deviations of the modes measured at the end of the fiber, we estimate that the effective RIN increases by 1 dB/Hz for L-MMF and 2 dB/Hz for R-MMF compared to the back to back case. Due to the additional positive correlations for the 900nm VCSELs, the back to back RIN was higher than the 850nm VCSEL RIN. However, also due to the additional positive correlations, the RIN did not increase as much through fiber in the 900nm case, as the dispersive effects reduce the noise by decorrelating the positive correlations thus reducing their magnitude. The 850nm VCSEL through L-MMF still had a lower effective RIN than the 900nm VCSEL back to back, but all effective RINs were below -140dB/Hz. We conclude that in order to minimize RIN enhancement when using VCSELs with many anti-correlated modes, an L-MMF is best suited for the link. However, if the VCSEL has nearly equal positive and anti-correlations, the type of fiber does not affect the RIN significantly.

We confirmed these effects by directly measuring the effective RIN at the link end, Fig. 3.2(a), which shows the average effective RIN increases by 1dB/Hz for L-MMF and

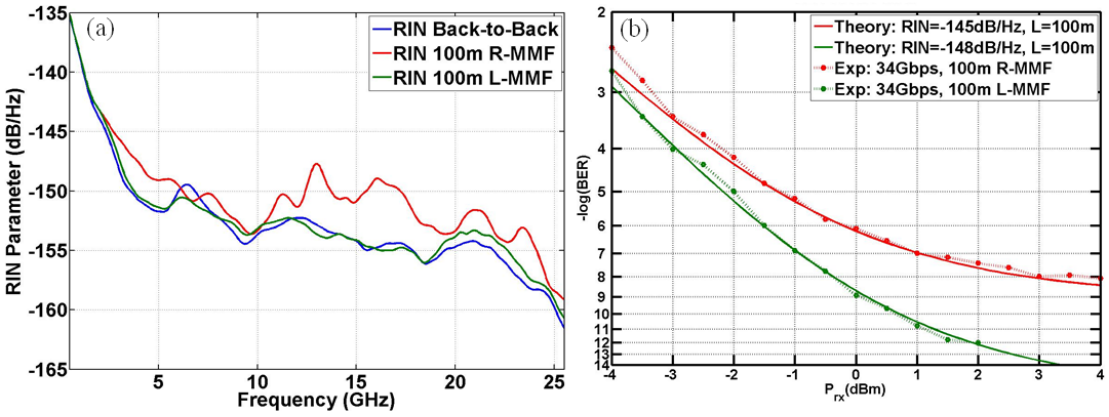

Fig. 3.2: (a) Measured RIN parameter of back-to-back vs. 100m R-MMF vs. 100m L-MMF; (b) 34Gbps OOK link BER analytic model vs. experiment.

5dB/Hz for R-MMF. Note that the RIN increase is predominantly observed at high frequencies. We experimentally quantified the impact on an OOK link using the two fibers at 34Gbps with 3.3 ER at 8mA bias using the 850nm VCSEL. We use our same end-to-end link model as used in section IV to calculate the MPN penalty. Using the known link parameters and $k_{mpn} = 0.03$, we demonstrate that an increased RIN parameter is required to match the theoretical results with experimental data, confirming the phenomenon of RIN enhancements due to fiber, Fig 3.2(b). Specifically, we observe an increase in RIN of 4 dB/Hz for the R-MMF and a 3 dB/Hz RIN difference between L- and R-MMF, resulting in a BER floor at 10^{-8} for R-MMF while L-MMF is able to support error-free communication. This increased RIN penalty of 3dB for R-MMF as compared to L-MMF is a substantial link penalty for high-speed VCSEL links.

3.2 Optimum VCSEL Apertures

The power efficiency, low cost, and high density capabilities of VCSEL-based transceivers make them a key component of short reach interconnects. The IEEE802.3bs standard focuses on 25GBd PAM-2 and PAM-4 MMF links requiring 16 and 8 fibers for 400Gbps links, respectively. Next generation links will most likely focus on fewer MMF

pair solutions by using wideband multimode fiber (WBMMF), short wavelength division multiplexing (SWDM), and faster line rates. In the case of PAM-4, these data rates were demonstrated with multiple aperture VCSELs. However, there was a difference in maximum error-free data rates between the VCSEL apertures that was not specific to mode partition noise (MPN), extinction ratio (ER), or VCSEL RMS spectral width [105]. Rather, the dispersion the VCSEL modes experience in the fiber differs between the VCSEL aperture sizes, and results in different noise enhancement effects.

In this section, we demonstrate through direct measurement of 850nm VCSELs with four different apertures, that i) the transverse mode correlations are stronger when fewer modes are present i.e. smaller apertures and ii) the mode correlations degrade more quickly due to dispersion when there are fewer modes. Thus the initial RIN is lower (better) for smaller aperture VCSELs but the observed RIN at a receiver is more sensitive to link dispersion for smaller apertures. This results in an optimum aperture size which depends on total link dispersion. We then show, through experiment, RIN degradation in 100Gbps error-free PAM-4 links and compare the noise enhancement effects of the different aperture VCSEL. These results demonstrate that VCSELs with a smaller aperture are more susceptible to RIN enhancement due to the stronger anti-correlations and fewer mode groups and that there is an optimum aperture size.

3.2.1 Experimental Setup

The VCSELs used in this study were 3rd generation high-speed VCSELs fabricated at Chalmers University. The 850nm VCSELs have aperture diameters of: 5, 7, 9, and 11μm. The VCSELs support 3 to 10 mode groups depending on aperture size, are biased with

similar current densities. Each achieves data rates of at least 60GBd PAM-2 over 100m WBMMF and 90Gbd PAM-4 over 100m WBMMF. The mode separation process, Fig. 1a, provides >15dB of isolation from adjacent transverse modes while still retaining the complete spectral content of each mode set. Details of the experiment are similar to reference 4. The setup is calibrated so back-to-back peak correlations coincide with τ=0. The measured spectral RMS of the VCSELs are 0.698nm, 0.763nm, 0.869nm, and 0.949nm for the 5μm, 7μm, 9μm, and 11μm VCSELs, respectively. The fiber for link tests was LaserWave FLEX WideBand Multimode Fiber [103]. This WBMMF provides more than 4.7MHz-km effective modal bandwidth (EMBc) over the 850nm to 940nm wavelength range. This specific fiber was optimized near 900nm wavelength, making it slightly left tilted at 850nm. The link loss was ~0.78dB including connectors. Here, the term left tilted refers to the slope of the differential mode delay (DMD), where high-order modes travel faster than low-order modes and the DMD reduces the effects of chromatic dispersion from the fiber.

3.2.2 Cross-Correlations

The cross-correlation coefficient of the intensity noise, $R_{ij}(\tau)$, is calculated using 400k synchronously captured noise samples from all mode pairs for each VCSEL and the normalized statistical expression:

$$R_{ij}(\tau) = \frac{\langle a_i(t)a_j(t+\tau)\rangle - \langle a_i\rangle\langle a_j\rangle}{\sigma_i\sigma_j} = \frac{cov_{ij}(\tau)}{\sigma_i\sigma_j} \tag{3.8}$$

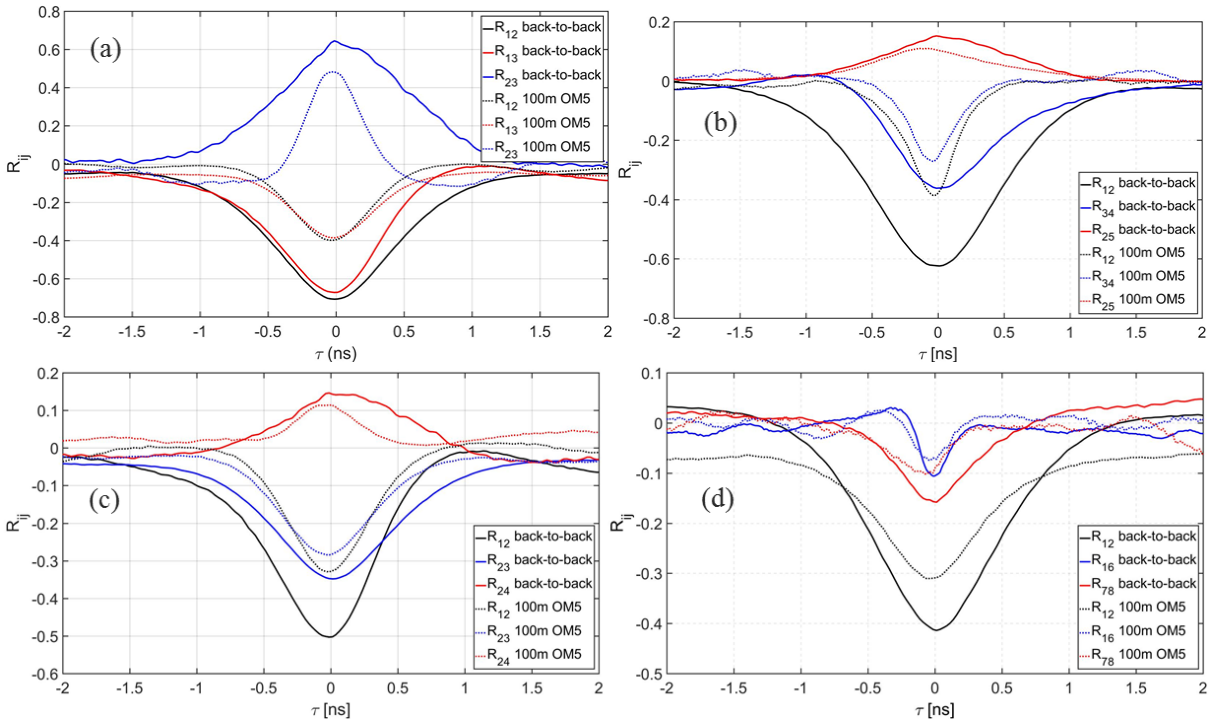

Fig. 3.3: (a) Correlations R_{12}, R_{23}, and R_{13} for the 5μm aperture VCSEL; (b) correlations R_{12}, R_{34}, and R_{25} for the 7μm aperture VCSEL; (c) correlations R_{12}, R_{23}, and R_{24} for the 9μm aperture VCSEL; (d) correlations R_{12}, R_{16}, and R_{78} for the 11μm aperture VCSEL.

Here, $a_i(t)$ and $a_j(t+\tau)$ represent the instantaneous power in the i^{th} and j^{th} mode and σ_i and σ_j are the standard deviations of the i^{th} and j^{th} mode. The correlations are determined

Table 3.6. Cross-correlations of 5μm and 7μm aperture VCSELs

Mode	1	2	3	4	5
1	-	-0.62	-0.35	-0.20	0.08
2	-0.71	-	-0.43	-0.24	0.15
3	-0.68	0.64	-	-0.36	-0.18
4	-	-	-	-	-0.23

Table 3.7. Cross-correlations of 9μm and 11μm aperture VCSELs

Mode	1	2	3	4	5	6	7	8	9	10
1	-	-0.42	-0.24	0.19	-0.27	-0.11	0.04	~0	~0	~0
2	-0.51	-	-0.34	0.20	-0.31	0.07	0.06	0.03	~0	~0
3	0.22	-0.35	-	-0.15	0.18	-0.28	-0.13	-0.08	-0.05	~0
4	-0.31	0.16	-0.28	-	-0.13	-0.24	0.06	-0.19	0.07	-0.07
5	-0.12	0.14	-0.17	-0.27	-	-0.29	-0.23	-0.17	0.16	0.10
6	-0.05	0.05	-0.19	-0.15	-0.21	-	-0.17	0.18	-0.14	-0.13
7	~0	~0	0.09	-0.20	-0.26	-0.25	-	-0.16	0.14	0.12
8	-	-	-	-	-	-	-	-	-0.29	-0.25
9	-	-	-	-	-	-	-	-	-	-0.25

for all mode pairs in both a back to back setup and after 100m of WBMMF. The number of supported modes vary between VCSEL apertures, where the 5μm VCSEL supports 3 mode groups and the 11μm VCSEL supports 10 mode groups. Note that in all VCSEL apertures, not every spectral peak signifies an independent mode. Some modes have multiple spectral peaks due to mode degeneracies. The 5μm aperture VCSEL has three mode correlations, where all modes exhibit strong correlations. The dominant lowest mode is anti-correlated with both higher modes which are positively correlated, Fig. 3.3a. The 7μm aperture VCSEL supports 6 modes, leading to more complex gain competition, several correlations are shown in Fig. 3.3b. As the VCSEL apertures increase to 9μm and 11μm, this trend continues as shown in Fig. 3.3c and 3.3d. The strength of the correlations generally decrease since there is gain competition among more modes and any two specific modes exhibit less correlation, Table 3.6 and 3.7. Furthermore, in the largest aperture VCSELs, the spatial overlap between the lowest and very highest mode groups are smaller making the mode groups essentially uncorrelated (correlations with ~0). Importantly, all VCSEL apertures support both anti-correlations and positive correlations, and the largest anti-correlations are between the first few modes. The larger anti correlations of the smaller aperture VCSELs contributes to the observation that the RIN is generally lower with smaller apertures. Lastly, we note that mode partition noise (MPN) is associated with anti-correlated modes and is therefore expected to be higher in the fewer mode, smaller aperture, VCSEL.

3.2.3 RIN Enhancement from Fiber

The net RIN is the sum of the variances plus a term that accounts for correlations (which are time dependent). We assume the RIN is white noise across the bandwidth:

$$10^{\frac{RIN\ (dB/Hz)}{10}} \cdot \Delta f = var_{RIN} = \sum_{i=1}^{N} var_i[W] + \sum\sum_{i \neq j} cov_{ij}[W] \quad (3.9)$$

$$\text{where, } var_i = \langle a_i^2 \rangle - \langle a_i \rangle^2 \text{ and, } cov_{ij} = R_{ij}\sigma_i\sigma_j \quad (3.10)$$

Here the a_i are normalized such that $\sum_{i=1}^{M}\langle a_i \rangle = 1$. From Fig. 3.3, we observe that the dispersive nature of the fiber significantly reduces the cross-correlations between the modes. In the case of the 5μm aperture VCSEL, Fig. 3.3a, the correlations are significantly reduced after 100m. Compared to the case of larger apertures 7μm, 9μm, and 11μm VCSEL, Fig. 3.3b, 3.3c, and 3.3d, the correlations decay slightly slower. This is most likely the result of the initially lower correlation and the different "mixing" effects the higher order modes experience when coupling to higher fiber modes. The result of this difference in loss of correlation is a difference in the susceptibility to RIN enhancement among

Table 3.8: Measured RIN and enhanced RIN for all VCSEL apertures

RIN (dB/Hz)	Distance	5μm	7μm	9μm	11μm
Variance and Covariance	back-to-back	-151	-151	-150	-147
	100m	-146	-148	-148	-145
Real-Time Scope	back-to-back	-153	-151	-149	-146
	100m	-148	-148	-147	-143

different VCSEL apertures. The correlations experience most of their reduction due to dispersion and not timing delay between the mode groups. The RIN was computed with both the variances and covariances of each mode and the aggregate signal, Table 3.6 and 3.7. The 5μm and 9μm aperture VCSELs had an initial (no fiber dispersion) RIN of -

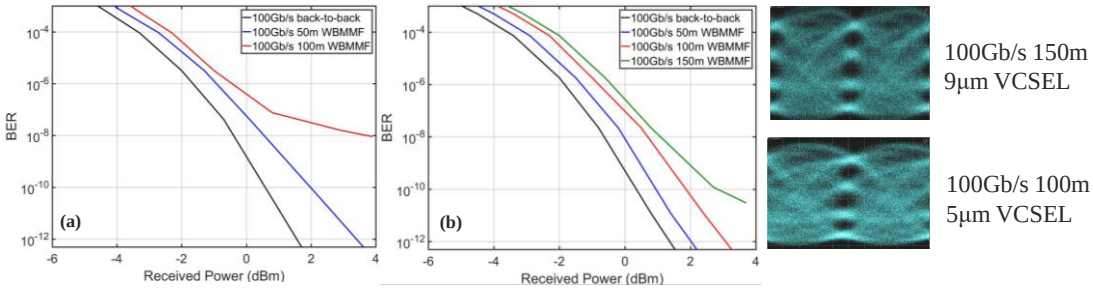

Fig. 3.4: (a) BER for 100Gbps RC PAM-4 using 5μm aperture VCSEL; (b) BER for 100Gbps RC PAM-4 using 9μm aperture VCSEL; (right) eye diagrams comparing 9μm and 5μm aperture VCSELs at 150m and 100m, respectively.

151dB/Hz and -150dB/Hz. All VCSELs experience an increased RIN after propagating thru fiber. The results of the computed aggregate RIN are confirmed by direct measurement of RIN using a high bandwidth real-time scope, Table 3.8. From our link BER experiments, we experimentally quantify the impact on a raised cosine (RC) PAM-4 signal at 100Gbps with setup similar to reference [105]. Consistent with Table 3.8, the 7μm VCSEL performs best. Figure 3.4 shows the BER and eye diagrams for the 5 and 9μm VCSELs. The 5μm aperture VCSEL degrades faster than the 9μm VCSEL with increased fiber length. The 5μm VCSEL does not reach 100m at 100Gbps PAM-4 error-free, Fig. 3.4a, while the 9μm aperture VCSEL reaches nearly 150m error-free, Fig 3.4b. This is consistent with the observed eyes of the 5μm VCSEL at 100m and the 9μm at 150m. More importantly, a noise floor develops much quicker in the smaller aperture VCSEL due to the dispersion effects on the heavily anti-correlated pairs and possibly due to MPN contribution. The 5μm VCSEL will experience a greater penalty due to MPN than the 9μm VCSEL, which will appear as a timing jitter and will not necessarily be accounted for in the variance measurements. Therefore, among this set of VCSELS the 7μm aperture is an optimum size for links beyond 50m.

CHAPTER 4.

VCSEL DATA COMMUNICATION

The 100GBASE-SR4 standard uses 25Gbps VCSELs to achieve 100Gbps using four MMF lanes. However, for the deployment of 200G and 400G systems, there is a need to increase the capacity of the system while controlling the density of the front panel interface and also the cost and complexity of the system. Employing 25Gbps core data rates for the 400GbE solution proposed by the IEEE P802.3bs Task Force requires using 16 fibers in each direction. At these data rates, it is difficult to scale to Terabit capacities. The historic and natural solution for retaining the low cost and low power consumption advantages of VCSEL-MMF links is enhancing the core data rates that each VCSEL source supports. However, data rate increases continue to out run bandwidth increases of VCSELs and receivers. Fortunately short reach links are beginning to exploit signal processing strategies to maintain the increasing data rates although available DSP is more limited that that used in long-haul systems due to power, cost and latency constraints.

In this Chapter, we will demonstrate the ability of VCSELs to scale data rate through VCSEL improvement and including signal processing strategies to mitigate channel impairments while shaping the spectral energy of the signal. Our first experiments investigate deployment of PAM-4 for 50Gbps. We then show that 100G transmission using a single 25G VCSEL can be achieved by employing RC pulse shaping and pre-emphasis at the transmitter in conjunction with post compensation at the receiver. We demonstrate greater than 100Gbps PAM-4 error-free signaling over 100m of OM5 MMF with new generations of VCSEL and photodiode technology. And, lastly we review different

modulation formats and determine the optimum format for a target bitrate, givem a specific channel bandwidth.

4.1 VCSEL Links >50Gbps: Experimental Studies and Demonstrations

VCSEL-MMF links with bitrates >50Gbps have been reported in the past using OOK modulation [106], but the capability to robustly support >50Gbps is limited. Advanced modulation formats like the multilevel modulation schemes that support multiple bits per symbol, offer a practical solution. In particular, PAM-4 has been demonstrated to support 32Gbps [107] using 850nm VCSELs. At the time of this research, reaches up to 200m at 30Gbps [101] and 50m at 50Gbps [102] were demonstrated at 850nm. Longer wavelength solutions using InGaAs VCSELs near 1micron had also been proposed. These VCSELs have their active layers strained, resulting in large differential gain and higher modulation bandwidths for these VCSELs. Advances in this technology have enabled 1060nm VCSEL-based MMF links with high reliability. One potential problem with links at longer wavelengths is the fiber DMD which would be high for the standard OM3 and OM4 fibers at wavelengths other than their optimal operation point, i.e., 850nm. To counter this issue, specialty fibers have been proposed which are designed for operation in broadband region, i.e., at wavelengths from 850nm to 1100nm, but more research is needed to determine the feasibility.

4.1.1 50Gbps PAM-4 links using 1060nm VCSELs

First attempts at 50Gbps links involved using strictly PAM-4. The ~25-Gbaud electrical PAM-4 signal is generated by power-combining two independent PRBS-7 channels (SHF 12124A), Fig. 4.1(a). Each channel has an independent 4-tap symbol spaced

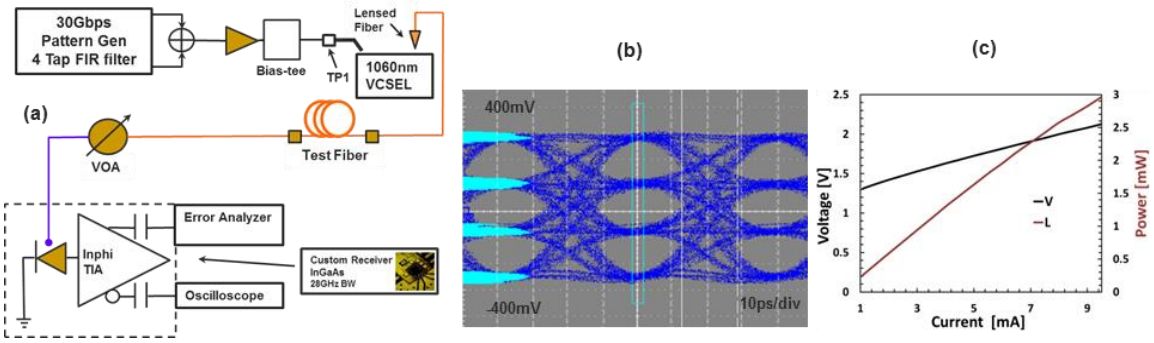

Fig. 4.1: (a) Block diagram of the experimental setup of PAM-4 link at 1060nm; (b) Eye diagram at TP1; (c) L-I-V curve of the VCSEL.

pre-emphasis filter. The resultant electrical signal exhibits a quality factor of ~9.5 when loaded with 50Ω impedance, Fig. 4.1(b). The receiver is custom designed at Georgia Tech consisting of an InGaAs photodiode and a low noise Inphi TIA yielding a net bandwidth of ~28GHz. The bit error ratio (BER) of the received PAM-4 signal is calculated using a conventional error analyzer (SHF 11100A). Three different threshold levels are used to measure the symbol error rates (SER) of the top, middle and the bottom eyes in the PAM-4 signal.

The BER can be calculated from the SER values, in high-SNR regime for the naturally coded PAM-4 signal [82]:

$$BER = \frac{1}{2}SER_{bot} + SER_{mid} + \frac{1}{2}SER_{top} \tag{4.1}$$

Our analytic model calculates the BER values directly from the noise variances such as receiver thermal noise, shot noise, RIN and MPN along with the eye-closure penalty which is impacted by all possible ISI effects in the link including the laser and receiver bandwidths, CD, DMD, baseline wander effects and finite ER of the transmitter. Our noise variances are equivalent to those of the IEEE 802.3bm link budget model [4]. ISI effects are determined assuming a Gaussian channel response to estimate the eye-closure penalty from the net channel response captured by the 10%-90% rise-time Tc. The worst-case eye-closure for each individual eye for PAM-4 is [108]:

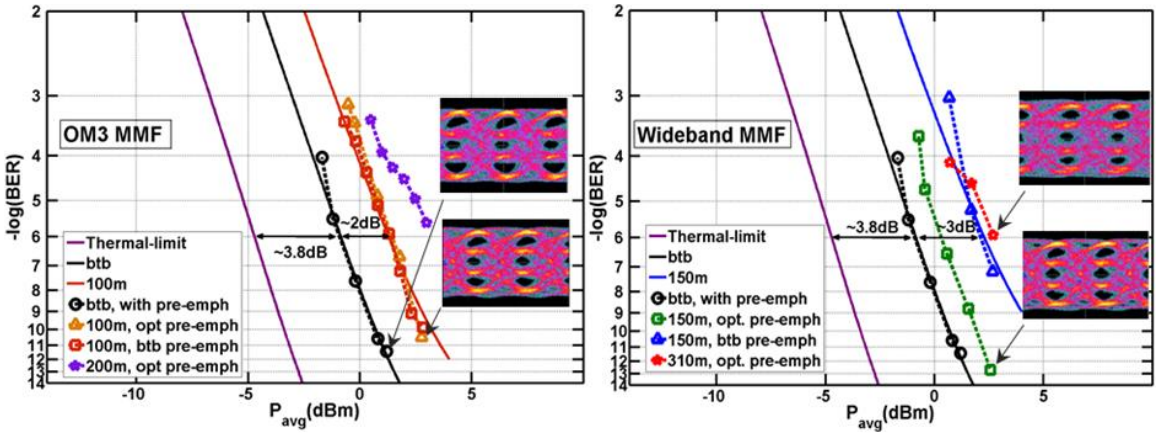

Fig. 4.2: 50Gbps using PAM-4 at 1060nm: (**left**) OM3 MMF performance: Analytic (solid lines): RIN ~-155dB/Hz, CD=40ps/nm.km, EMBc~2.4GHz.km and ISI penalty indicated. Experimental (dashed lines): 100m and 200m; (**right**) Prototype Wideband MMF performance: Analytic (solid lines): RIN ~ -155dB/Hz, CD=40ps/nm.km, EMBc~4GHz.km and ISI penalty indicated. Experimental data (dashed lines): 150m, 250m and 310m.

$$E_{m,PAM-4} = 2.85\exp\left(-1.28\left(\frac{T}{Tc}\right)^2\right) \tag{4.2}$$

where 'T' is the symbol period. Through best fitting of the analytic model results with the back-to-back (back to back) and fiber experimental data, power penalties due to individual ISI effects have been identified along with an accurate estimation of different noise parameters including RIN and MPN. The BER performance for back to back, 100m and 200m of OM3 fiber, using pre-emphasis optimized for each link, is shown in Fig. 4.2. Results for the 100m fiber link with the same pre-emphasis as the back to back case are also included for accurate estimation of CD/MD penalties from comparison with analytic model results. The PAM-4 full ER (top/bottom) was maintained at ~6dB with a baud rate of 25.78125Gbaud/s allowing for FEC overhead. This OM3 sample has its peak modal bandwidth between 900 and 950nm. The performance with 100m OM3 exhibits a 2dB fiber penalty when the same pre-emphasis as back to back was used. Estimations deduced from fitting our analytic model results to the experimental data for 100m fiber link yield ~2.4GHz.km for the EMBc of the OM3 fiber at 1060nm. Here, a CD parameter of ~40ps/nm.km has been used in the analytic model which is typical of 50 micron MMFs at

1060 nm. The corresponding ISI penalties due to CD and MD for this 100m fiber link are ~0.2dB and 1.5dB respectively. The 200m fiber data shows that a BER of < 10-5 can be achieved, which is limited only by the overall power available. Specifically, there is no evidence of a noise floor in these measurements, which suggests negligible MPN penalty in these links. Fig. 4.2 also shows the performance of a prototype wideband MMF designed for performance beyond ~980nm. DMD measurements with a tunable laser show that modal bandwidth increases from ~1.8GHz-km at 775nm to as high as ~4.2GHz-km at 1000nm for these fibers. The peak bandwidth beyond 1000nm has not yet been determined. The experimental data shows that error-free performance is possible for reach up to 150m fiber without FEC and 310m with FEC at an additional fiber penalty of ~3dB.

4.1.2 RIN Dependence on Bias for 50Gbps PAM-4 Links

RIN is primarily the result of spontaneous emission [109] and therefore generally decreases with increasing average laser power. The RIN penalty for a modulated VCSEL depends on the individual intensities of each possible amplitude. For PAM-2 links, a single RIN corresponding to the average output power may be a reasonable approximation as there are only two output power levels and the ER may be modest. The four distinct levels of PAM-4 together with the typical high ER associated however may result in significant variation of RIN with the power levels. Additionally, the reduced ER of the individual levels increases the BER sensitivity to RIN compared to OOK links and a small error in RIN estimation causes larger deviations in the predicted link performance even at reasonably high ER. The effect increases with increasing VCSEL RIN, and is significant for RIN >-140dB/Hz. The power spectral density (PSD) of the VCSEL RIN is measured when operating the VCSEL unmodulated at different DC-bias currents. The resultant

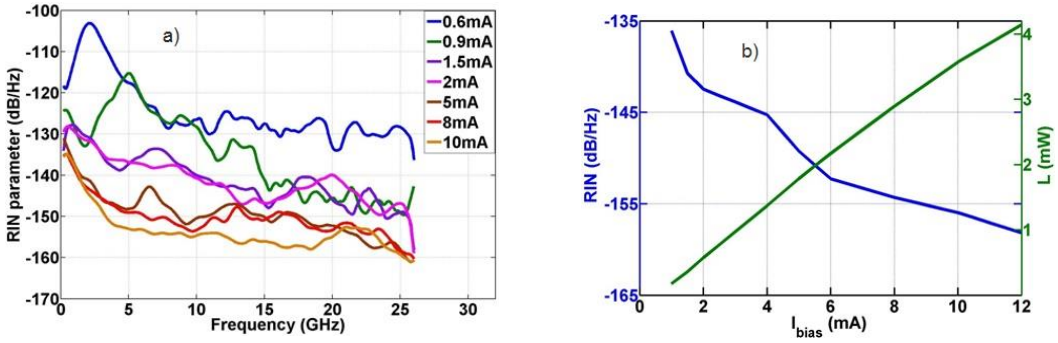

Fig. 4.3: (a) Unmodulated RIN spectra for various bias currents; (b) L-I-RIN for the 900nm VCSEL

spectra, Fig. 4.3, exhibit the expected peak resonance frequency shifts towards higher frequencies and increased damping with increasing bias, Fig 4.3.

We compute the average RIN at each bias and use these results in our analytic model. These VCSELs exhibit a very good average RIN less than -150dB/Hz for bias larger than 5mA. Error-free performance of 25.78GBaud PAM-4 using 900nm VCSELs at a full (highest to lowest level) ER of ~5.4dB, is readily achievable, Fig. 3.6, in the back to back configuration. We fit the measured data using both a fixed average RIN of -153.8dB/Hz corresponding to the average bias point (7.5mA) and an intensity dependent RIN of [-143.4, -150, -153.6 and <-155] dB/Hz for the 0, 1, 2 and 3 levels respectively.

The receiver sensitivity is fixed; therefore the only fitting parameter is the net ISI penalty. The variable RIN model yields notably better fits to the measured data than the fixed RIN model, Fig. 4.4. Importantly, the ISI primarily determines the behavior at high BER and a combination of ISI and RIN determines the behavior at low BER. The extracted ISI is ~5.3dB (5.5dB) for the variable RIN and fixed RIN model respectively. Importantly, the apparent ISI penalty decreases by ~0.2dB when using a variable RIN; thus the fixed RIN modeling overestimates the fiber ISI penalty. Furthermore, these deviations in the RIN penalty will be much larger for VCSELs with higher RIN. For example, our model predicts

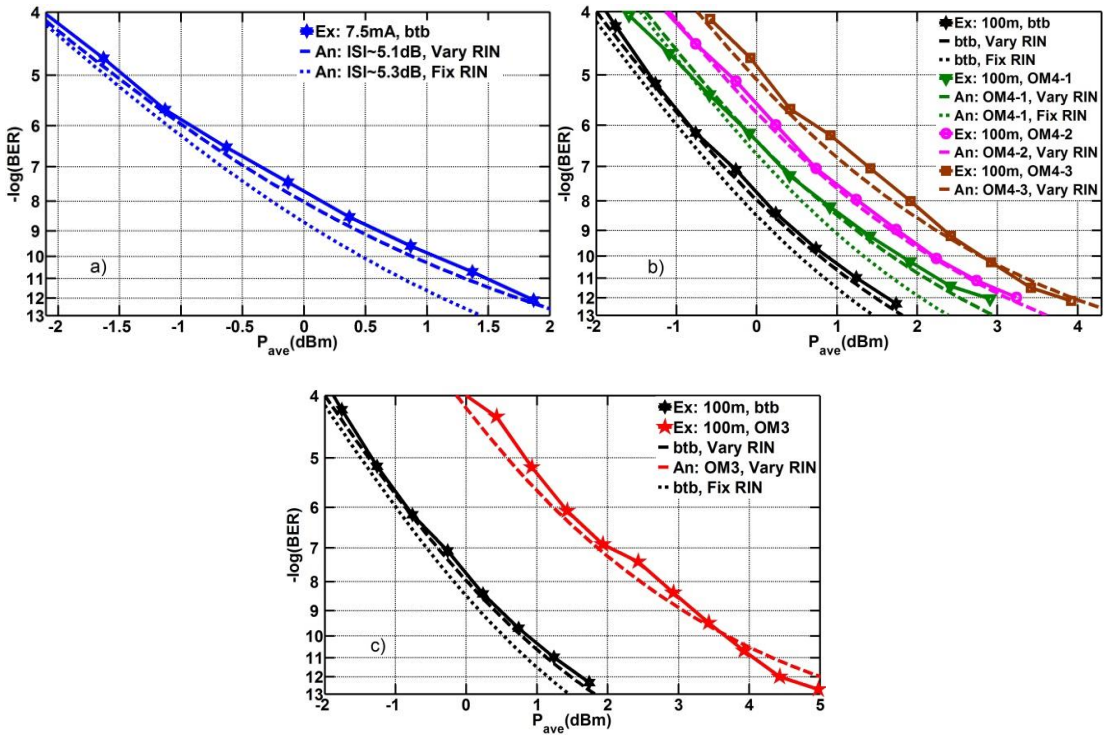

Fig. 4.4: 50Gbps PAM-4 for (top left) back to back at 7.5mA bias; (top right) 100m of three standard OM4 fibers at 8.5mA. (bottom) 100m of one standard OM3 fiber at 8.5mA. Ex: experimental, An: analytic model. Variable RIN yields improved fit to experiment.

deviations of up to 2dB if the average RIN of the VCSEL is >-145dB/Hz for an ER of ~6dB. Error-free transmission over 100m of three standard OM4 fibers and an OM3 fiber is also readily achieved, Fig. 4.4. Here, a bias of 8.5mA and a full ER of ~6dB was used. The EMBc of the three OM4 fibers are ~10.0GHz-km (OM4-1), ~6GHz-km (OM4-2) and ~5.2GHz-km (OM4-3) with slightly different optimum wavelengths near 850nm.

We use the same individual RIN values as for the back to back case and achieve a very good fit when using an appropriate ISI penalty. On the other hand when using the singe valued RIN the model deviates from the observed BER performance. Note that the model predicts the MPN parameter k to be < 0.1 indicating negligible MPN in all the links.

4.2 DSP-Enabled 100Gbps PAM-4 VCSEL Links

Data centers (DCs) are the “processing unit” of the internet, providing both storage and computational resources to all users. Maintaining and increasing these services requires power efficient optical links ranging from a few meters to ~2km with the number of connections scaling inversely with reach. Thus, the short reach interconnects within DCs are highly constrained to be low cost as highly power efficient, while supporting increasing data rates. Vertical cavity surface emitting laser (VCSEL) sources using multimode fiber (MMF) and direct photodetection have consistently provided advantages in short reach links since these links offer excellent performance, low cost and high density and are power efficient.

In this section, we explore the challenges and benefits of signal processing with currently available optical technologies and demonstrate a path to deploying 100Gbps VCSEL links [2] using a single VCSEL source over >100m of MMF while employing direct detection. We achieve higher data rates by increasing the baud rate as well as by employing higher modulation formats [3] both enabled by signal processing that can be implemented in current SiCMOS technologies [4]. We demonstrate the benefits of near Nyquist spectral occupancy and the decoding strategies required when employing these pulse shapes. We show that 100G transmission using a single 25G VCSEL can be achieved by employing the spectrally efficient RC pulse shaping and pre-emphasis at the transmitter in conjunction with the widely employed Oerder-Meyr timing recovery and post compensation using 7 FFE and 3 DFE taps at the receiver. We investigate the performance advantages of pulse shaping in band limited links including a comparison of ISI penalties for RC pulses and unshaped signals. We include calculations for noise enhancement due to receiver equalization and transmitter pre-emphasis for both shaped and unshaped signals

enabling a full assessment of PAM-4 signaling in bandwidth constrained VCSEL/MMF links. We also demonstrate 107Gbps PAM-4 signaling at 850nm and 940nm through 105m of OM5 MMF.

4.2.1 Pulse Shaping and Equalizer Noise Enhancement

Bandwidth limitations from components and fiber are a primary roadblock to achieving higher baud rates. One way to overcome this limitation is to limit the bandwidth by employing pulse shaping. However, pulse shaping comes at a cost of increased processing requirements, especially with advanced multilevel formats. Alternatively, one can use equalization to mitigate the ISI penalty. However, equalization introduces noise enhancement and an additional power penalty. Thus, it is important to optimize the trade-offs between pulse shaping, modulation format and equalization. We must first compute the penalties associated with these impairments [110, 111] with the goal to obtain a limit on the achievable performance, when using available VCSELs, fibers and receivers.

We start with the measured combined optical transmitter, fiber and optical receiver response, $H_c(f)$. The MMF link, which is dominated by the VCSEL response, is shown to be closely approximated by a third order Gaussian behavior, where the frequency response of an mth order Gaussian is $\exp\left((f/f_o)^{2m}\right)$. The steep roll-off after 20GHz implies significant challenges for equalization and motivates the use of a pulse shaping technique with a tighter roll-off than those conventionally used in MMF links. Hence, we investigate the use of raised cosine (RC) pulse shaping. We employ RC pulse shaping, where the frequency response $H_p(f)$ of the RC filter has the conventional form:

$$H_p(f) = \begin{cases} T, & |f| \le \frac{1-\beta}{2T} \\ \frac{T}{2}\left[1 + \cos\left(\frac{\pi T}{\beta}\left[|f| - \frac{1-\beta}{2T}\right]\right)\right], & \frac{1-\beta}{2T} < |f| \le \frac{1+\beta}{2T} \\ 0, & otherwise \end{cases} \quad (4.3)$$

Revisiting section 2.5.2, in Eq. (4.3), T is the symbol period, while β is the roll-off factor. The ISI penalty is data rate dependent and is the ratio of the eye height without ISI to that with ISI. It represents the extent to which the signal power would have to be increased in order to compensate for the reduced noise margin, arising from an ISI induced closing of the eye. The ISI penalty is [83]:

$$P_{ISI} = 10\log\left(\frac{1}{1-E_m}\right) \quad (4.4)$$

Details of the ISI implications and derivation can be found in section 2.5.2.

We also must consider equalization and the noise it enhances in the system. Pre-emphasis and post-equalization jointly compensate for the channel response for frequencies up to some BWEQ due to hardware or SNR limitations, i.e. we compensate such that $H_{E,Tx}H_{E,Rx} = \frac{1}{H_c}$ for frequencies up to BWEQ.

Figure 4.5 depicts the elements of our link and identifies the various noise processes. The optical power penalty due to noise enhancement is the ratio of the noise power before and after receiver post-equalization [83]:

$$Penalty_{noise} = 5\log\left(\frac{\int_0^{BW_{EQ}} N_2|H_r|^2\left|H_{E,Rx}\right|^2 df + \int_{BW_{EQ}}^{\infty} N_2|H_r)|^2 df}{\int_0^{\infty} N_1|H_r|^2 df}\right) \quad (4.5)$$

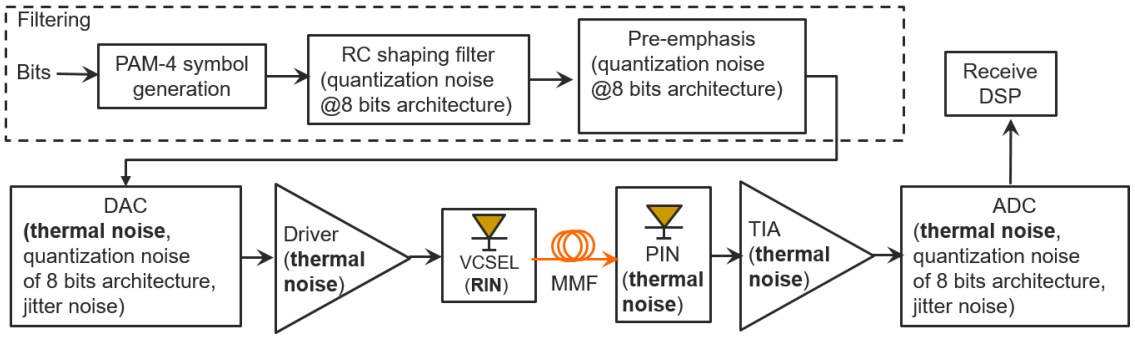

Fig. 4.5: Block diagram of the VCSEL -MMF link investigated. Noise sources are identified at each element with the dominant noise source in bold.

where,

$$N_1 = N_{thermal} + N_{RIN} + N_{ADC} + N_{DAC} \tag{4.6}$$

$$N_2 = N_{thermal} + N_{RIN} + N_{ADC} + \widetilde{N}_{DAC} \tag{4.7}$$

where N_{RIN} and N_{DAC} are Power Spectral Densities (PSDs) of the RIN and DAC quantization noise added at the transmitter, N_{ADC} is the PSD of the ADC quantization noise added at the receiver, while $N_{thermal}$ accounts for the all the thermal noise added by the link shown in Fig. 4.5. It should be noted that $\widetilde{N}_{DAC}$ is the PSD of the DAC quantization noise after pre-emphasis. In our theoretical analysis, the digital receive filter is presumed to have the same bandwidth limitation as the equalizer, i.e. BWEQ, and an ideal low-pass filter shape. Hence the second term in the numerator of Eq. (4.5) is negligible. More details on the noise enhancement can be found in section 2.5.3.

We revisit the power penalty due to ISI and sensitivity degradation in our link at various bit rates for the cases of the measured channel and RC pulse shaping without equalization are shown in Fig. 4.6 (same as Fig. 2.10). Results are shown for the case of

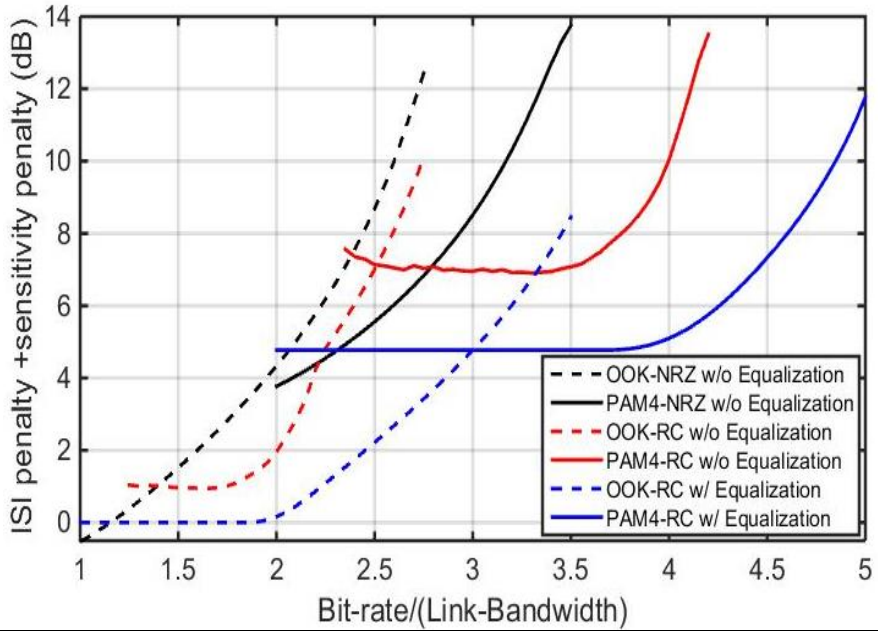

Fig. 4.6: ISI penalty for various modulation formats and transmit pulse shaping.

PAM-2 and PAM-4 modulations. Finally, in Fig. 4.6, we also show the power penalty owing to ISI and sensitivity degradation for the case of RC pulse shaping with equalization. It can be seen that employing PAM-4 rather than PAM-2 is justified for bit rates greater than three times the channel bandwidth, when employing RC pulse shaping and equalization. It can be seen from Fig. 4.6 that employing RC pulse shaping and PAM-4 modulation is justified for our 107Gbps equalized optical link, because the bitrate/(link-bandwidth) ratio is 107Gbps/28GHz=3.8. We emphasize that the results in Fig. 4.6 depend on the following system parameters:

1. These results were computed using the experimentally measured channel response of the optical link and hence the cross over points change if the channel were different. A Gaussian channel rolls off much slower than the measured channel equivalent 3dB bandwidth will exhibit a higher crossover point.

2. The results in Fig. 2 are dependent on the equalization bandwidth BW_{EQ}.

3. Finally, the cross over points are also dependent on the implementation penalties, which are typically higher for PAM-4 than for PAM-2. For example, brick wall filters are not realizable and we have neglected VCSEL nonlinearities. For our channel at 107Gbps (i.e. bitrate/(link-bandwidth)=3.8) our experiments resulted in a closed eye for PAM-2-RC modulation, while the eye was open for PAM-4-RC. We also obtained a closed eye for PAM-4-unshaped modulation.

The results shown in Fig. 4.6 assume ideal sampling at the center of the eye. Typically, the advantage of a lower ISI with RC pulse shaping comes at the cost of having

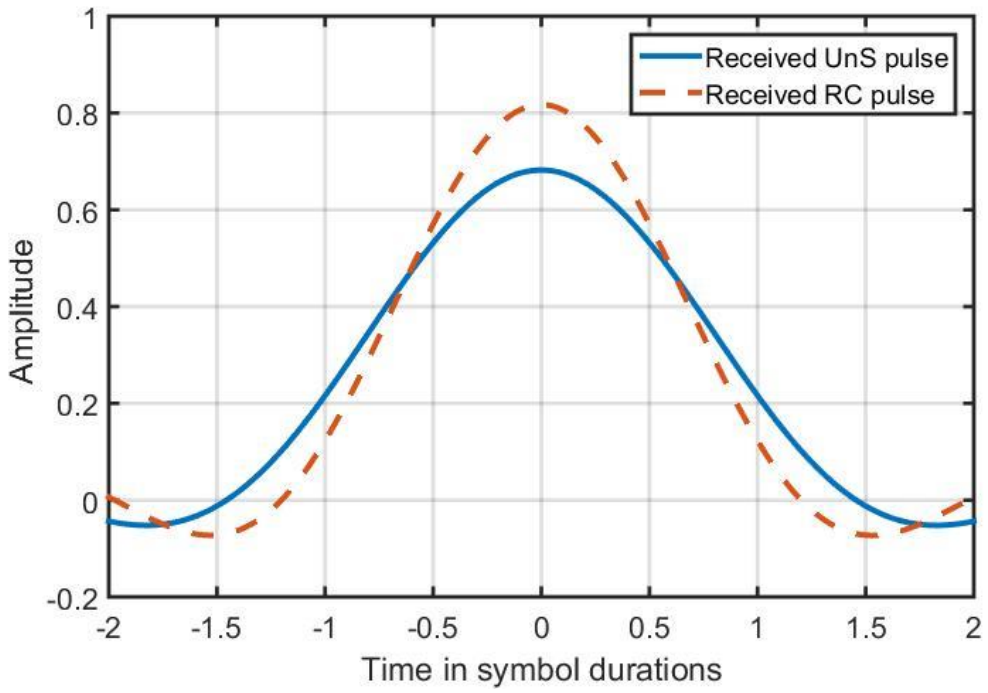

Fig. 4.7: Received pulse shapes at bitrate/(link-bandwidth) = 4.

to employ more sophisticated timing recovery algorithms, because the width of the eye for raised cosine pulse shaping is narrower than that for unshaped waveforms.

When the link is significantly bandwidth constrained, unshaped pulses suffer greater ISI then RC pulses due to their higher spectral occupancy. Hence, unshaped pulses lose the advantage of an initially wider pulse. Fig. 4.7 shows an isolated received pulse (simulated) for unshaped and RC pulse shaping in an equalized channel, when the bitrate is 4 times the bandwidth. It can be seen from Fig. 4.7 that the drop in pulse amplitude due to the bandlimited channel is comparable for the case of unshaped pulses and for RC pulse shaping, thereby resulting in an eye having a similar width. The width of the eye for the case of unshaped pulses is significantly reduced at this higher bitrate, because the bandlimited nature of the link severely distorts the pulses and the received pulses are no

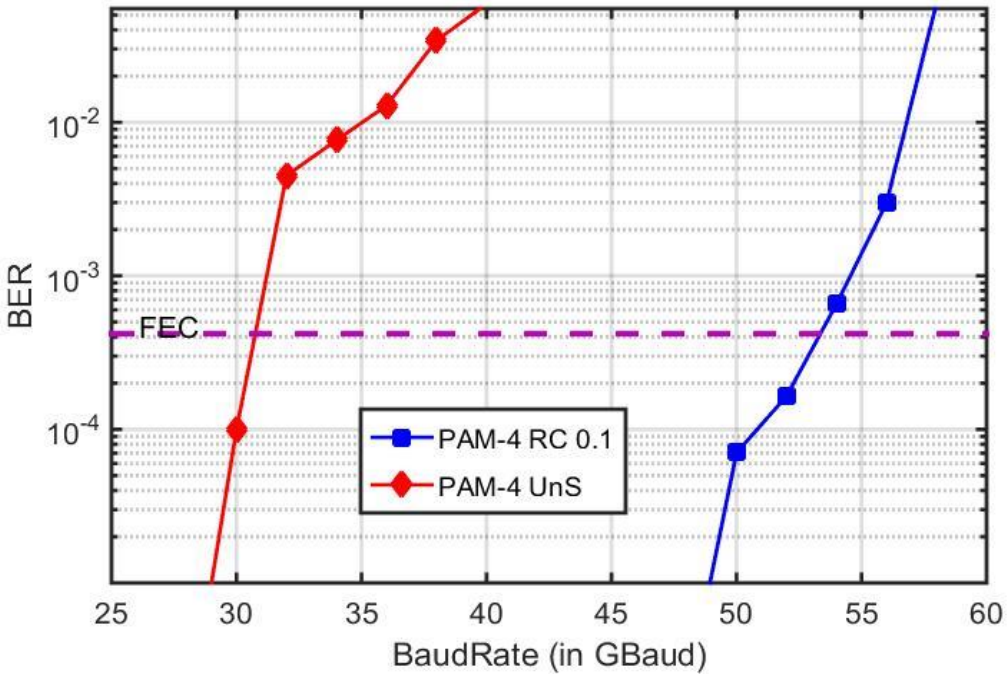

Fig. 4.8: Experimental PAM-4 BER for UnS and RC 0.1 pulse shapes with the same V_{pp} swing (0.7V) and optical power (1.5dBm).

longer rectangular shaped, as can be seen from Fig. 4.7. Hence a migration to RC pulse shaping is justified.

We experimentally compare unshaped to a RC pulse shape with roll off factor of 0.1, Fig. 4.8. Using the same voltage swing and maintaining the same output power, we are able to directly assess the performance degradation of a RC pulse shape. Ideally, the RC pulse shape with a roll-off factor of 0.1 should extend the baud rate from 30GBaud unshaped pulses to ~54Gbaud 0.1 RC without any performance degradation [111]. As expected, we experimentally measure minimal BER degradation when moving to RC. Thus, we can conclude that the implementation penalty of RC compared to unshaped pulses is nearly the same and that the sample jitter in RC is negligible.

4.2.2 Experimental Setup

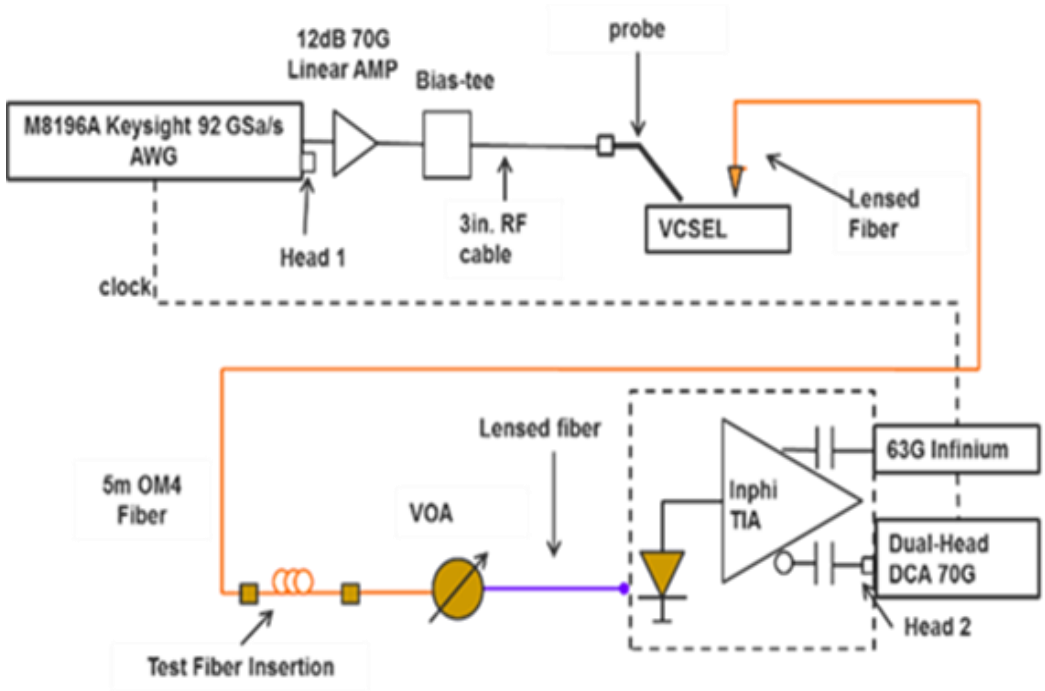

Fig. 4.9: Experimental Setup for PAM-4 link.

As shown in Fig. 4.9, the experimental setup we employed included the electrical transmitter, optical transmitter, the optical channel, optical receiver and finally the offline electrical receiver.

4.2.3 Electrical Transmitter

The 107Gbps electrical PAM-4 signal was generated using the Keysight M8196A Arbitrary Waveform Generator (AWG) having 32 GHZ of bandwidth. Unlike the conventional rectangular pulse shape of unshaped (UnS) signaling, we employ the spectrally efficient raised cosine (RC) pulse shape.

In our experiments, we used roll-off factor of 0.1 for the back-to-back (BTB) and with fiber scenarios. As seen from the employed data rate, an overhead of 7 percent was considered in order to account for the deployment of a low latency Reed-Solomon FEC [10]. The FEC technique we employed had an uncorrected bit error rate (BER) threshold of 4.2×10^{-4} in order to achieve a post FEC BER $< 1 \times 10^{-12}$. In addition to generating the electrical signal the AWG also performed the DSP technique of pre-emphasis. This involved the AWG relying on a calibration software for measuring the overall channel response from the AWG to the optical receiver, where this channel response was then partially compensated by the AWG. The adaptive filter at the receiver post-compensated for the residual channel response. The joint compensation of the channel response through pre-emphases and post compensation was primarily gain boosting of less than 10dB at the

Nyquist frequency and they can be implemented using low-complexity, low-cost analog FIR and IIR filters. Fig. 4.10 demonstrates how pre-emphasis helps overcome channel distortions and hence opens the eye, the filter shape is described in Section IV of this paper (Fig. 11).

There are multiple chipsets currently available for 28Gbaud PAM-4 from Inphi and Avago with the experimental setup, Fig. 4.9, similar to that of the Inphi architecture [112]. These products are full transceivers with PAM-4 mapping and a pre-emphasis FIR filter at the Tx while having a continuous time filter, ADC and equalizer at the Rx. These chipsets support 56Gbps PAM-4 sufficient for the overhead of FEC. In order to achieve 56Gbaud PAM-4 with pulse shaping, a doubling in throughput and an additional filter for RC pulse

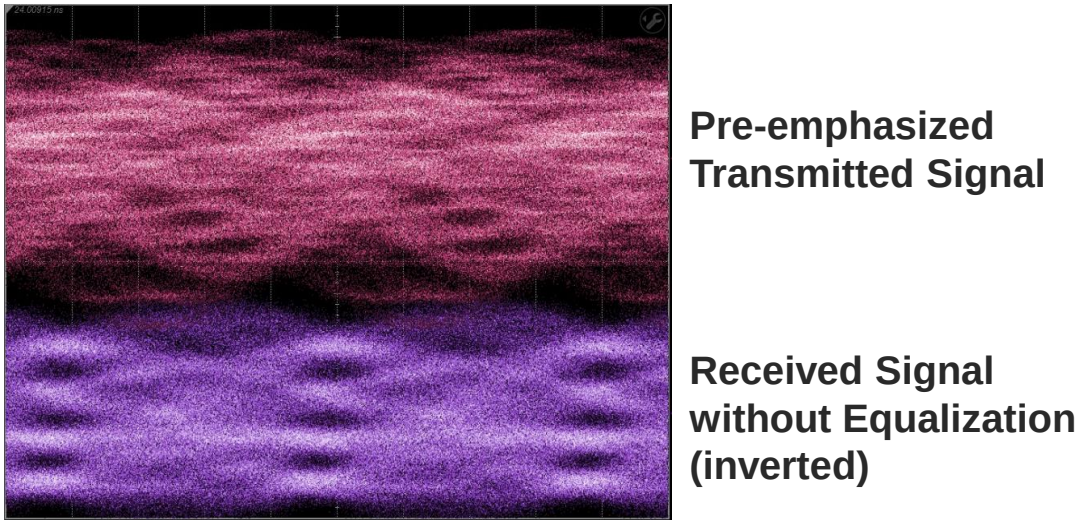

Fig. 4.10: Transmitted distorted signal captured with sampling scope and optical received eye (inverted) at 107 Gbps after 105m OM4 fiber.

shaping are required. However, the general architecture is unchanged and therefore the complexity and cost to move to 100Gbps would not be significant. Designing an analog FIR filter to implement RC pulse shaping is not a sophisticated task. Due to the symmetry as well as regular zero crossings of RC pulses, only 6-7 non-zero unique tap weights are

needed to create an effective T/2 spaced filter, and this filter would have better performance than the DAC used in the experiment. Generally, it is preferable to deploy the most efficient link possible for a given application. And, some applications will benefit from maintaining the native 100G data systems using analog PAM-2. However, historically higher data rates per laser source always become dominant technology. As an estimate on availability, the bandwidth of PAM-4 electronics has increased from approximately 10Gbps in 2010 to 56Gbps in 2015. Thus PAM-4 chipsets with sufficient through-put should be available in commercial chipsets in the next few years and as SiCMOS chipsets become available for PAM-4 over a wide range of media, costs will not be a significant issue.

4.2.4 Optical Transmitter

The optical transmitter converted the electrical signal to an optical signal. As seen in Fig. 4.9, the electrical signal after pre-emphasis was amplified using a 70GHz linear SHF 827 amplifier. The amplified signal was then employed in directly modulating an unpackaged VCSEL via a 3in cable, 40GHz bias-tee, and 40GHz probe. The VCSELs were biased in the near-linear region of its L-I-V transfer characteristic. The amplification of the modulating signal allowed the AWG to spend most of its resources on pre-emphasis rather than on generating a high power output signal. The VCSELs used in our experiment were commercially designed for 25Gbps operation. Additionally, they had a RIN of ~-142dB/Hz [11, 12]. Two important impairments imposed by the VCSELs include the nonlinear nature of its electrical to optical conversion as well as its limited modulation bandwidth. The optical power levels for PAM 4 modulation were optimized for minimizing this nonlinearity. Employing pre-emphasis and post-compensation helped relax the bandwidth constrained imposed by these VCSELs. Finally, the employment of spectrally efficient

raised cosine pulse shaping in the electrical transmitter helped achieve maximum data rate for the available bandwidth. The VCSELs were biased at 13.5 mA (for 850nm) and 14.4mA (for 940nm), yielding RMS spectral widths of ~0.49nm and ~0.54nm at 850nm and 940nm, respectively. Both VCSELs yielded >3dBm fiber coupled power with no thermoelectric cooler.

4.2.5 Fiber and Optical Receiver

In this study we first employed 105m of OM4 fiber from OFS in conjunction with an 850nm Finisar VCSEL and then employed 105m of OM5 fiber from OFS in conjunction with both 850nm and 940nm Finisar VCSELs. The major impairments imposed by the fiber include modal dispersion and chromatic dispersion [113]. Additionally, dispersion in the fiber results in the generation of mode partition noise (MPN) and enhancement of RIN [113]. The effective modal bandwidths (EMBc) of the OM4 fiber and OM5 were 6GHz-km and ≥5GHz-km, respectively [103]. The optical receiver consisted of an Enablence p-i-n photodiode followed by a low noise Inphi Trans Impedance Amplifier (TIA) having bandwidth >43GHz. The photodiode had a responsivity of 0.3 and 0.33 at 850 and 940nm with coupling. The twin outputs of the TIA were captured by both a sampling scope (DCA 81600D), and a real-time scope (DSA-X 96204Q). The bandwidth of the entire BTB optical link was measured to be ~21GHz with the 850nm VCSEL and ~22GHz with the 940nm VCSEL. The bandwidth dropped to ~20GHz at 850nm when 105m of fiber was employed. The overall bandwidth of the optical receiver was 28GHz and the thermal noise added was 2.1mV RMS. The sampling scope was used to observe the received eyes prior to offline DSP, while the real-time scope recorded the waveform for offline equalization.

4.2.6 Electrical Receiver

The real-time scope sampled the received signal at 160GSa/s. The waveform was saved and employed as the input for the offline electrical receiver, where this receiver performed offline equalization and demodulation. Fig. 4.11 shows the various offline DSP steps. The use of RC pulse shaping for spectral efficiency, instead of the conventional rectangular pulses, necessitates the use of an advanced timing recovery scheme, namely the Oerder-Meyr algorithm [114]. This compensates for fractional baud rate errors that rise from imperfect clocks in the digital-to-analog and analog-to-digital converters. As shown in Fig. 9, the signal was resampled and then low-pass filtered for SNR maximization

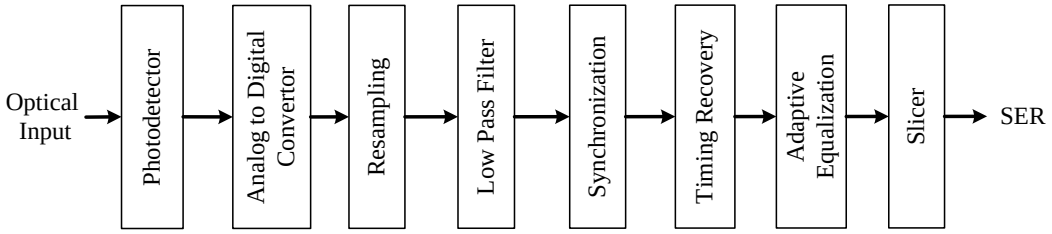

Fig. 4.11: Receiver Architecture

through suppression of out-of-band noise. The ISI imposed by the residual channel response after pre-emphasis is overcome using equalization. Static equalization techniques can optimize the link for a specific application, while reducing its adaptability to multiple or dynamic link conditions. Hence, we choose to employ adaptive equalization techniques relying on a training sequence. Identification of the start of the training sequence (synchronization) within the output of the receive filter is achieved through a cross-correlation test between the transmitted training sequence and the received signal waveform, as shown in Fig. 4.11. The equalization algorithm itself relies on the availability on one sample per symbol. Hence, the synchronized received signal is then down-sampled

to one sample per symbol. After an extensive study of various methods, we zeroed in on a digital feedback equalizer (DFE) filter having 3 backward taps and 7 forward taps, because it struck the optimum tradeoff between implementation complexity and BER performance. The DFE filter coefficients are adaptively determined using the Least-Mean-Square (LMS) algorithm with a step size of 0.0004. As shown in Fig. 4.11, the equalized output is then passed through a slicer for calculation of symbol error rate. The use of gray coding ensures that the BER of the signal is approximately 0.5 times the symbol error rate.

4.2.7 Experimental Results

We first evaluated the system performance at 850nm for 105m of both standard OM4 fiber and WBF. These fibers had an over-compensated alpha profile, which reduces the group delay of the higher order fiber modes compared to the lower order fiber modes at a single wavelength. The higher order VCSEL modes having higher wavelengths couple into higher order fiber modes having a lower group delay. Thus, modal dispersion compensates chromatic dispersion (CD), thereby reducing the effect of fiber-enhanced RIN

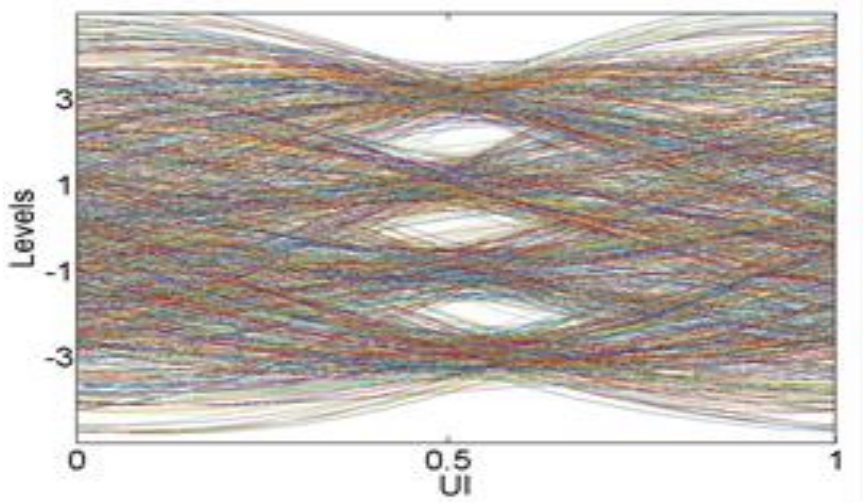

Fig. 4.12: Received unequalized eye at 850nm through 105m of OM4.

and MPN [113]. Fig. 4.12 shows the received eye prior to equalization where a minor eye skew of ~0.05 UI can be seen, where this skew can be attributed to VCSEL nonlinearities. While this skew can be mitigated through additional signal processing, we avoided correcting it because the penalty was negligible enough to ensure that the BER was below the required threshold value. Fig. 4.13 shows the spectrum of equalization filters in the case

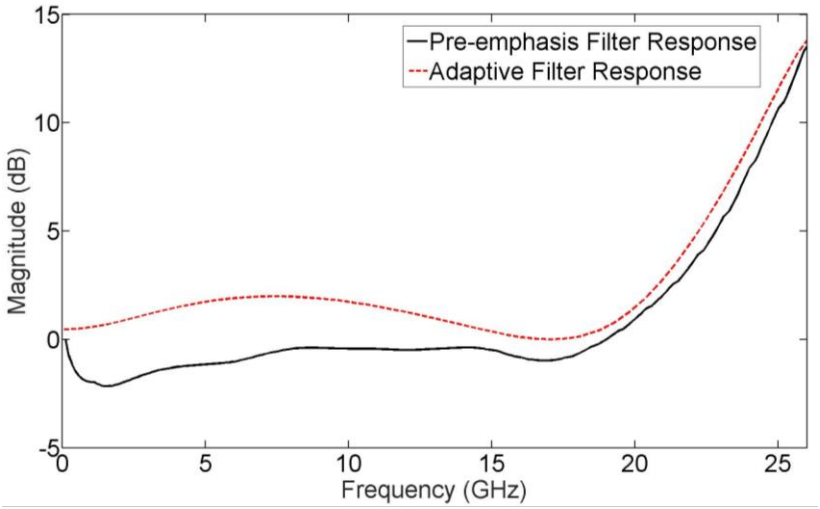

Fig. 4.13: Frequency response of the pre-emphasis filter in the transmitter and adaptive equalizer filter in the receiver.

of 105m of OM4 fiber and an 850nm VCSEL. The Keysight AWG implements pre-emphasis of the signal to compensate for the estimated channel response evaluated by the AWG calibration software. The adaptive filter at the receiver compensates the remaining channel distortions. In this case, the AWG and adaptive filter provide similar compensation, and thus can each be implemented with digital or analog filters of similar complexity.

Fig. 4.14 compares the BER of three scenarios for the 850nm VCSEL, namely the BTB scenario, 100m OM4 fiber scenario, and 100m wideband fiber scenario. It can be seen from Fig. 4.14 that the FEC limit was readily achieved in all cases. The steep roll-off of

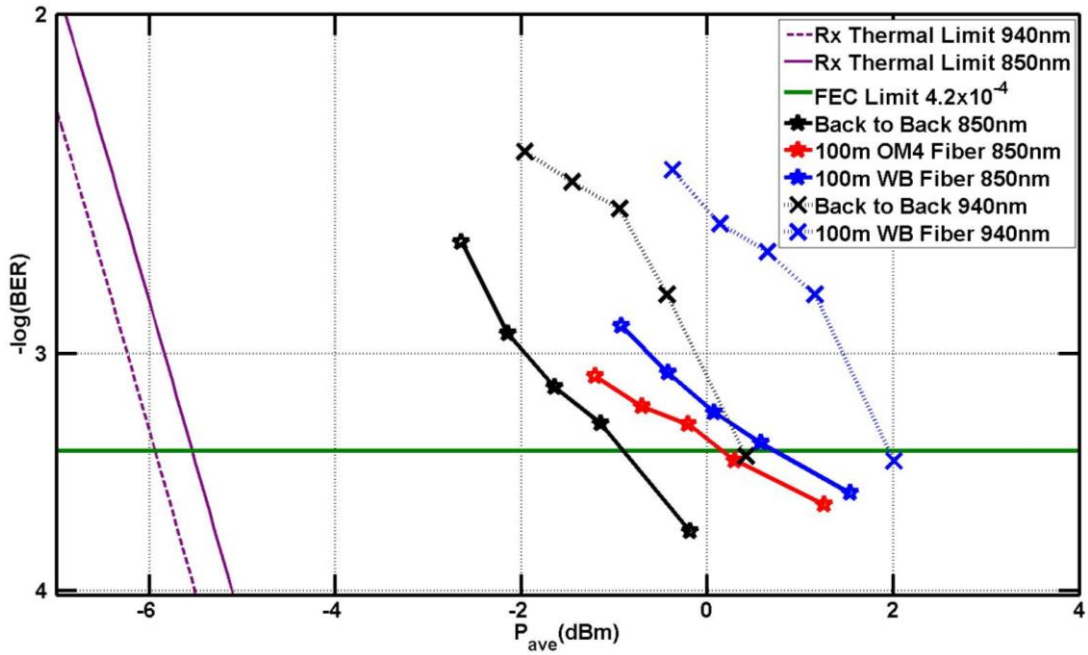

Fig. 4.14: 100Gbps PAM-4 BER performance at 850 nm and 940nm.

the link's bandwidth and saturation of the TIA made pre-emphasis for compensation of the channel response challenging. An additional 2.5dB attenuation was required for adequate compensation. However, comparing the BER performances of the BTB and fiber scenarios in Fig. 4.14, it can be said that there remains an uncompensated residual ISI penalty of approximately 1.3dB. It can be stated from Fig. 4.14 that within the margins of experimental error both OM4 and WBF provide similar performance, where this provides motivation for a migration from OM4 to WB, which can support higher frequencies in addition to 850nm. Thus, we then compared the system performance at 850nm and 940nm, when using WBF.

Fig. 4.15 compares the eye diagrams at 850nm and 940nm, when employing WBF. It can be seen from Fig. 4.15 that unlike at 850nm, the eye skew is much less pronounced at 940nm, despite using similar voltage swings. This may be attributed to damping differences between the VCSEL cavities. Fig. 4.14 also shows the BER performance at

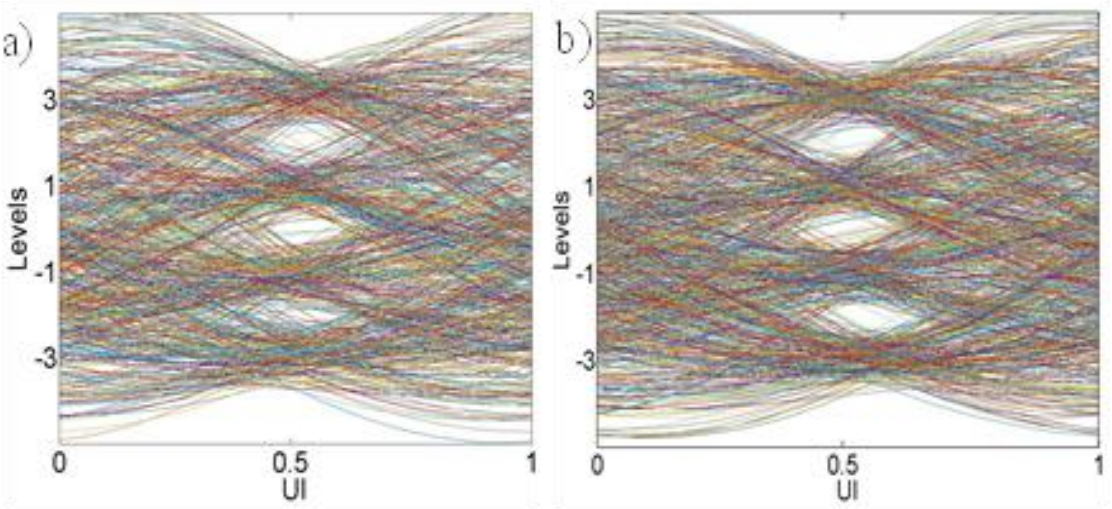

Fig. 4.15: Received unequalized eyes at (a) 940nm and (b) 850nm for OM5.

940nm for both B2B and WBF scenarios and compares it to the results obtained at 850nm. It can be seen from Fig. 10 that there is a 4dB and 6dB penalty from the thermal limit. Within these penalties, 2.29dB is associated with noise enhancement from receiver equalization, which was calculated from Eq. (1) based off the receiver equalization response in Fig. 4.13. Approximately 0.6dB is associated with the RIN of the VCSEL, calculated from the measured average RIN of the VCSEL (-142dB/Hz) and parameters of the link using our PAM-4 analytic model mentioned in [115]. Another 0.3dB penalty is associated with the ISI penalty at this particular bitrate/(link-bandwidth) (3.8), which is calculated from Eq. (7) and shown in Fig. 4.6. Additional penalties could be a result of nonlinearities in the PAM-4 eyes, both timing and amplitude, which can be observed in both Fig. 4.12 and Fig. 4.15.

4.3 Error-Free 100Gbps PAM-4

New generation VCSELs have been shown to have low relative intensity and mode partition noise (RIN and MPN) penalties (section 3.1), demonstrating that data rates are

limited by bandwidth issues at the transmitter and/or receiver. Experimental efforts with PAM-2 VCSEL links have reached 57Gbps error-free with no equalization and 71Gbps over 3m error-free with transmitter equalization [116, 117]. Additionally, several research groups have achieved 100Gbps and beyond using more complex modulation formats and FEC with transmitter and receiver equalization [118]. Although PAM-4 may enable higher data rates and longer reach [118], PAM-4 is generally less power efficient and requires more complex coding and decoding. Solutions that require FEC also add considerable latency and are not considered to be an option for high performance computing applications. Therefore, different VCSEL MMF links, with varying complexity and features (modulation format, equalization format, and forward error correction) need to be studied.

In this section, we demonstrate greater than 100Gbps PAM-4 error-free signaling over 100m of SWDM capable fiber; LaserWave *FLEX* WideBand Multimode Fiber [103] (OM5). Equalization is implemented exclusively at the transmitter as pre-emphasis. We study the maximum achievable error free ($BER<10^{-12}$) data rates for both PAM-2 and PAM-4. Additionally, we investigate the benefits of pulse shaping within the band limited VCSEL links. Furthermore, we study four sets of three VCSELs, with each set having a different aperture diameter of 5.1μm, 7.3μm, 9.2μm, or 11.2μm. The power penalties for each VCSEL, modulation format, and pulse shape are compared.

4.3.1 Experimental Setup

The VCSELs in this study were 3rd generation high-speed VCSELs from Chalmers University. The oxide-confined 850 nm VCSELs were designed for high-speed modulation

using strained InGaAs quantum wells, a short optical cavity, and multiple oxide apertures [119]. The reflectivity of the top mirror was adjusted in a post-fabrication process for the VCSELs to have a flat and high-bandwidth modulation response [120]. The VCSELs were driven by a 92GSa/s Arbitrary Waveform Generator (AWG) with 32GHz of analog bandwidth (Keysight Technologies M8196). Each VCSEL is capable of >20GHz bandwidth. A peak-to-peak voltage swing of 900mV was used to drive each VCSEL for all reported data. Details of the experiment are similar to our previous work [105] with a few alterations. In the case of the shaped pulses, a time-domain raised cosine (RC) filter with 0.3 roll-off factor is used. The optical signal was muxed and demuxed into and out of the WBF to demonstrate SWDM compatibility. The Huber-Suhner Cube Optics Mux/Demux added an additional 2.7dB loss. Lastly, all BER measurements were done with an SHF 11100 A. In the case of PAM-4, the error rate is evaluated by measuring the symbol error rate of each eye at identical sampling points, and then summing half the individual eye error rates [101], this is described in detail in section 2.4.4.

4.3.2 PAM-2

To quantify the tradeoffs between PAM-2 and PAM-4 we compare the performance of both formats over a wide range of bitrates. We first determine the receiver thermal noise limit for PAM-2 including extinction ratio (ER), the responsivity of the photodiode (including coupling loss), and the thermal noise at the output of the receiver. This

represents the best case BER if the modulated optical signal were free of impairments; ISI, RIN, jitter, or MPN.

Unshaped (UnS) pulses are tested with PAM-2 modulation. Unshaped pulses are

Table 4.1: Maximum achievable error free data rates over 100m MMF using PAM-2.

VCSEL Aper. (μm)	Max Data Rate (Gbps)					
	UnS PAM-2			**RC PAM-2**		
	VCSEL #			VCSEL #		
	1	2	3	1	2	3
5.1	58	58	58	62	60	58
7.3	64	62	60	68	68	68
9.2	62	62	60	68	66	68
11.2	60	58	60	68	68	68

Table 4.2: RIN and Enhanced RIN for all tested VCSELs

VCSEL Aper. (μm)	**RIN (-dB/Hz)**			**Enhanced RIN (-dB/Hz)**		
	VCSEL #			VCSEL #		
	1	2	3	1	2	3
5.1	153	155	155	151	152	152
7.3	151	150	152	150	149	150
9.2	147	149	148	144	146	146
11.2	145	146	146	141	143	142

limited only by the bandwidth of the electrical AWG and the intrinsic bandwidth of the equalized link. The maximum achievable data rate through 100m of MMF is 64Gbps, the minimum is 58, Table 4.1. The results were consistent for the 3 VCSELs of each set.

When applying RC pulse shaping an increase of the data rate is observed. The larger aperture VCSELs show a larger increase likely due to the larger extinction ratio capability resulting from their larger slope efficiency. The 5μm VCSEL exhibited an ER of ~6.5dB while the other VCSELs had an ER of ~8dB.

All VCSELs have less than -141dB/Hz enhanced RIN (RIN value after 100m of fiber). The smaller aperture VCSELs produce a smaller RIN and thus have less enhanced RIN compared to the larger apertures, Table. 4.2. The 5, 7, 9, and 11μm VCSELs were biased near 4, 8, 13, and 20mA, respectively.

Figure 4.16 depicts the BER vs received power for the 9mm VCSEL. The behavior, and that of each of the other VCSELs, is free of any noise floor and demonstrates a penalty dominated by ISI compared to the best case thermal limited result.

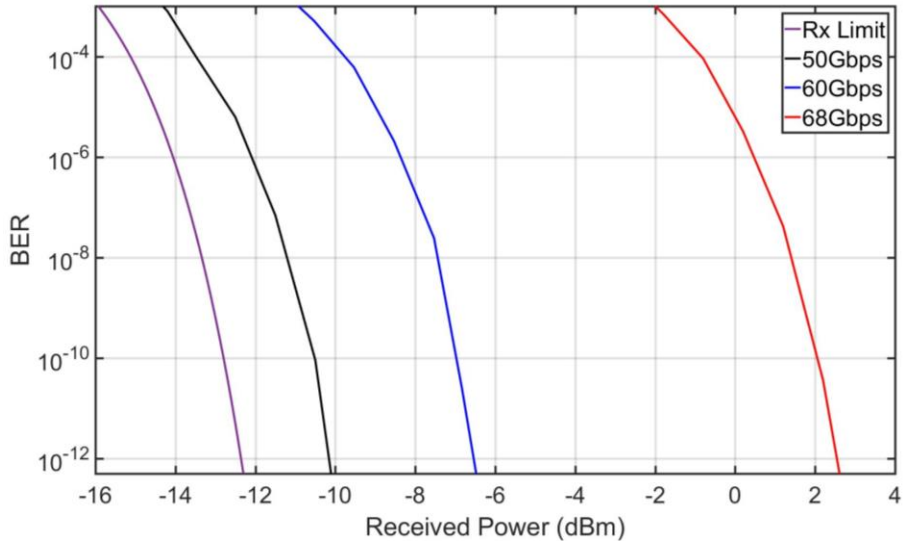

Fig. 4.16: BER vs. received power for PAM-2 for various bit rates on an equalized 100m OM5 channel using RC pulses with a 9μm VCSEL and an ER of ~8dB.

Using our analytic link model based off the IEEE spreadsheet model, we determine that RIN and MPN adds at most a 1.5dB power penalty for the 5μm aperture VCSELs and up to 3dB for the 11μm aperture VCSELs. The vast majority of the link penalty, up to 10dB, is a combination of residual ISI from bandwidth limitation and aliasing as the data rates reach >46Gbps. The difference in noise and extinction ratio between each VCSEL aperture has a minor effect.

4.3.3 PAM-4

Table 4.3: Maximum Data Rates for PAM-4

VCSEL Aper. (μm)	Max Data Rate (Gbps)					
	UnS PAM-4			**RC PAM-4**		
	VCSEL #			VCSEL #		
	1	2	3	1	2	3
5.1	84	80	82	96	88	92
7.3	90	88	90	110	102	104
9.2	88	84	86	104	102	100
11.2	84	86	82	92	98	100

PAM-4 offers the lowest implementation complexity for all formats with 2 bits/symbol with transceivers already commercially available for up to 50Gbps []. Similar to the PAM-2 setup, we determine the receiver thermal noise limit for PAM-4. The addition of two more amplitude levels results in a sensitivity penalty of dB compared to PAM-2. PAM-4 benefits from a large ER, low RIN and may be the format of choice with strongly band limited channels. Furthermore, the addition of two more amplitude levels also increases the link sensitivity to noise.

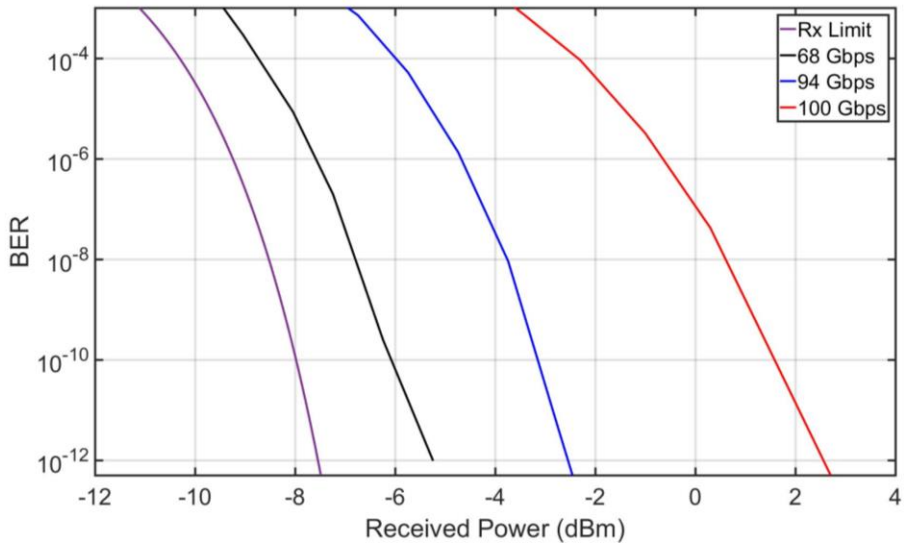

Fig. 4.17: BER vs. received power for PAM-4 for various bit rates on an equalized 100m OM5 channel using RC pulses with a 9μm VCSEL and an ER of ~8dB.

PAM-4 modulation was evaluated with both UnS and RC pulses. The same bias points were used in the PAM-4 and PAM-2 experiments. For PAM-4, the 7 and 9μm

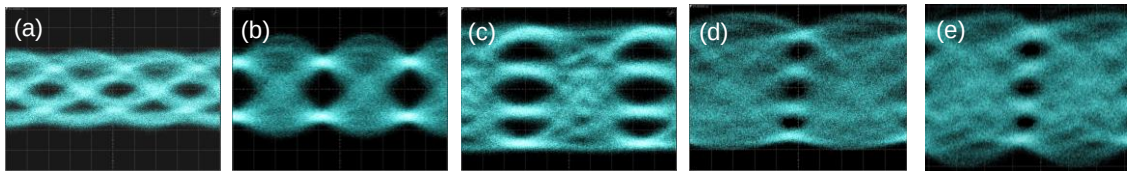

Fig. 4.18: Error-free eye diagrams: (a) PAM-2 UnS 60Gbps, (b) PAM-2 RC 68Gbps, (c) PAM-4 UnS 90Gbps, (d) PAM-4 RC 100Gbps, (e) PAM-4 RC 110Gbps

VCSELs perform best due to their high ER and low RIN. Figure 4.17 shows the BER vs. received power and depicts ISI dominated performance up to 94Gbps. The 100Gps results

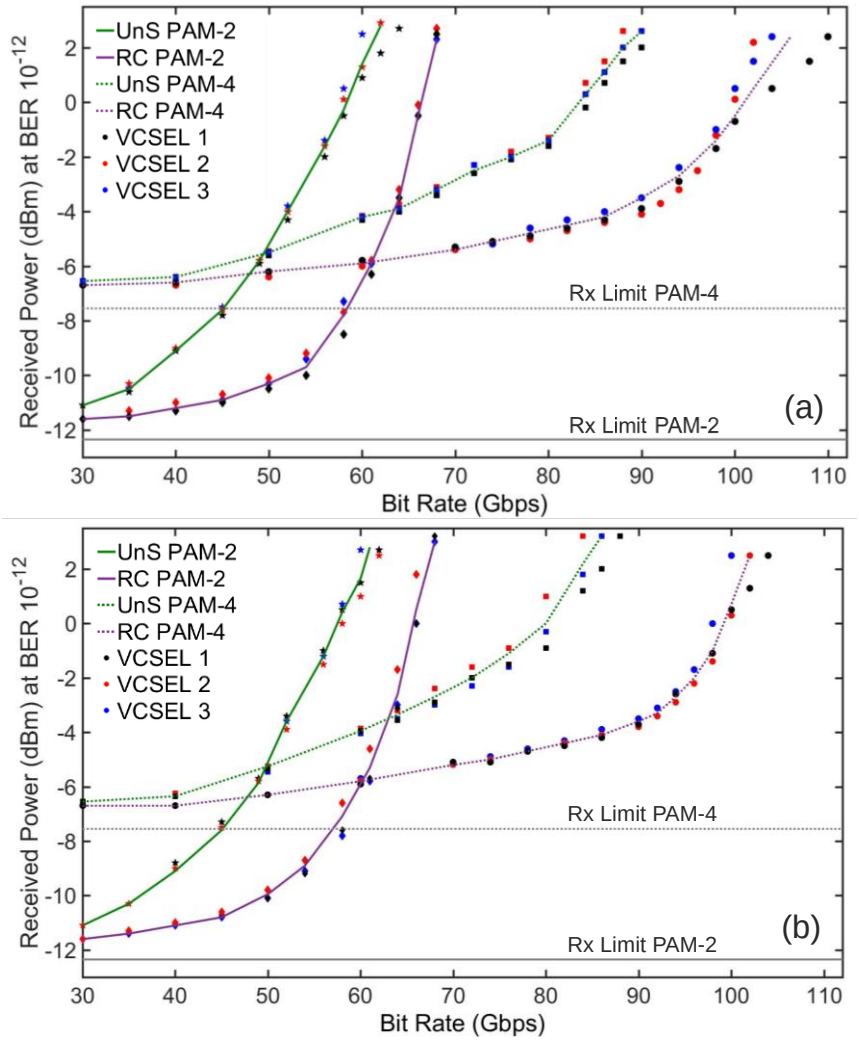

Fig. 4.19: Received power (BER 10^{-12}) vs. bit rate for PAM-2 and PAM-4 using both UnS and RC pulses on an equalized channel with aperture size 7μm (a), and 9μm (b). Black, red and blue represent VCSEL 1, 2, and 3, respectively. The green and purple lines show the bit rate trends for their respective shaping and modulation format. All data is through 100m OM5 with ER of ~8dB.

reveal some indication of a noise floor. Error-free eye diagrams comparing PAM-2 and PAM-4 are displayed in Figure 4.18.

Figure 4.19 compares the power penalty of both PAM-2 and PAM-4 for the 7μm (4a) and 9μm (4b) apertures. The results from all VCSELs are depicted demonstrating excellent uniformity among similar VCSELs. PAM-2 outperforms PAM-4 for bitrates <50Gbps (UnS) and <60Gbps (RC). The crossing of the similar colored trend lines identifies where PAM-4 begins to outperform PAM-2. Using UnS pulses with PAM-4, data rates of 90Gbps were achievable, Table 4.3. Pulse shaping with the RC filter yields substantial benefits for PAM-4 increasing data rates ~20Gbps up to 110Gbps. Shaping provides ~20% bitrate increase for both PAM-2 and Pam-4. From the increasing power penalties at high bitrates shown in Fig. 4.19 we see that even modest increases in component bandwidths will provide significant margin increases further enabling error-free 100Gbps VCSEL- MMF links.

4.4 Power Efficient Modulation Formats for Error-Free VCSEL MMF Links

Power efficient VCSEL based optical links are essential for data centers and high performance computing centers since data center capacity growth is limited by power considerations Current IEEE standards 802.3bm and 802.3cd define 10Gbps, 25Gbps and 50Gbps core rates for current 100Gbps modules and future 400Gbps solutions. Currently VCSEL links are mainly used for server to top of rack (TOR) connections, but could evolve into a higher data rate substitute for passive copper cable, server to middle of rack (MOR) solutions at 30m [121], or even low power >1km inter data center connections [122]. Regardless, as bandwidth capacity requirements grow and server switch radix increase

from 128 to 256, the demand for low power high speed links will increase. Thus, using as many VCSEL links as possible will keep data center costs and power consumption the lowest [123]. Since VCSEL links are primarily bandlimited by the laser, increases in data rates are directly coupled with advances in VCSEL bandwidth, which have increased from 18GHz to 30GHz over the last decade. The economics of short reach links strongly limit the complexity of any signal processing used to enhance capacity Furthermore, FEC adds latency and increase power requirements and should be minimized or avoided. Thus PAM-4, electrical duobinary [124], and efficient channel equalization have been investigated.

In this section, we quantify the effectiveness, from a received power perspective, of PAM-2, PAM-4, and duobinary at 25Gbps, 50Gbps and 100Gbps. Equalization strategies include only transmitter based pre-emphasis. We exclude FEC and therefore focus on error-free performance. We quantify the power penalty versus data rate and reach for each modulation format and identify an optimum data format based on the required bitrate and available intrinsic channel bandwidth.

4.4.1 Modulation Formats

PAM-4 was introduced to increase the bitrate in bandlimited channels at the cost of an increase in required optical power received. When thermal noise is dominant, the optical received power penalty for using M-level PAM compared to PAM-2 increases by $10\log_{10}(M-1)$, at the same symbol rate, where M is the number of PAM levels. PAM-2 and PAM-4 are both implementable with low complexity, requiring one and four electronic operations per bit at the transmitter, respectively. PAM-3 is not as attractive due to its more complex implementation. In contrast, duobinary is a low complexity signaling

Table 4.4**:** Complexity and Power Penalty for Modulation Formats

Modulation Format	Operations per bit (Includes EQ.)	Received Power Penalty
PAM-2	21	0
Duobinary	23	3dB
PAM-4	24	4.77dB

solution that provides an increase in bitrate while reducing the received power penalty compared to PAM-4. Furthermore, duobinary has the same horizontal eye opening as PAM-2 for equivalent symbol rates and increases the bitrate by $(M-1)$ rather than $\log_2 M$ of PAM signals. Table 4.4 lists the number of electronic operations per bit of PAM-2, PAM-4, and duobinary (including equalization provided by the DAC) as well as the calculated optical received power penalty at the receiver. Note that all three modulation formats have similar transmitter complexity. Thus, all three formats could be used with similar transmitter power requirements. The experimental setup was similar to that listed in section 4.3.1.

4.4.2 Experimental Results

The sensitivity of the three modulation formats were evaluated for bit rates from 24Gbps to maximum error-free bit rate achievable through 100m of OFS OM5 fiber. The rise and fall time of the electrical drive signal is limited by the DAC analog bandwidth. Figure 4.20 shows the received power required for each format versus bit rate at 8mA bias. For bit rates <45Gbps the better receiver sensitivity of PAM-2 makes it the most power efficient format. As the bit rate increases, PAM-2 and PAM-4 reach the same efficiency near 50Gbps after 100m of fiber. Duobinary is the most efficient modulation format between 48Gbps and 68Gbps. At 50Gbps, duobinary is ~2dB more power efficient than

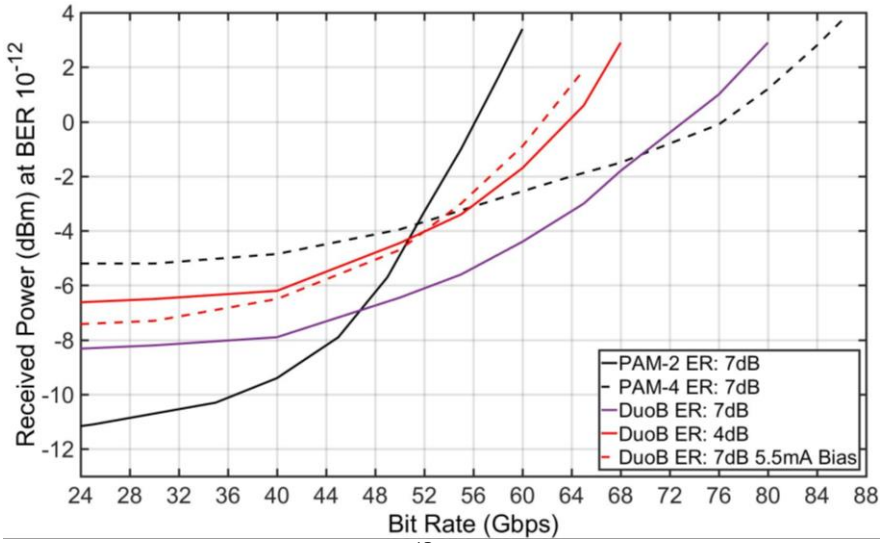

Fig. 4.20: Received power (dBm) at 10^{-12} BER for various bit rates on an equalized channel with a 7µm VCSEL. All data is taken through 100m OM5 fiber.

either PAM-2 or PAM-4, making it an excellent solution for reducing the power required for a 50G link. At 100m; power efficiency can be increased by lowering the DC bias of the VCSEL or decreasing the electrical drive swing (optical ER). If the ER is kept constant, the DC bias of the VCSEL can be lowered from 8mA to 5.5mA reducing the power by 2.21dB, Fig. 4.20. For a constant DC bias, the electrical drive swing voltage reduces significantly as the required ER decreases, Table 4.5. At an ER of 4dB, the voltage reduction is a substantial 5.28dB. For data rates >85Gbps error-free links are no longer possible with just transmitter equalization. However, with additional filtering in the form of pulse shaping, VCSEL links can reach beyond 100Gbps using a PAM-4 modulation. In theory, duobinary should also be able to reach the same rates. However, duobinary

Table. 4.5: Drive swing power required for a given ER

Extinction Ratio (ER)	Electrical Drive	
	V_{RMS}	ΔdB
4dB	0.173	-5.28
5dB	0.212	-3.51
6dB	0.256	-1.88
7dB	0.318	0

signaling at 100Gbps requires 100GSa/s to properly implement. This further complicates the transmitter and is beyond the capabilities of the DAC used here.

With the most power efficient 25Gbps, 50Gbps and 100Gbps error-free VCSEL links established, we next quantify the maximum fiber reach. For 25Gbps, all formats are able to achieve 500m reach error-free, Fig. 4.21a. Even though PAM-2 has the smallest sensitivity penalty, all formats require nearly identical received power at longer reach. This

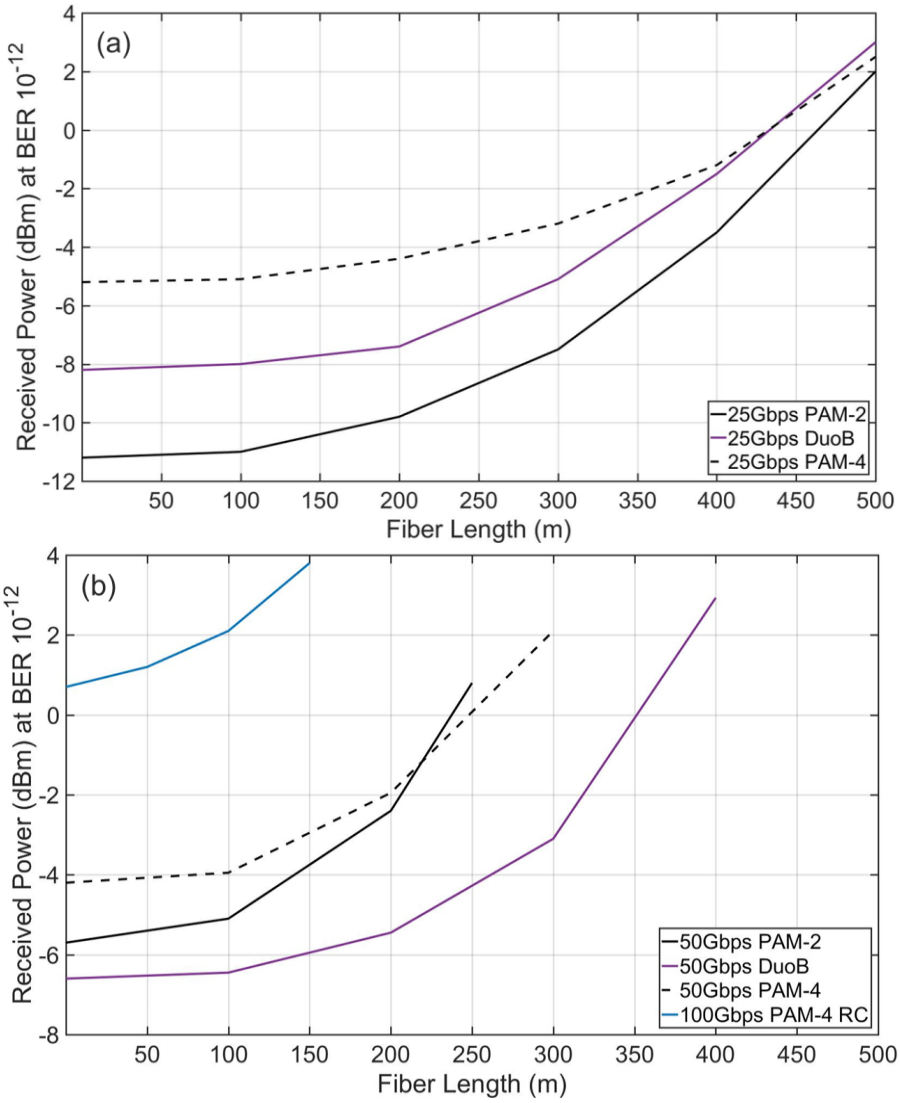

Fig. 4.21: Received power (dBm) at 10^{-12} BER for various fiber lengths on an equalized channel with a 7μm VCSEL and 7dB ER. (a) PAM-2, PAM-4, and duobinary at 25 Gbps; (b) PAM-2, PAM-4, and duobinary at 50 Gbps and PAM-4 RC at 100Gbps.

results from the increasing effects of dispersion and modal bandwidth resulting in an ISI penalty which dominates at long reach for 25Gbps links. For 50Gbps links the bandwidth limitations result in a back to back performance with only a 2dB benefit for PAM-2. Thus the effects of dispersion and modal bandwidth which are also enhanced at higher data rates results in PAM-2 and PAM-4 requiring equal received optical power at 225m, Fig 4.21b. The error-free reach is 250m and 300m, respectively. In contrast, the correlative coding intrinsic to duobinary results in a lower bandwidth requirement for the same bit rate and thus duobinary is able to reach 400m error-free. This clearly demonstrates deployment opportunities for duobinary. Most importantly, these results demonstrate that 25Gbps and 50Gbps VCSEL MMF links are suitable for mid-range up to 500m links and are thus appropriate for most intra data center links.

We further evaluated each format to determine suitability for 100Gbps links. Only PAM-4 with raised cosine pulse shaping at the transmitter was able to achieve error-free performance. The maximum 100Gbps reach is 150m and is thus appropriate for a large

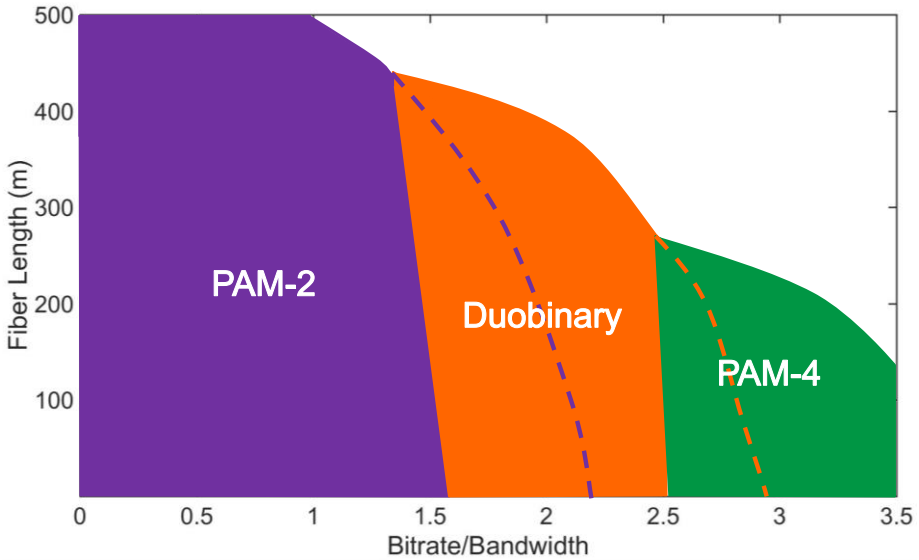

Fig. 4.22: Best modulation format for an error-free link from 0 to 500m at a given Bitrate/Bandwidth based on power efficiency. The dashed lines represent the maximum error-free reach for each format at the corresponding bitrate/bandwidth.

number DC links since many cable lengths in data centers are 30m or less and would benefit from a power-efficient 100Gbps solution.

As noted, the VCSEL bandwidth dominates link bandwidths and hence modest improvements in VCSELs will provide a commensurate increase in in performance. Furthermore, there is a tradeoff between equalization complexity and power requirements. Hence, it is useful to examine format performance from the perspective of the required bitrate and available channel bandwidth. Specifically, the link characteristic of merit is the ratio of bitrate to equalized channel bandwidth. Figure 4.22 depicts the fiber reach achievable with the lowest received optical power for each format for each normalized bitrate. There is a clear best format for each normalized bit rate and there is a large bitrate range where duobinary provides an advantage over PAM-2 and PAM-4. Note that when the fiber reach increases, the transition between optimum formats is dependent on the normalized bit rate due to residual ISI resulting from fiber dispersion. Importantly, while these results correspond to a specific set of VCSELs, and fiber, the behavior is general for different MMF fiber and multimode VCSELs.

CHAPTER 5.

SHORTWAVE DIVISION MULTIPLEXING (SWDM)

IEEE standard 802.3bm and the future 802.3cm standard define 10Gbps PAM-2, 25Gbps PAM-2 and 50Gbps PAM-4 core rates for current 100Gbps, and future 200Gbps and 400Gbps modules. Hence, a 400Gbps link requires 8 fibers per direction. Scaling VCSEL links to >400Gbps will require faster line rates with higher modulation formats and wave division multiplexing. PAM-4 [125] and short wave division multiplexing (SWDM) over OM5 [126] are both currently being standardized in the IEEE 802.3 Ethernet Working Group [127].

Faster data rates may be feasible, however the bandwidth limits of VCSEL MMF links would require complex receiver DSP and FEC schemes that add latency. Therefore, scaling by wavelength multiplexing will be a more cost effective solution. It has been shown that 100Gbps PAM-4 is feasible in the previous Chapter. However, the continual growth of data centers will demand higher capacity short reach solutions for 800GbE/1.6TbE solutions. Thus, capacity will need to scale to more wavelengths to meet this demand.

In this Chapter, we investigate the ability to wave division multiplex 4 different wavelengths operating at 100Gbps over 100m OM5 fiber. To further increase fiber capacity, we investigate the upper wavelength limit of VCSEL technology at 1060nm. Lastly, we compare the improvement of different equalization strategies at the transmitter and receiver

5.1 4λ x 100Gbps VCSEL PAM-4 Transmission over Wideband MMF

Short reach optical interconnects, here defined to have reach <500m, are dominated by intensity-modulated VCSELs with direct-detection over MMF due to low power per bit, lower cost and high density. Serial SWDM 50Gbps links have been demonstrated using PAM-2 [117]. In the case of PAM-2, 107m 850nm VCSEL links have been reported with BER $<10^{-12}$ to 60Gbps [128]. For PAM-4, data rates of 112Gbps [129] and 107Gbps have been demonstrated to 100m, but require forward error-correction (FEC) to achieve BER $<10^{-12}$. In this manuscript we use the term PAM-2 to be consistent with PAM-4 in place of the more common NRZ or more precise binary-NRZ.

The primary link limitation is the channel bandwidth, owing to limited VCSEL bandwidth. Higher line rates therefore require both channel equalization and efficient bandwidth usage. Therefore, exploring different signaling strategies within an SWDM link; i) channel equalization, ii) pulse shaping and iii) and modulation formats will provide insight into further increasing data rates. Many VCSEL-MMF links now include some equalization [128, 129], which enables bandlimited pulse shaping like raised cosine (RC), while maintaining low complexity. We believe that this, together with SWDM, enables scaling to 400Gbps and beyond.

In this section, we demonstrate 100Gbps PAM-4 transmission below the FEC threshold using 850nm, 880nm, 910nm, and 940nm VCSELs over 100m wideband MMF (OM5). Through advancements in both VCSELs and photoreceivers, we show 50Gbps PAM-2 and 100Gbps PAM-4 are achievable with next generation technology. These

results demonstrate a feasible path to 400GbE single MMF solutions. *We color code the 850nm, 880nm, 910nm, and 940nm wavelengths blue, green, gold, and red, respectively*.

5.1.1 Transmitter: Equalization and Pulse Shaping

Modern VCSEL drive circuits now include a multi-tap analog FIR filter and a wideband line driver. We examine a number of transmitter filtering strategies to assess the impact on link performance. One method is to simply equalize the channel response where the equalization is limited by the filter complexity and added noise considerations. The channel here includes the line driver, amplifier, and everything to, and including, the receiver TIA. A second filtering option allows for deliberate shaping of the electrical drive signal to produce a near Nyquist pulse and thereby reduce ISI. We note that both techniques reduce ISI by improving the received signal spectra and will therefore have similar effects when implemented separately. However, pulse shaping generally requires stricter spectral control and is therefore more complex to implement.

The observed channel response exhibits a 3rd order Gaussian frequency response with a 3dB frequency of <20GHz. With equalization we extend this to ~27GHz although the channel response above 30GHz is negligible. We specifically limited the equalization to <10dB gain so that the filter can be implemented with a relatively simple FIR structure or a passive analog filter.

The reference case, which we call unshaped (UnS), relies on the DAC to create the drive signal by holding the symbol value constant over all samples within the symbol period. The rise-fall times of the drive signal is strictly limited by the DAC analog

bandwidth. The signal is further truncated by the channel response. Since this channel frequency response is fixed, it impacts the performance differently at different baud rates.

Actively shaping the pulse allows a reduction of the ISI. We implemented an electrical drive with a RC frequency response:

$$H_{RC}(f) = \begin{cases} T, & |f| \le \frac{1-\beta}{2T} \\ \frac{T}{2}\left[1 + \cos\left(\frac{\pi T}{\beta}\left[|f| - \frac{1-\beta}{2T}\right]\right)\right], & \frac{1-\beta}{2T} < |f| \le \frac{1+\beta}{2T} \\ 0, & otherwise \end{cases} \quad (5.1)$$

where β is the roll-off factor chosen to be a readily achievable 0.1. The filter used to approximate the RC spectral shape was limited to 11 T/2 taps (5 symbols). The 0.13μm SiGe BiCMOS process provides the gain and bandwidth necessary to create these 11-tap analog FIR filters for 50GBd waveforms [130]. The RC spectra for a 50GBd signal is compared to the UnS spectra and the equalized channel response in Fig. 4. We emphasize that these drive signals are clearly sufficient for 25GBd signaling. The RC signal is optimized for the available channel bandwidth limited by the VCSEL bandwidth and therefore represents the optimum signaling for higher baud rates. We examine 4 filtering strategies; with and without channel equalization and with and without pulse shaping. All four of these are investigated using PAM-2 and PAM-4 formats.

5.1.2 PAM-2 (NRZ)

To understand the tradeoffs and benefits of pulse shaping and equalization, we first experimentally determine the PAM-2 BER performance for a wide range of baud rates. As reference we identify the thermal noise limited performance for a receiver with 29GHz bandwidth. This represents the best case BER without intersymbol interference (ISI), RIN,

jitter, or mode partition noise (MPN) impairments.

The equalized channel with UnS pulses supports error-free performance to 44Gbps using PAM-2 for all 4 VCSEL wavelengths, Fig. 5.1, limited by available received power. Baud rates below 30Gbps exhibited performance near the thermal limit. The BER behavior also shows all VCSELs have nearly identical performance with no sign of a noise floor and a near uniform power penalty consistent with an ISI dominant penalty.

RC pulse shaping, Fig. 5.1, systematically improves performance; the power penalty is decreased for all bitrates compared to the unshaped transmission and the maximum error-free bit rate is increased from 44Gbps to 54Gbps. Again, there is no evidence of a noise floor. The lower power penalty of RC signaling is attributed to the reduced ISI and increased energy in the center of the symbol period.

The back-to-back performance was evaluated for all baud rates. At lower baud rates, the back-to-back and through-fiber configurations behave nearly identically since the equalization, which is separately done for back-to-back and through fiber, compensates for any small channel differences. At maximum baud rates, the fiber imposes a small power penalty of <0.8dB without evidence of a noise floor.

RC pulse shaping consistently outperforms UnS pulses on the same equalized channel. The maximum UnS data rate increases from 40Gbps to 44Gbps with equalization

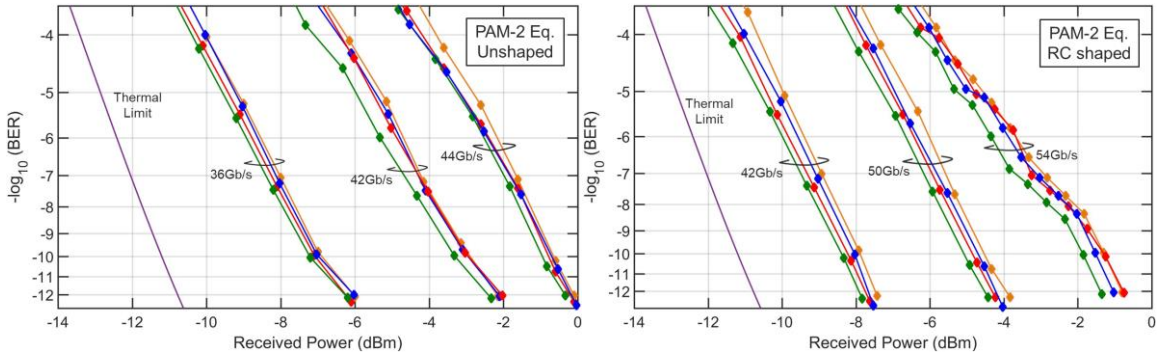

Fig. 5.1: (left) Unshaped PAM-2 performance on an equalized 27GHz channel, for all 4 VCSEL wavelengths; (right) RC shaped PAM-2 performance on an equalized 27GHz channel, for all 4 VCSEL wavelengths. Link includes 100m of OM5 with a 6dB ER.

and increases further to 54Gbps with RC pulse shaping. Thus, equalization and pulse shaping together increased the maximum error-free rate by 14Gbps. 50Gbps and higher was only achievable with both channel equalization and pulse shaping. A 5dB power penalty was incurred at 50Gbps PAM-2. From the perspective of required optical power, equalization benefits RC pulse shaping more than UnS. These results demonstrate the advantages of using both channel equalization and pulse shaping.

These results also show that VCSELs with wavelengths from 850nm to 950nm readily support error-free >40Gbps PAM-2 over 100m or more of OM5 fiber using simple transmitter based electronic filtering. Furthermore, 50Gbps serial rates can be achieved with additional filtering and penalty; however, modest VCSEL bandwidth improvements will enable 50Gbps serial rates with simple electronic filtering.

5.1.3 PAM-4

An alternative to 50Gbps PAM-2 is 25GBaud PAM-4. PAM-4 is currently under standardization for the IEEE standard 802.3cd and may also be a viable path to 100Gbps. A key challenge is to identify filtering strategies that enable PAM-4 without adding significant complexity. For brevity, we only investigated PAM-4 on the equalized channels. We also focus on data rates that can achieve error-free BERs since added latency of FEC is not tolerable in many applications of VCSEL/MMF links.

As reference, we again determine the receiver thermal noise limit for PAM-4 assuming equal optical modulation amplitude (OMA) between each eye and a 29GHz receiver bandwidth. The additional optical power penalty over PAM-2 is ~4.8dB [108].

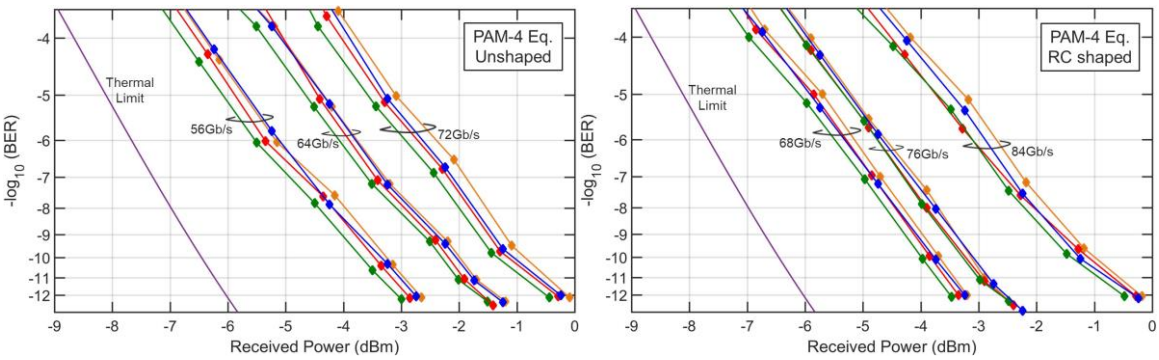

Fig. 5.2: (left) PAM-4 performance for 4 VCSEL wavelengths on an equalized channel using unshaped pulses; (right) PAM-4 performance for 4 VCSEL wavelengths on an equalized channel using RC pulses. Link includes 100m of OM5 and a 6dB ER.

Error analysis was accomplished by real-time counting using the error analyzer for each eye within the PAM-4 signal.

On the equalized channel, error-free PAM-4 performance is demonstrated to 72Gbps with UnS pulses, Fig. 5.2, and RC pulse shaping improves the maximum error free rate to 84Gbps, Fig. 5.2. Compared to PAM-2, PAM-4 always improves the maximum achievable data rate. Again, all wavelengths achieved error-free performance with very similar overall performance; no clear noise floor and penalties consistent with ISI. The results in Fig. 5.2 used the same filter as PAM-2, Fig. 5.1. Similar to PAM-2, the back-to-back and fiber configurations behave nearly identically at low baud rates. At maximum data rates, the fiber imposes a penalty up to 1.4dB but does not create a noticeable noise floor.

5.1.4 Comparison of PAM-2 and PAM-4

The required optical power to achieve an error-free BER is compared for data rates ≥24Gbps, Fig. 5.3. As demonstrated, PAM-4 significantly extends achievable error-free data rates but does not simply allow a doubling of the data rate compared to PAM-2. Notably, both formats approach the thermal limit of the receiver at low baud rates.

Neglecting the added complexity of a PAM-4 transceiver and only considering

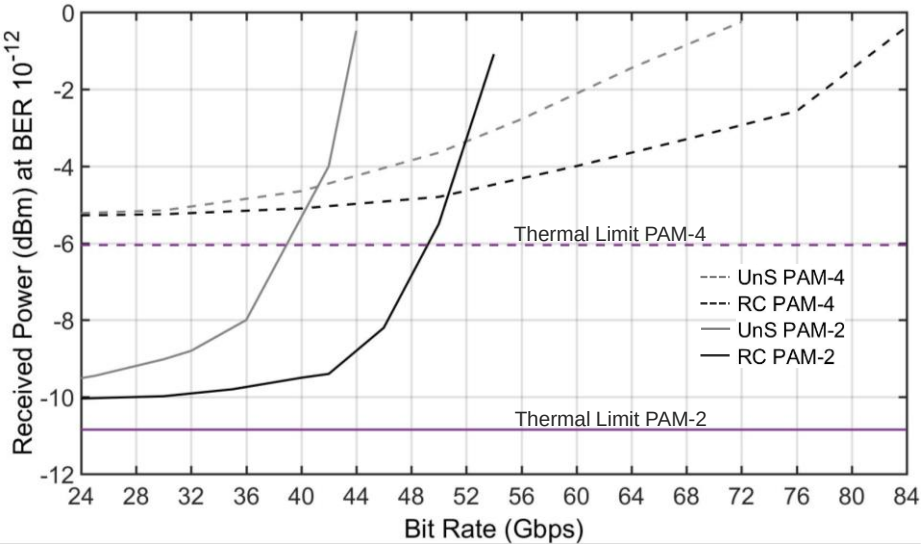

Fig. 5.3: Required received power for error-free (BER 10^{-12}) transmission with PAM-2 and PAM-4 on an equalized channel for the 850nm VCSEL. Link includes 100m of OM5 with ER of 6dB.

received power as the metric for choosing a modulation format, it is advantageous to choose PAM-4 for data rates ≥50Gbps. This assumes both equalization and pulse shaping are implemented. If just equalization is used the transition to PAM-4 occurs near 40Gbps. It is also clear that modest increases in channel bandwidth, again determined mostly by the VCSEL, allow PAM-2 to readily support 50Gbps and PAM-4 to support 100Gbps links.

Choosing a somewhat arbitrary maximum 3dB penalty over the thermal limit we observe that PAM-2 achieves 36Gbps and 45Gbps using equalization alone and equalization with shaping respectively. These correspond to a bitrate to bandwidth ratio of 1.33 and 1.67. In contrast PAM-4 exhibits a ratio of 1.96 and 2.64 for equalized and equalized with shaping respectively.

5.1.5 PAM-4 100Gbps and 400Gbps Links

Examination of the performance beyond 84Gbps i.e. beyond rates that achieve error free performance, we observe a monotonic increase in the minimum achievable BER reaching ~10^{-3} at 100Gbps without receiver equalization. Addition of a 7/3 receiver equalizer produces sub-FEC threshold BER (BER <$4.2x10^{-4}$) at effective bit rates as high as 104Gbps. This FEC threshold is based on the standard Reed Solomon (RS) code chosen by the IEEE for short reach links due to its low-latency and low-overhead characteristics [3].

We investigate in detail the performance of each VCSEL wavelength in both a back-to-back configuration as well as through 100m of OM5 with two different equalizers, Fig. 5.4. The 5/1 DFE produces sub-FEC threshold BER. The BER behaviors were consistent between all VCSELs and no burst errors were found in the captured data. Furthermore, there was no sign of a significant noise floor with this tap configuration.

Additionally, adding more equalizer taps lowers the BER revealing no floor above 10^{-6} BER. This suggests the main impairment in the signal is residual ISI. Since all transmissions were passed through a MUX/deMUX to the OM5 and the same equalization was used for each VCSEL wavelength, the 100Gbps rates could be combined easily for a 400Gbps link. In the back-to-back configuration, the 940nm VCSEL performs slightly better than the other VCSELs with the 910nm VCSEL performing the worst. We note that

Table 5.1: PAM-4 100Gbps Fiber Penalty vs. Wavelength

	Wavelength (nm)			
Fiber Penalty (dB)	850	880	910	940
	0.9	0.7	1.3	1.5

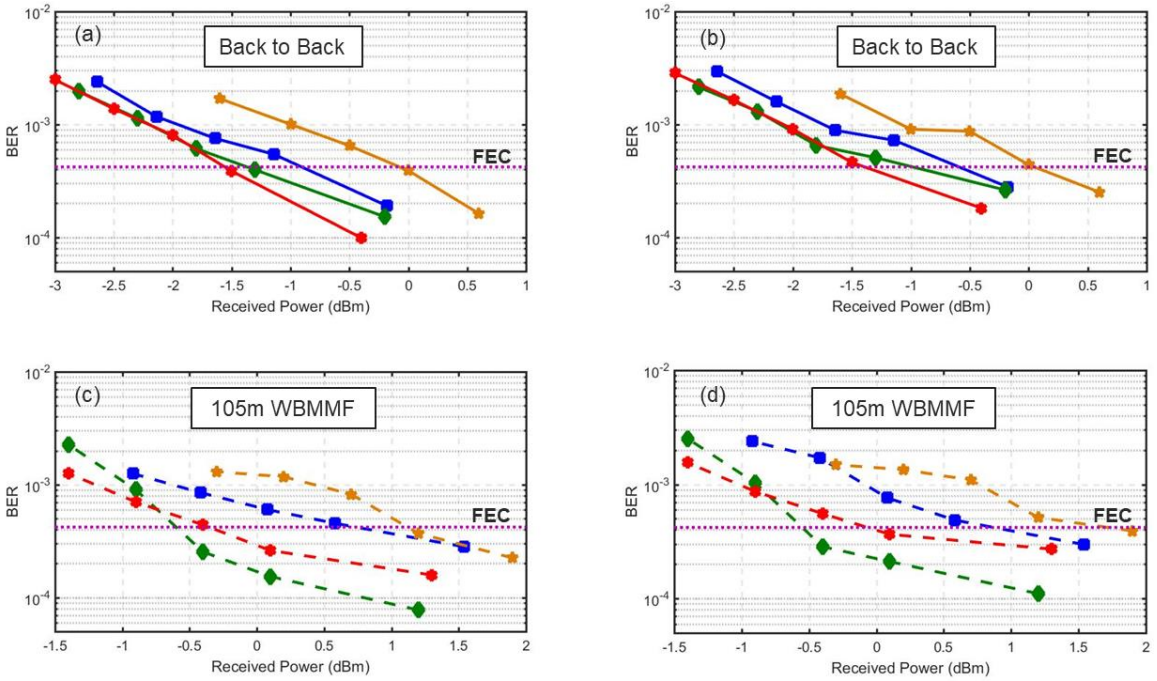

Fig. 5.4: PAM-4 performance for 4 VCSEL wavelengths with Tx and Rx equalization using RC pulses at 100Gbps. (a) BER after equalization for back-to-back (B2B) link with 7/3 forward/backward receiver equalizer and (b) BER after equalization for back-to-back (B2B) link with 5/1 forward/backward receiver equalizer; (c) OM5 link with 7/3 forward/backward receiver equalizer (d) and OM5 link with 5/1 forward/backward receiver equalizer.

the 910nm preproduction VCSELs have the worst performance of the four VCSELs by a minor, but consistent margin.

The OM5 fiber imposes only a small penalty that varies slightly among the four wavelengths at 100Gbps, Table 5.1. The fiber penalty varies with wavelength primarily due to the variation of the EMBc of the fiber. The 0.7dB penalty indicates that the peak bandwidth of the fiber is around 880nm. However, even at an effective 100Gbps the fiber penalty for all wavelengths is small compared to the ISI penalty.

If error-free data transmission is required, then an equalized bandwidth of ~30GHz, based off estimation from Fig. 5.4, is required to achieve 100Gbps. This estimate is in agreement with recent results where 68Gbps PAM-2 and >100Gbps PAM-4 were demonstrated error-free on a channel equalized to 30GHz in different work.

5.2 Error-Free 1060nm 100Gbps PAM-4 VCSEL Links

To reduce the fiber requirements, the IEEE Ethernet working group 802.3cm has started standardizing 50Gbps PAM-4 data rates as well as shortwave division multiplexing (SWDM) to transmit two wavelengths per fiber (850nm and 910nm) [131]. In order to support SWDM, multimode fiber (MMF) manufacturers have developed MMF which provides sufficient modal bandwidth (EMBc) from 850nm to 950nm [232]. These two efforts allow VCSEL-MMF links to scale capacity in two dimensions: data rates and wavelengths.

In this section, we investigate greater than 100Gbps PAM-4 signaling using 1060nm VCSELs over 100m of SWDM capable fiber; OFS LaserWave FLEX WideBand Multimode Fiber (OM5) [103]. Equalization is implemented exclusively at the transmitter as pre-emphasis. We study the maximum achievable error-free (BER $<10^{-12}$) data rates for PAM-2 and PAM-4 and reach 60Gbps and 100Gbps, respectively. Additionally, we investigate benefits of pulse shaping within band limited VCSEL links and find a reduction in power penalty of 4dB at 50Gbps and 3.5dB at 100Gbps. We conclusively show OM5 fiber is capable of supporting link transmission of the entire wavelength band of GaAs/InGaAs VCSEL Datacom technology (850nm to 1060nm).

5.2.1 Experimental Setup

The 1060 nm VCSEL design [122] has been developed from a previous 850nm high-speed GaAs-based design [119]. The active region of the VCSEL has three InGaAs quantum wells separated by partially strain-compensating GaAsP barriers. The short half-wavelength-thick cavity provides strong longitudinal optical confinement and is

surrounded by DBR structures carefully designed in the AlGaAs material system. Transverse optical and current confinement is achieved by two primary oxide layers in the top p-DBR, which are thin and placed in optical field nodes to obtain low beam divergence and improve transmission over longer distances.

The VCSELs were driven by a 92GSa/s Arbitrary Waveform Generator (AWG)

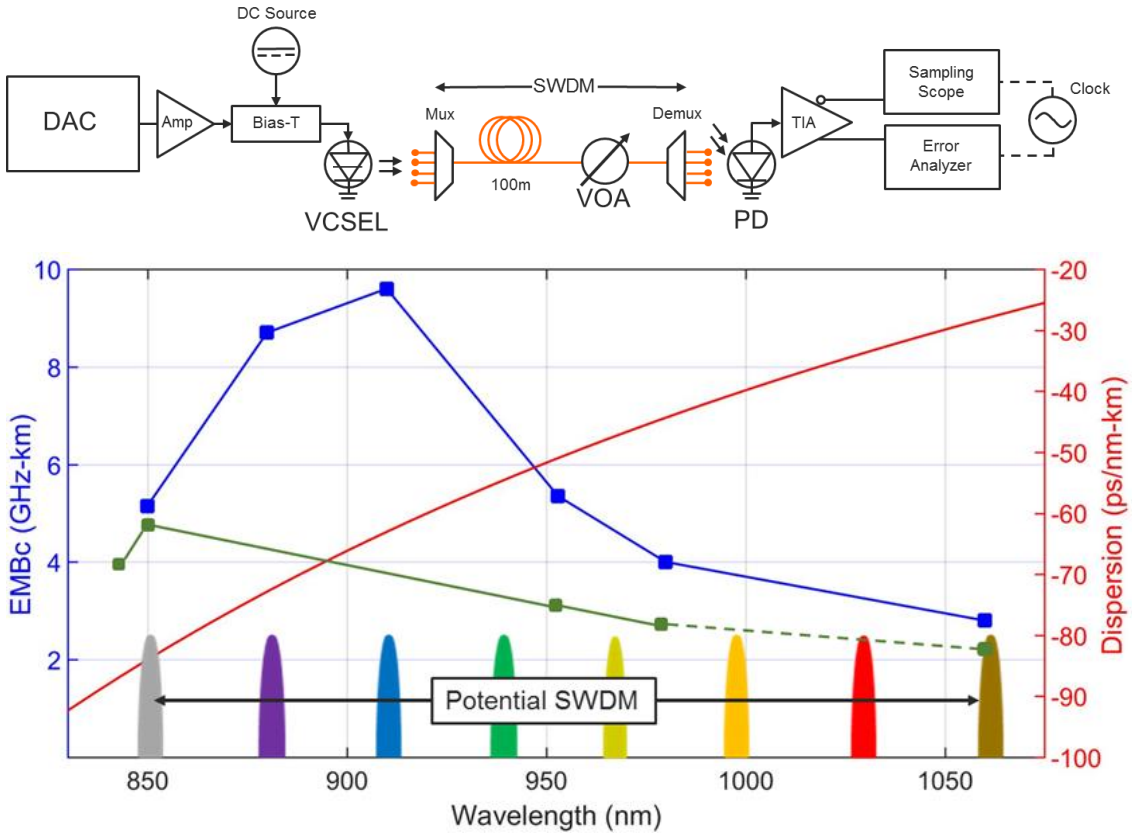

Fig. 5.5: (top) Experimental setup for BER measurements; (bottom) OM5 Fiber EMBc (blue) and fiber dispersion (red) over wavelength. ANSI/TIA492AAAE MMF standard (green) with approximated 1060nm (green dashed).

with 32GHz of analog bandwidth (Keysight Technologies M8196), Fig. 5.5top. The 5μm aperture VCSELs that were investigated had >23GHz bandwidth. A peak-to-peak voltage swing of 650mV was used to drive each VCSEL with a DC bias of ~6mA. Details of the experiment are similar to our previous work [113] with a few alterations. In the case of

investigating shaped pulses, a time-domain raised cosine (RC) filter with 0.35 roll off factor is used. The optical signal was attenuated by 3dB to emulate the loss from a MUX/deMUX. A Thor Labs DXM30BF Ultrafast Detector was used with an SHF 807 amplifier for the receiver. Lastly, all BER measurements were done with an SHF 11100A error rate analyzer. In the case of PAM-4, the error rate is evaluated by measuring the symbol error rate of each eye at identical sampling points, and then summing half the individual eye error rates.

5.2.2 Shortwave Division Multiplexing (SWDM) for 850nm to 1060nm VCSELs

The inclusion of SWDM in the next IEEE MMF standard allows continued scaling of VCSEL link capacity while alleviating strain on data rate requirements. The current standard is focusing on SR4.2 and SR8.2 links for 200GbE and 400GbE solutions, where SRx.2 represents x fibers with 2 wavelengths. These solutions require wideband MMF in order to support higher wavelengths with sufficient EMBc to limit modal dispersion. The ANSI/TIA-492AAAE OM5 fiber standard was crafted to support SWDM and requires a minEMBc of 4700MHz-km at 850nm and 2470MHz-km at 953nm, covering four wavelengths. The EMBc of the OM5 fiber surpasses the requirement, Fig. 5.5 bottom.

Fiber penalties in VCSEL MMF links are mostly dispersion related. The two worst case dispersion scenarios over the 850nm to 1060nm band in OM5 are at 850nm where chromatic dispersion is at a maximum and 1060nm where modal dispersion is at a maximum. Longer wavelengths have additional benefits due to the higher concentration of Indium in optoelectric devices such as smaller material bandgap (less fJs/bit) and higher responsivity of photodiodes. These benefits help further offset link penalties outside of the

primary design range of the fiber. By establishing link performance at 1060nm over OM5 fiber, and having already established 850nm, 880nm, 910nm, and 940nm performance, we now demonstrate that all wavelengths from 850 to 1060nm will behave in a similar fashion. With the standard at 30nm spacing, this includes 970nm, 1000nm, and 1030nm wavelengths for a potential 8 channels supported by a single MMF.

5.2.3 Channel Response and PAM-2

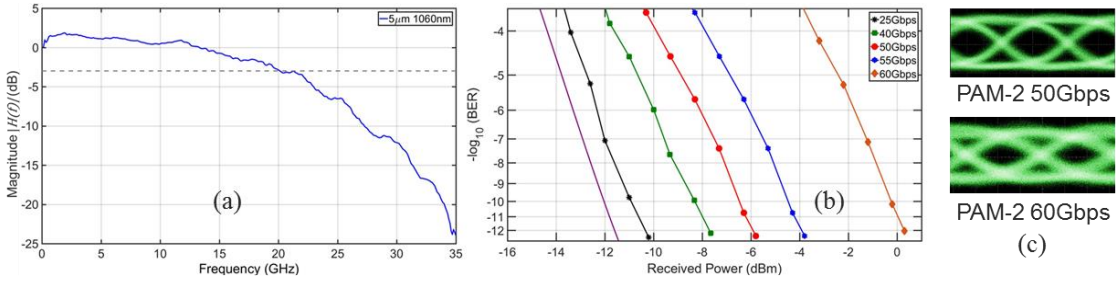

Fig. 5.6: (a) Unequalized electrical channel response (b) BER vs. received power for PAM-2 for various bit rates on an equalized 100m OM5 channel with extinction ratio of 7dB; (c) PAM-2 eye diagrams at 50Gbps and 60Gbps.

The channel response is taken with 100m of OM5. Even with an EMBc of ~2500MHz-km at 1060nm, the link 3dB bandwidth is ~20GHz, Fig 5.6a. With a 10-tap equalizer we are able to realize a link bandwidth of ~32GHz, where the equalizing filter is discussed in previous work [133]. The equalizer provides large bandwidth enhancement due to the slow roll off of the channel. This is attributed to advances in multimode photodiode bandwidth that reach >32GHz.

We examine PAM-2 error-free rates with a PRBS-15 signal using the same 1060nm VCSEL. An extinction ratio (ER) of 7dB is maintained across the examined bit rates. The receiver thermal limit is shown in Fig. 5.6b in purple. This represents the best case received power for a given BER limited only by thermal noise, responsivity, and VCSEL extinction ratio. At 25Gbps, deterministic ISI penalties are negligible. The majority of the <1dB

penalty is due to VCSEL noise including both relative intensity noise (RIN) and mode partition noise (MPN), as well as noise resulting from reflections at optical coupling points. As data rates reach 50Gbps, the optical power penalty reaches ~5.5dB. Residual ISI and DAC aliasing account for a maximum 4dB optical power penalty. The ISI penalty may be further reduced with larger transmitter filtering, however we limited our filter to at most 10 taps. The result is a 7dB power budget assuming a required power of -6dBm for PAM-2 at 50Gbps. Using all the available optical power we achieve 60Gbps over 100m of OM5, the maximum testable data rate for our BERT.

5.2.4 PAM-4

PAM-4 is used in band limited systems due to the increase in bits/symbol, lowering its required bandwidth for the same bitrate. PAM-4 benefits from a high ER laser and extends data rates in band limited channels. Similar to the PAM-2 setup, we determine the receiver thermal noise limit for PAM-4, Fig. 5.7a. The tradeoff for moving to a higher order modulation scheme is a 4.77dB ISI penalty. Additionally, the increase in level transitions makes PAM-4 more susceptible to nonlinearities of the VCSEL and RIN.

At 25Gbps, PAM-4 exhibits nearly the same inherent noise penalty as PAM-2. However, PAM-4 supports much higher data rates data rates without incurring the same ISI penalty as PAM-2, Fig. 5.7a and 5.7c. At 50Gbps, the residual ISI penalty is <0.5dB compared to 25Gbps. Power sensitivity is similar to PAM-2 as the ISI penalty of PAM-2 is nearly the same as the optical power penalty from increasing the amplitude levels. At 80Gbps, the band limitations of the channel contribute ~3dB ISI penalty compared to an ideal link. 100Gbps was achievable with a ~6dB power penalty. However, this establishes

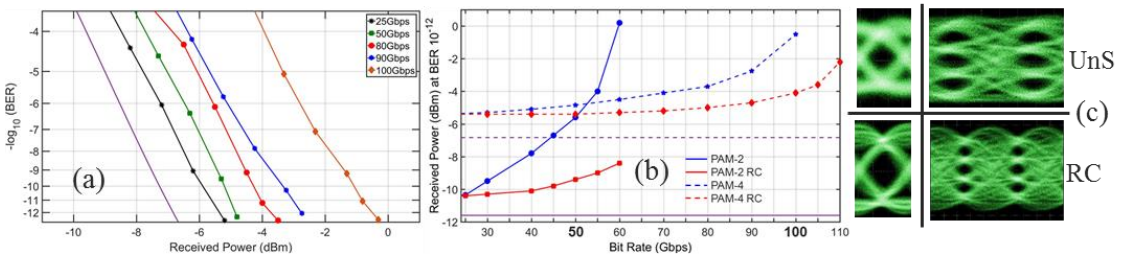

Fig. 5.7: (a) BER vs. received power for PAM-4 for various bit rates on an equalized 100m OM5 channel with extinction ratio of 7dB; (b) Received power (at BER 10^{-12}) vs. bit rate for PAM-2 (solid) and PAM-4 (dashed), including pulse shaping (red), on an equalized channel over 100m OM5. Thermal receiver limits are in purple; (c) eye diagrams of unshaped 60Gbps PAM-2 (top) and 100Gbps PAM-4 (top) and shaped 60Gbps (bottom) and 110Gbps (bottom).

that OM5 fiber can support 100Gbps PAM-4 with the upper wavelengths of GaAs/InGaAs VCSELs. We note again these are all error-free results.

We next added an additional filter to the transmitter to shape the electrical drive signal to yield Nyquist-like pulses further reducing ISI, Fig. 5.7b. We shape over 4 symbols with an RC filter with a 0.35 roll off. While this is a small filter, it is more complex to implement than the previous equalization since the tap spacing requirement is generally smaller. However, the penalties are substantially reduced, Fig. 5.7b and 5.7c. At 50Gbps, PAM-2 is achieved with a modest 2.5dB power penalty. 60Gbps performs error-free with a 3.5dB penalty, this was the maximum data rate of the BERT. The pulse shaping also had a large improvement on PAM-4. Most notably, the power penalty compared to an ideal link at 100Gbps was reduced to <3dB. This small penalty should provide a sufficient power budget for margins required in commercial deployment.

5.3 Error-Free 850nm to 1060nm VCSEL Links: 800Gbps 8λ-SWDM

Low cost, and high density capabilities of VCSEL-based transceivers make them a key component of short reach interconnects. The standards anticipate forward error

correction (FEC), however error free links without FEC are desirable in many applications. Error-free FEC-free VCSEL links have been demonstrated at 71Gbps PAM-2 over 3m [117] and 100Gbps PAM-4 over 100m [2, 3]. In the case of PAM-4, these data rates were demonstrated with multiple aperture and multiple wavelength VCSELs. Although faster data rates are feasible, bandwidth limits of VCSEL MMF links would require complex receiver DSP and FEC schemes that add latency and power consumption. Higher efficiency and low latency will be beneficial to deploy 50Gbps and 100Gbps single lane architectures. Therefore, scaling by wavelength multiplexing of error free links will be a more cost effective solution. It has been shown that 100Gbps PAM-4 is feasible across four wavelengths in the targeted OM5 range [133, 105]. Some performance and dispersion penalties have been investigated for both PAM-4 and longer wavelength VCSELs [134-135, 122], highlighting link budgets and PAM-4 advantages at 50Gbps. However, an assessment the distinct penalties across the entire possible SWDM range is necessary to better understand the full capability of future VCSEL links.

In this section, we investigate the effectiveness of limited transmitter equalization on 850nm, 980nm, and 1060nm VCSELs in back to back (b2b) and OM5 links. We compare the error-free sensitivity (BER 10^{-12}) for different equalizers sizes across all VCSEL wavelengths using PAM-2. Additionally, we measure a Q factor and determine a maximum bit rate. We also assess fiber penalties for both PAM-2 and PAM-4 through 100m of OM5 across all wavelengths. And, through simple measurements, we decompose total power penalty into individual dispersion related penalties, noise related penalties, and in the case of PAM-4, nonlinear related penalties.

5.3.1 Experimental Setup

The 850nm and 1060nm VCSELs were designed by Chalmers University and the 980nm VCSELs were designed by TU Berlin. All VCSELs had similar aperture sizes (5-6μm) with measured RMS spectral widths of 0.60, 0.51, and 0.41 for the 850nm, 980nm, and 1060nm VCSELs, respectively. The VCSELs were driven by a 92GSa/s Arbitrary

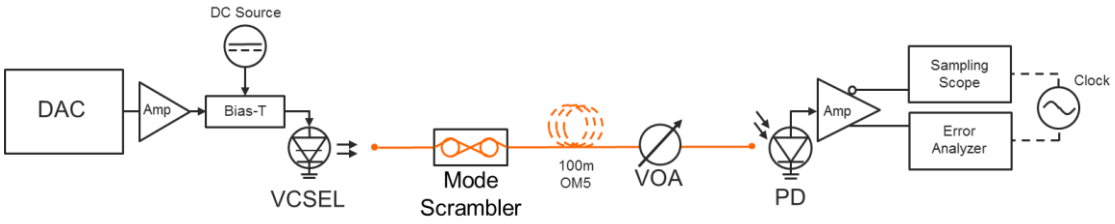

Fig. 5.8: Experimental setup for equalization and fiber penalty analysis. *The color scheme 850nm (blue), 980nm (green) and 1060nm (red) is used consistently throughout for all figures in section 5.3.*

Waveform Generator (AWG) with 32GHz of analog bandwidth (Keysight M8196) using a PRBS-15 pattern, Fig. 5.8. Experimental details are similar to earlier sections with a few alterations. When investigating shaped pulses, a time-domain raised cosine (RC) filter with 0.35 roll off is used. The optical signal is mode scrambled to create a worst-case overfilled launch and to ensure measurement consistency across different wavelengths. A Thor Labs DXM30BF Detector was used with an SHF 807 amplifier for the receiver. The measured channel response, including 100m of OM5 fiber, is nearly identical for all VCSELs. Lastly, all BER counting up to 60Gbaud was done with an SHF 11100A error rate analyzer. In the case of PAM-4, the error rate is evaluated by measuring the symbol error rate of each eye at identical sampling points, and then summing half the individual eye error rates.

5.3.2 Transmitter Equalization

Modern VCSEL drive circuits now include a multi-tap analogue FIR filter and a wideband line driver [130]. To quantify the benefits of transmitter equalization within an SWDM environment, we first demonstrate the error-free sensitivity improvement for bit

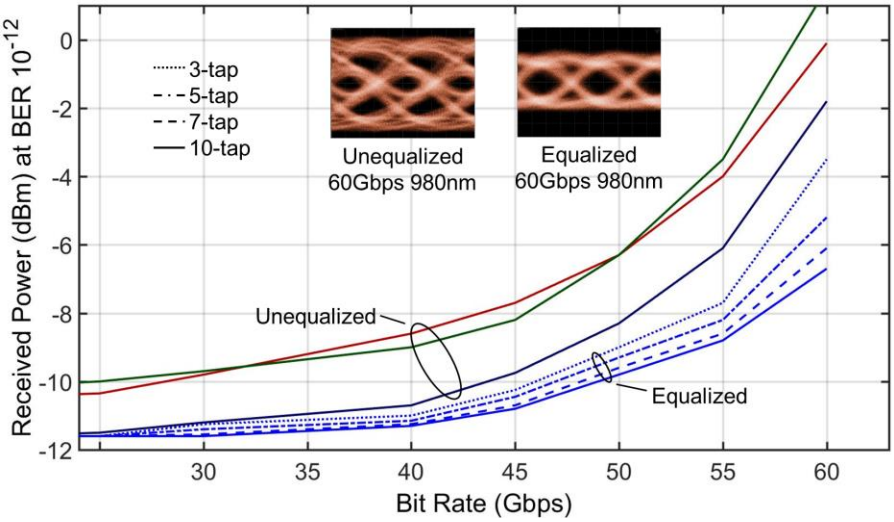

Fig. 5.9: Error-free sensitivity of PAM-2 versus bitrate of 850nm, 980nm, and 1060nm VCSELs. 3-tap (dotted blue), 5-tap (dot-dash blue), 7-tap (dash blue), and 10-tap (solid blue) filters for 850nm VCSEL included.

rates to 60Gbps, Fig. 5.9, and then determine the maximum achievable data rate with equalization, Fig. 5.10. Drive voltage was kept constant across all VCSELs, but different for PAM-2 and PAM-4. All VCSELs were biased at 5mA for PAM-2 and PAM-4. The extinction ratio (ER) was measured to be 4dB, 5.8dB, and 5.7dB for the PAM-2 850nm, 980nm, and 1060nm links, respectively.

Without equalization, all VCSELs support up to 60Gbps error free BER10^{-12}, Fig. 5.9. Small differences in received powers at low bit rates result from differences in photodiode responsivity, ER, and relative intensity noise (RIN). The channel response is then equalized using frequency domain based gain equalization. The AWG is constrained into 3-tap, 5-tap, 7-tap, and 10-tap T-spaced time domain filtering [133]. Each tap configuration was tested at all wavelengths for error-free operation. In Fig. 5.9, only the

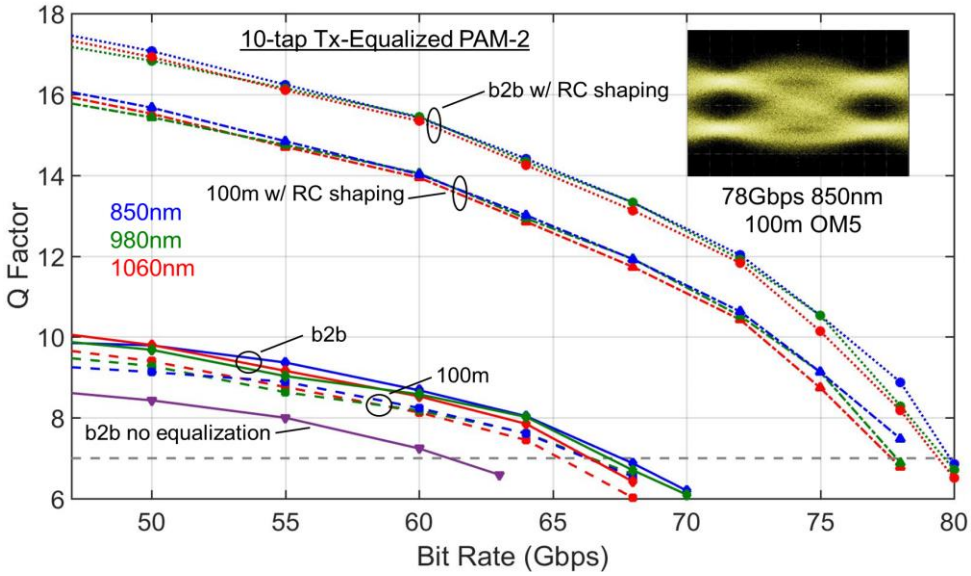

Fig. 5.10: Q factor vs. bit rate for equalized PAM-2 100m OM5 link using 850nm, 980nm, and 1060nm VCSELs. Purple line corresponds to the unequalized 850nm PAM-2 back to back (dark blue) link shown in Fig. 5.9.

equalization of the 850nm VCSEL is shown, but the benefits are similar for all VCSELs. We observe a decreasing benefit with increasing number of taps consistent with a channel memory of a few symbols. At 50Gbps the average received power can be reduced by nearly 2dB using equalization. Furthermore, the residual penalty at 50Gbps is only ~2dB compared to 25Gbps.

The maximum bit rate and the impact of pulse shaping is determined by assessing the Q factor: $Q = I_1 - I_0/(\sigma_1 + \sigma_0)$, (where the parameters have their usual meaning). For these measurements, Fig. 5.10, the average received optical power is fixed to 0dBm for all bit rates and a 10-tap equalizer is optimized separately for back to back and with 100m of OM5 fiber for each VCSEL. The back to back unequalized 850nm link is shown for reference in Fig. 5.10 (purple solid line) and the error free Q=7 is also indicated. The error-free data rate of each VCSEL extends beyond 65Gbps. Pulse shaping with a 9-tap RC filter with roll-off 0.35 is then added to the equalized links. Error-free data rates now increase to

>75Gbps for all wavelengths with the 850nm VCSEL reaching to 78Gbps PAM-2 over 100m OM5, nearly a 30% data rate increase from the unequalized back to back link. Interestingly, the pulse shaping improves the Q factor by >2dB across all bit rates yielding a 50Gbps response with negligible penalty compared to 25Gbps.

5.3.3 Receiver Equalization

The results presented in previous section relied solely on transmitter based filtering, in part to enable direct assessment of error rates. However receiver based signal optimization is a standard feature of optical receivers [112]. Implementing equalization at both the Tx and Rx reduces complexity and improves performance by distributing the filtering and by enabling a static equalizer at the transmitter and a dynamic filter at the receiver.

Various receiver DFE filters with transmitter-based equalization were investigated for PAM-4. Here we investigated sub-100Gbps data rates due to ADC limitations. Results for unshaped pulses at 72Gbps, Fig. 5.11, and RC pulse shaping for 84Gbps, Fig. 5.12,

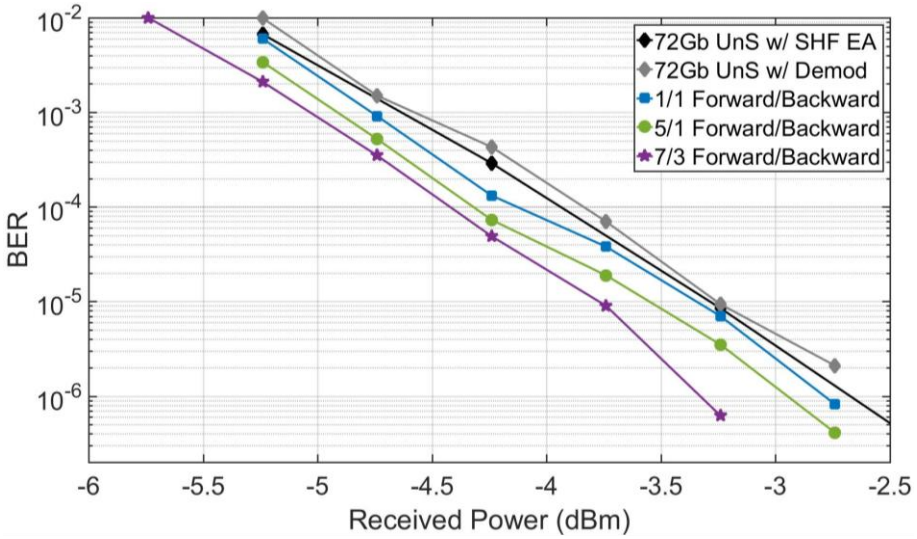

Fig. 5.11: Receiver tap combinations at 72Gbps PAM-4 on an equalized channel, using unshaped (UnS) pulses and PAM-4.

show the benefits of receiver DFE filters for the highest PAM-4 bit rates that achieved error-free performance. The results shown are for the 850nm VCSEL and are representative of all VCSEL wavelengths. We first compare the offline error counting method to the real-time error analyzer results and demonstrate consistency between these methods. The largest DFE filter examined, a 7/3 forward/backward tap configuration produced ~0.5dB reduction in the required received optical power for a BER >10-5. Fewer taps yield commensurately smaller benefits. The performance gains of receiver DFE filters for RC pulses is similar to, but slightly less than that observed for UnS pulses. This reduction in gain results in part from the tighter timing tolerance that accompanies RC pulse shaping.

There is a trend of higher receiver filter benefits at lower BER. At error rates of 10-6 both pulses experience a gain of approximately 0.75dB. Extrapolating to a BER of 10-12, a gain of at least 1dB for both UnS and RC pulses is expected.

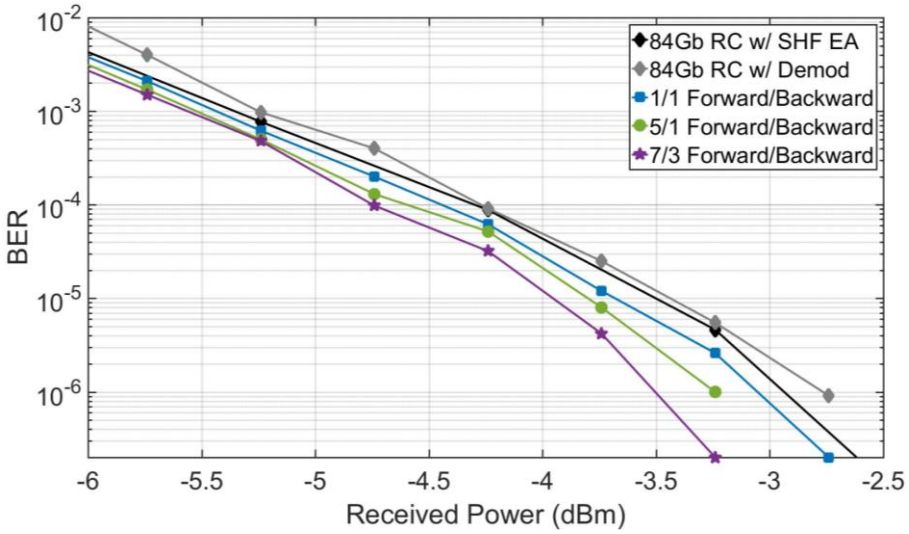

Fig. 5.12: Receiver tap combinations at 84Gbps on an equalized channel, using RC pulses and PAM-4.

5.3.4 Fiber Penalties

Fiber penalties including chromatic dispersion, differential mode delay and loss

will vary considerably from 850nm to 1060nm. We assess the total fiber penalty by comparing the required received power for error-free operation between back to back and with 100m OM5 with the equalization optimized for back to back. The VCSELs perform similarly for PAM-2 for the back to back with the 850nm VCSEL requiring >1.5dB lower power, Fig. 5.13. The 100m of OM5 adds only a modest penalty in all cases. For 50Gbps PAM-2 the fiber adds a total penalty of 1.5dB, 1.2dB, and 1dB to the 850nm, 980nm, and 1060nm links, respectively. For 100Gbps PAM-4, the fiber exhibits a power penalty of 2.2dB, 1.8dB, and 2.6dB to the 100Gbps PAM-4 850nm, 980nm, and 1060nm links, respectively. Thus OM5 fiber is readily able to support even the 200nm wide implementations of SWDM for both 50G PAM-2 and 100G PAM-4.

The total link penalty is decomposed into penalties associated with noise, dispersion, or nonlinearity. With reference to the Q factor, by measuring the minimum power required for a target BER with PAM-2 and PAM-4, I1, I0, ER, σ1, and σ0, with and without fiber, the individual power penalties for noise, dispersion and nonlinear PAM-4

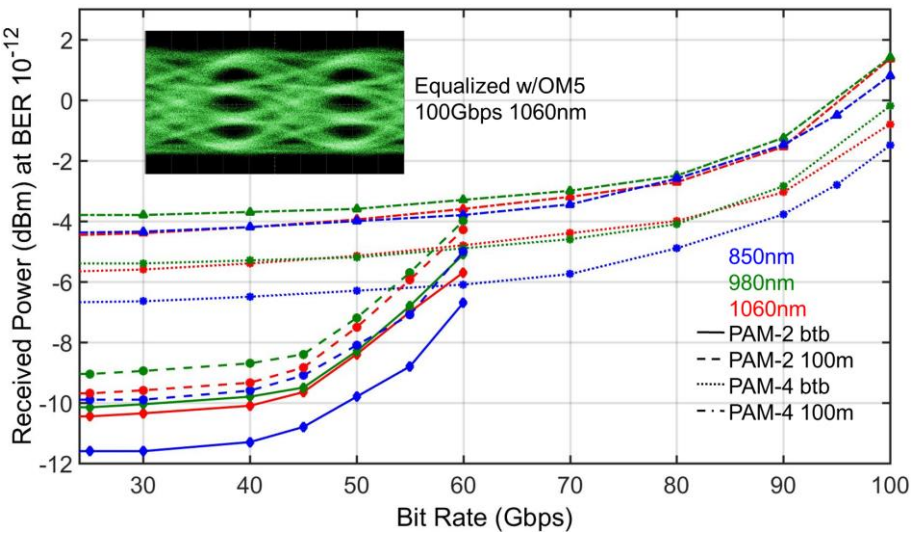

Fig. 5.13: Error-free received power for 850nm, 980nm, and 1060nm 10-tap equalized links using PAM-2 and PAM-4. Includes both back to back and 100m OM5.

effects can be isolated and quantified. Penalties from RIN, enhanced RIN, thermal, and equalizer noise addition are determined by measuring noise power and applying noise penalty equations derived in the IEEE Ethernet spreadsheet [85]. Dispersion penalties (chromatic, modal) are determined from differences in received power with and without the fiber. And, nonlinear penalties that arise from PAM-4 (eye skew, $ISI_{non\text{-}linear}$) are

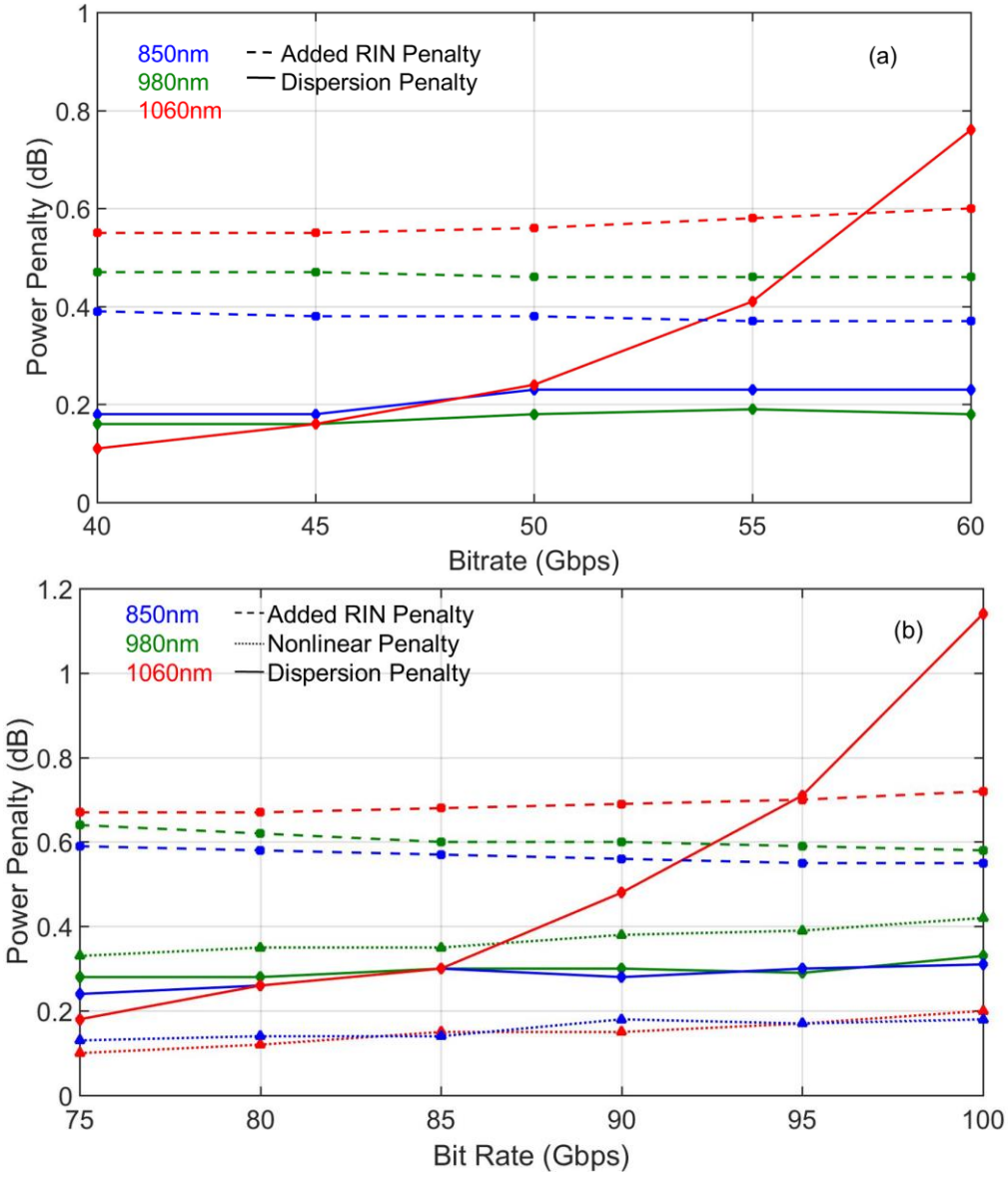

Fig. 5.14: Power penalty for error-free (a) PAM-2 and (b) PAM-4, over various bit rates for 850nm, 980nm, 1060nm 100m OM5 VCSEL links. Dispersion penalty notes by solid lines, fiber noise penalty noted by dashed lines, and nonlinear penalties noted by dotted lines in (b).

measured by comparing the BER of PAM-2, PAM-4, and the individual SER of each PAM-4 eye.

Several distinct penalties are depicted in Fig. 5.14. The primary observation is that the dispersion penalty is nearly constant with increasing bitrate for 850nm and 980nm while it increases with bitrate at 1060nm for both PAM-2, Fig 5.14a and PAM-4, Fig. 5.14b. Although the chromatic dispersion (CD) is greatest at 850nm, the DMD-CD interaction may be reducing the net dispersion penalty. The measured modal bandwidth for the fiber is ~5000MHz-km for both 850nm and 980nm, and ~2700MHz-km for 1060nm. Thus, the increase in dispersion penalty at 1060nm, where CD is lower, results from a decreasing modal bandwidth which is optimized for 850nm to ~950nm. The enhanced RIN penalty is fairly constant with wavelength, due to the offsetting effects between CD and DMD as well as the decreasing RMS spectra with increasing VCSEL wavelength.

In the case of the nonlinearity, all VCSELs have a similar penalty, with 980nm having slightly more, which slowly increases as the bit rate increases. The PAM-2 penalties (RIN and dispersion) are smaller than the PAM-4 penalties, resulting from the higher sensitivity of PAM-4 to amplitude distortions. For these VCSEL designs, nonlinear behavior is not a dominant impairment for PAM-4.

CHAPTER 6.

STATE-OF-THE-ART VCSEL COMMUNICATION

Future VCSEL deployments must continue to scale serial data rates to 100Gbps and beyond while retaining energy-efficiency and cost effectiveness. For applications such as high performance computing (HPC), forward error correction (FEC) adds substantial latencies making them impractical for many short reach links [136]. Thus, VCSEL-MMF links have been restricted to PAM-2 modulation formats, as PAM-4 has been standardized to include FEC. We demonstrated a path to 100Gbps data rates using 21GHz production VCSELs in previous Chapters. However, as VCSEL and receiver bandwidths increase, it is now possible to increase data rates for VCSEL-MMF links further.

In this Chapter, we overview the changes in VCSEL fiber optic communication technology over the last few years that have enabled data rates to continue increasing. We

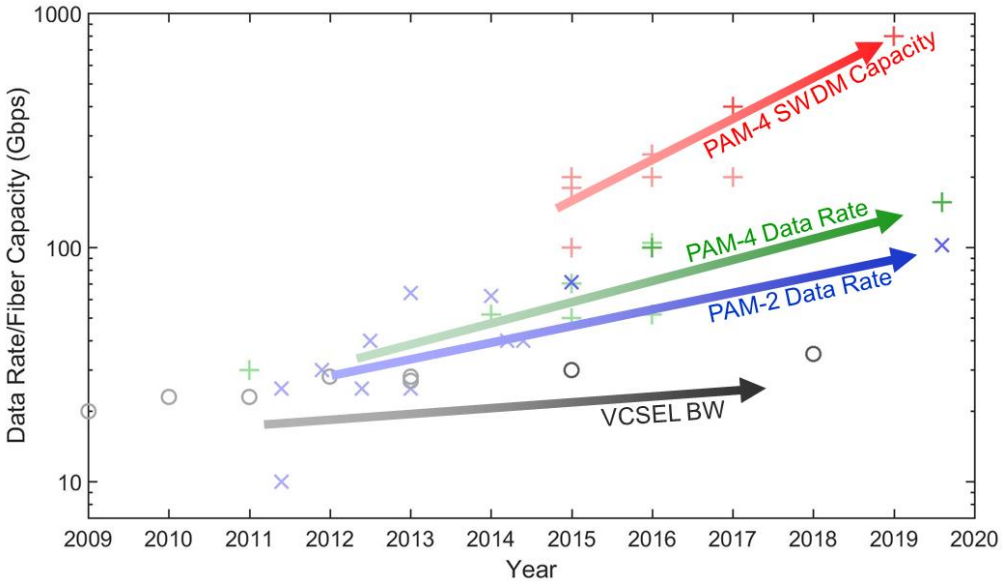

Fig. 6.1: SWDM capacity, data rate, and bandwidth growth over the last decade.

then present our most recent work with both single mode and multimode VCSEL setting record data rates and data rate distance products over fiber.

6.1 Advances in Error-Free Transmission for >100Gbps PAM-4

In this section, we overview the maximum achievable error-free (BER $<10^{-12}$) data rates and the penalties for standard 50Gbps and 100Gbps links for PAM-2 and PAM-4 using both commercially produced and research grade VCSELs. We show that VCSEL/MMF links are significantly improved with simple equalization and pulse shaping implemented exclusively at the transmitter. Current production VCSELs, used for existing 25Gbps transceivers, support up to 100Gbps using PAM-4 with FEC and research grade VCSELs enable error-free rates well beyond 100Gbps using PAM-4. We show that these benefits originate substantially due to the slow roll-off of VCSEL responses when strongly biased but also due to higher available power and low relative intensity noise (RIN). This performance is achieved with short wave division multiplexing (SWDM) capable fiber; LaserWave FLEX WideBand Multimode Fiber (OM5) which readily supports 50Gbaud beyond 100m.

6.1.1 Experimental Setup

VCSELs suitable for IEEE standard 802.3bm (25Gpbs PAM-2) were provided by Finisar. This design is in volume production and previously described [119]. The relative intensity noise (RIN) was ~-142dB/Hz with an oxide aperture of ~8μm and an RMS spectral width of 0.493nm. Next generation VCSELs used in this study were 3rd generation VCSELs designed and fabricated at Chalmers University. These 850nm VCSELs were

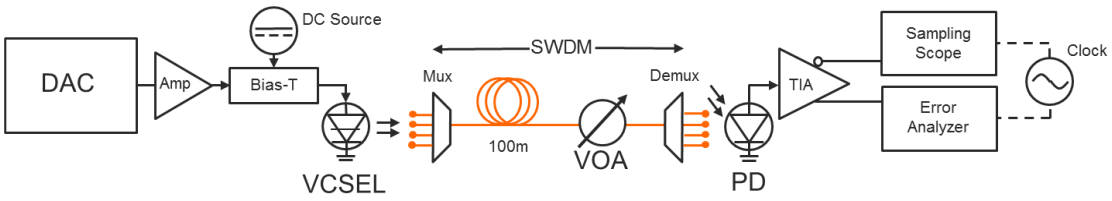

Fig. 6.2: Experimental SWDM link with MUX and deMUX. The "channel" starts at the DAC and ends at the digitizer. The total link loss is 2.4dB.

designed for high-speed modulation using strained InGaAs quantum wells, a λ/2 optical cavity, and multiple oxide apertures [120]. The reflectivity of the top mirror was adjusted to optimize a flat and high-bandwidth modulation response [120]. The optimum mirror reflectivity can be designed into the epitaxial layer growth and the fabrication process is otherwise conventional. Thus these VCSELs represent a target for high volume production. VCSELs with 5μm, 7μm, 9μm and 11μm aperture sizes were studied, each had a bandwidth of ~25GHz and RIN between -145dB/Hz to -153dB/Hz depending on aperture. The RMS spectral widths are 0.69nm, 0.76nm, 0.86nm, 0.94nm from smallest to largest aperture.

The electrical drive signals were generated using a Keysight Arbitrary Waveform Generator (AWG) with 32GHz of analog bandwidth. The signals were amplified with a SHF 827 linear amplifier and applied to unpackaged VCSELs using an RF probe, Fig. 6.2. All VCSELs were biased and electrically driven for optimum performance. Extinction ratios (ER) for 7μm, 9μm and 11μm aperture Chalmers VCSELs were ~8dB. The Finisar VCSEL and the Chalmers 5μm aperture VCSEL had a ~6dB ER. A PRBS-15 pattern was used for all testing and the PAM-4 patterns were implemented with gray coding. The OM5 fiber is similar to [132] and exceeds the proposed OM5 TIA specification of 4700MHz-km at 850nm. The setup includes a CWDM MUX and deMUX to emulate a SWDM link, resulting in a total insertion loss of 2.4dB for 100m of fiber.

The receiver consists of an InGaAs photodiode with 20μm aperture and a low noise Inphi TIA with a combined electrical bandwidth of 29GHz. The responsivity was ~0.34A/W at 850nm. In section 6.1.4, the receiver was exchanged with a Thor Labs DXM30BF photodiode with 33GHz bandwidth and 0.48A/W responsivity at 850nm connected to a SHF 807 amplifier. The received signal is direct detected and analyzed by a DCA 81600D sampling scope, SHF 11100A Error Analyzer (EA), and Keysight M8040A EA to capture eye diagrams and determine bit error rates.

6.1.2 Commercial Production VCSELs

Commercial production VCSELs are currently manufactured targeting 25Gbps PAM-2 links. The 3dB bandwidths of these VCSELs are ~20GHz. The channel response with this production VCSEL had a 3dB bandwidth of ~19GHz, Fig. 2. When equalizing, the channel response roll-off, the choice of equalizer length, optical power, extinction ratio, baud rate and RIN all contribute to the optimum equalized 3dB bandwidth.

Experimentally, links are equalized using a 10-tap frequency-domain equalizer. However, an equivalent equalizer can be implemented with a conventional time-domain 10-tap FIR filter, Fig 6.3. The number of taps are limited to ensure a high-bandwidth power efficient filter is feasible. The optimum equalized 3dB bandwidth was determined by maximizing link data rates for each VCSEL. As a result, the filter may not be optimum for low baud rates and the observed received power is slightly higher than that possible with a filter optimized for low baud rates. We also evaluate the impact of an additional 9-tap raised cosine (RC) pulse shape filter to reduce spectral occupancy, thereby limiting the impact of dispersion [133].

We quantify the performance of PAM-2 and PAM-4 formats by the received power required for error-free operation for various data rates. The equalized channel bandwidth was 24GHz corresponding to a peak equalizer gain of ~11dB and demonstrating the

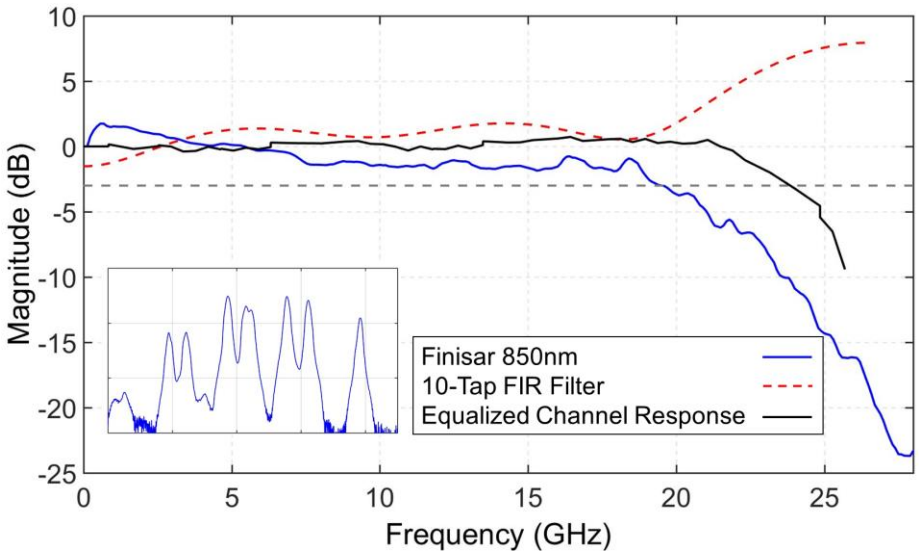

Fig. 6.3: Measured channel response of Fig. 1 with production VCSEL and corresponding 10-tap FIR equalization filter response optimized for a 24GHz 3 dB bandwidth (red dotted). Optical spectra in inset.

significance of the unequalized 15dB channel bandwidth. The production VCSELs achieve maximum error-free PAM-2 data rates of 54Gbps and 44Gbps with and without pulse shaping respectively, Fig. 6.4. Implementing PAM-4 with the production VCSEL extends maximum error-free data rates to 84Gbps and 72Gbps with and without pulse shaping respectively, Fig. 6.4.

For many applications it is more instructive to examine the performance corresponding to specified data rates compared to btb. Using the error-free equalized PAM-2 link as reference, Fig. 6.4 shows pulse shaping of PAM-2 allows 50Gbps with a 5dB penalty and a ~4dB power margin. Pulse-shaped and equalized PAM-4 supports 50Gbps with similar required optical power. Modest pulse shaping of PAM-4 allows >75Gbps with

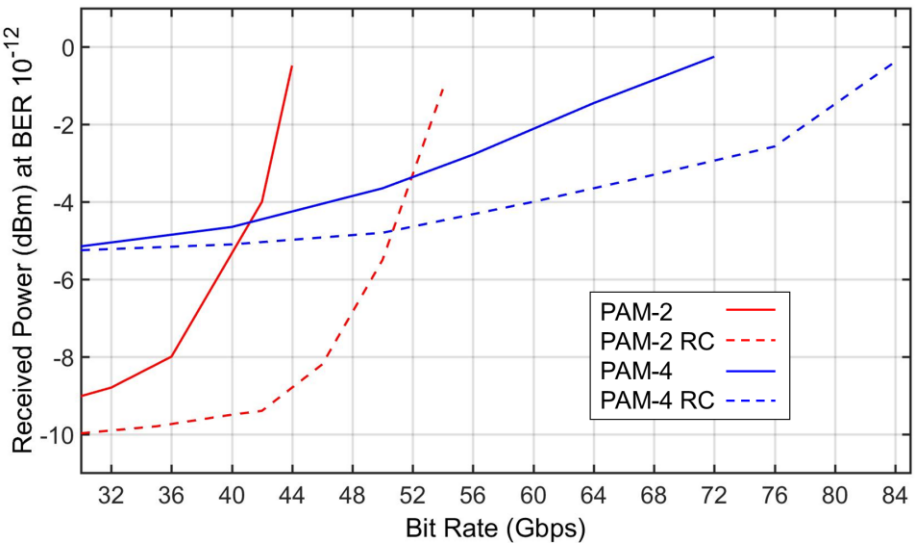

Fig. 6.4: Required received power for error-free transmission with PAM-2 and PAM-4 on an equalized channel with 100m OM5 fiber using Finisar production VCSELs. Solid lines: no pulse shaping; Dashed line: raised cosine (RC) pulse shaping.

a 7dB penalty and a similar ~3dB power margin. This demonstrates the performance advantages attainable using transmit only filters with 25Gbps production VCSELs.

6.1.3 Research Grade VCSELs

The Chalmers VCSELs yield an unequalized 3dB channel bandwidth of 21.5GHz for 11μm oxide aperture and 22.5GHz for the other apertures, Fig. 6.5. These research grade VCSELs, each exhibit 2.5GHz more channel bandwidth compared to production VCSELs, an increased OMA, and fiber coupled power up to 18mW for the 11μm oxide aperture. Each VCSEL was biased with a near equal current density of ~0.15 mA/μm2. The corresponding mode structures are shown as insets in Fig 6.5. These research VCSELs were able to be equalized to a 3dB bandwidth of 28GHz due to their increased bandwidth, lower RIN, improved optical power, and higher extinction ratio.

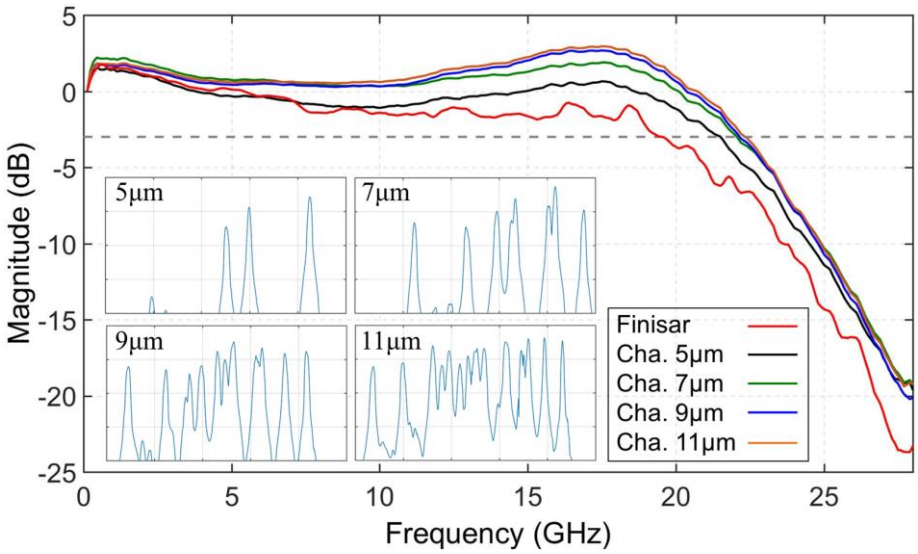

Fig. 6.5: Measured channel response of research grade Chalmers VCSELs with optical spectra for 5µm, 7µm, 9µm, and 11µm apertures, the production VCSEL response is also shown.

The 7µm VCSEL supports maximum PAM-2 data rates of 68Gbps and 62Gbps with and without pulse shaping respectively, Fig. 6.6a. This represents a 30% increase over production VCSELs. The 9µm and 11µm aperture VCSELs performed nearly identical to the 7µm VCSEL. Most notably, the research grade VCSELs readily support error-free 50Gbps PAM-2 with only transmit equalization and no pulse shaping, an important data rate benchmark. Furthermore, these VCSELs support 50Gbps with only a 2dB penalty compared to back to back when using both equalization and pulse shaping.

When examining PAM-4, the research grade VCSELs achieve error-free data rates of 100Gbps and 90Gbps with and without pulse shaping, Fig. 6.6a, which is the first report of 100Gbps PAM-4 error-free rates. The maximum achievable error-free data rate for PAM-4 was 110Gbps.

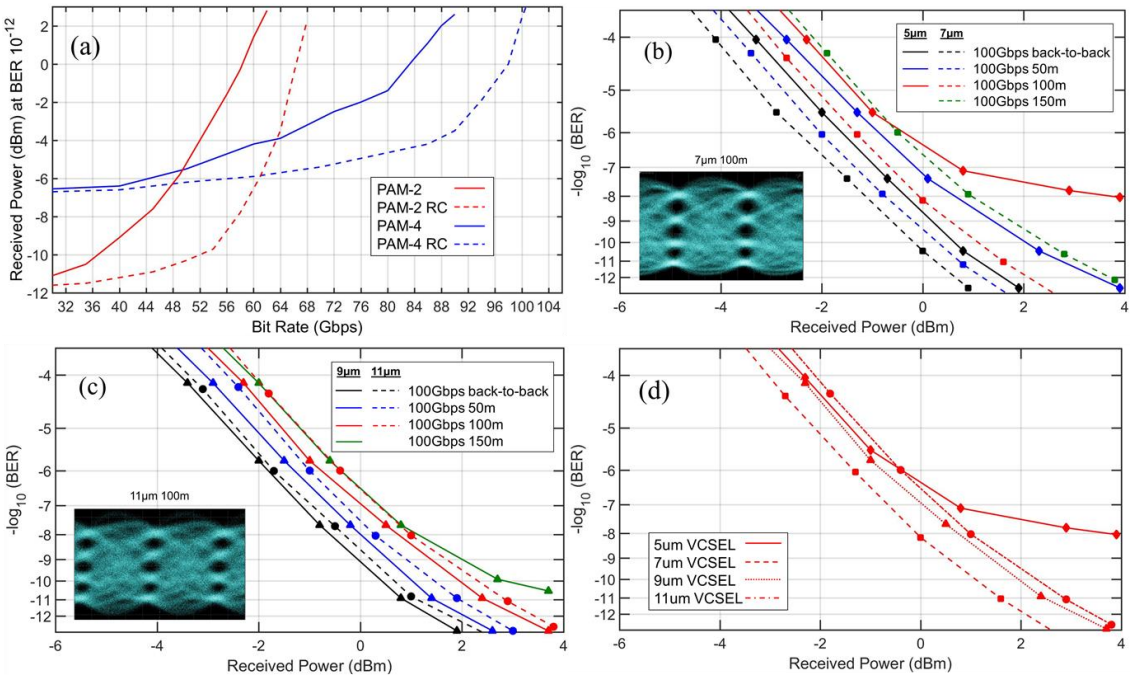

Fig. 6.6: (a) Required received power for error-free transmission with PAM-2 and PAM-4 on an equalized channel with 100m OM5 fiber using 7µm Chalmers VCSELs. Solid lines: no pulse shaping; Dashed line: raised cosine (RC) pulse shaping; (b) PAM-4 BER performance for 5µm and 7µm; (c) PAM-4 BER performance for 9µm and 11µm; (d) PAM-4 BER performance over 100m for all apertures. All results achieved with transmitter only equalization.

Focusing on PAM-4 100Gbps data rates, we examine performance versus aperture and fiber reach, Figs. 6.6b, and 6.6c. Performance versus aperture varies due to the specific RIN, power, and optical spectral characteristics. Typically, VCSELs with more mode sets experience a smaller RIN enhancement due to fiber dispersion and associated decorrelation of modes (section 3.2). We observed a RIN enhancement (worsening) of 5dB/Hz, 3dB/Hz, 2dB/Hz and 2dB/Hz for the 5µm, 7µm, 9µm, and 11µm VCSELs, respectively after 100m of fiber.

The 7µm and 9µm VCSELs performed best due to their low RIN and RIN enhancement. Error-free 100Gbps PAM-4 was achieved at 150m using the 7µm VCSEL, and 100m with the 9µm VCSEL, Fig. 6.6b and 6.6c. Generally, the fiber penalties are small,

~1-1.5dB at 100m. However, a noise floor associated with RIN enhancement was observed with the 5μm VCSEL limiting error-free performance to 50m.

The 100m performance of each research grade VCSEL is shown together, Fig. 6.6d. The 7μm VCSEL performs best, with the 5μm VCSEL performing the worst. The 7μm, 9μm, and 11μm VCSEL all reach error-free data rates at similar received power. For the 7μm, 9μm, and 11μm VCSELs, the OM5 fiber imposes a penalty of approximately 2dB over 100m. Also, there is no indication of a significant BER floor for VCSELs at 100m other than the 5μm aperture. Thus, the most important factor to enabling 100Gbps data rates is increasing VCSEL bandwidth while simultaneously maintaining low RIN and sufficient fiber coupled power.

6.1.4 Comparison of Channel Bandwidths

At the higher data rates, the bandwidth limitation of the receiver notably impacts link performance. Receivers with MMF input present significant challenges balancing collection efficiency with speed. We investigated link performance using a receiver with a different frequency response, specifically a Thor Labs photodiode and SHF amplifier, Fig. 6.7a. Although the 3dB bandwidth is slightly worse, roll off is slower resulting in higher 10dB and 15dB bandwidths. As a result, the equalized 3dB bandwidth is >33GHz.

Three link configurations are considered, Fig. 6.7b: Finisar VCSEL (red) with 3dB equalized bandwidth of 24GHz, Chalmers VCSEL (blue) with 3dB equalized bandwidth of 28GHz, and the Chalmers VCSEL with Thor receiver (black) with 3dB equalized bandwidth of 33GHz. The additional 5GHz channel bandwidth reduces the PAM-4 penalty by ~7dB at 100Gbps yielding a penalty of <2dB compared to PAM-4 back to back with a

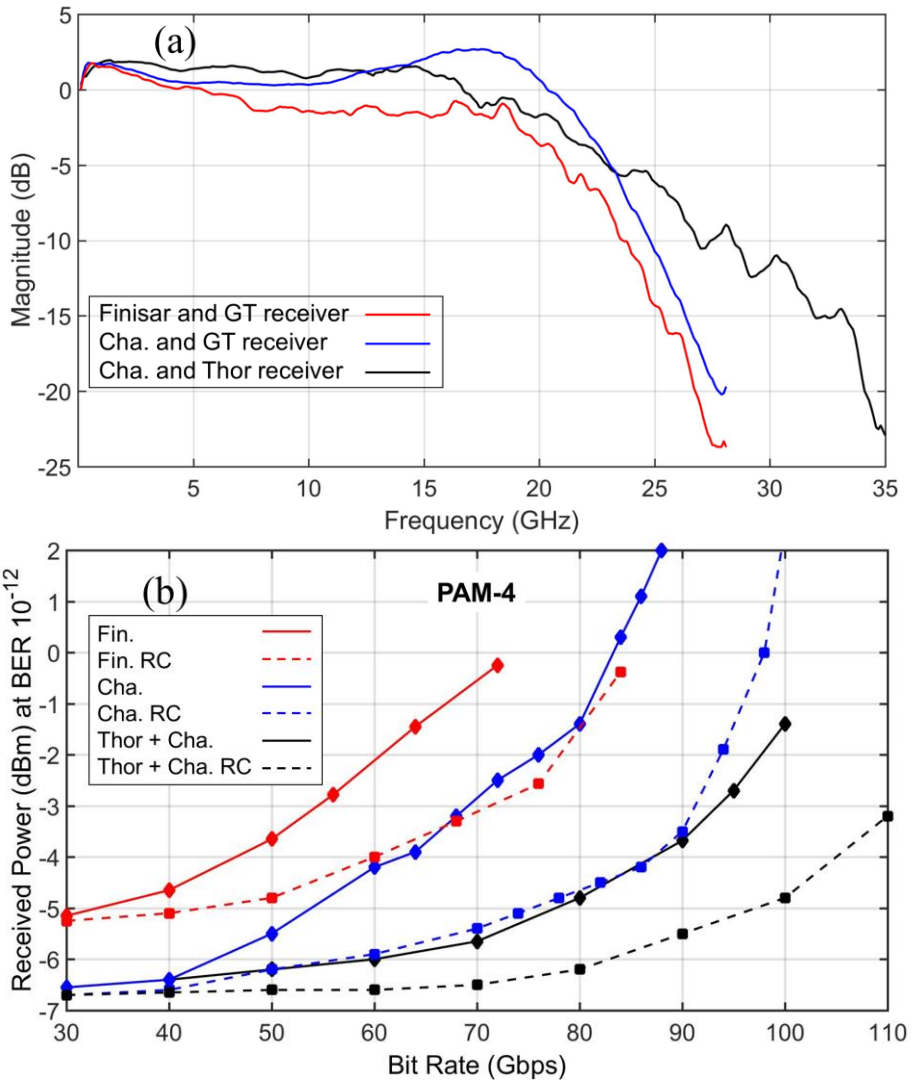

Fig. 6.7: (a) Previous measured channel response of Fig. 2 and Fig. 5a compared to improved receiver (black); (b) Comparison of required received power for error-free (BER 10^{-12}) PAM-4 transmission on an equalized channel with 100m OM5 fiber. Solid lines represent no pulse shaping and a dashed line represents raised cosine (RC) pulse shaping.

~8dB margin when implementing equalization and pulse shaping. Without shaping, 100Gbps is achieved with a 5dB penalty. Similar benefits are found for the commercial VCSEL which now supports a maximum bit rate of >80Gbps and negligible penalty at 50Gbps compared to PAM-4 back to back (the PAM-2 link also shows negligible penalty with the new receiver compared to PAM-2 back to back). We conclude that error-free

100Gbps (50GBaud PAM-4) can be achieved with 25GHz VCSELs and receivers that enable 30GHz equalized channel.

6.2 104Gbps NRZ over 50m OM5 MMF

To sustain capacity growth continued effort is needed to increase core data rates while retaining the power efficiency advantages of VCSEL-MMF links. The new inclusion of equalization and forward error correction (FEC) into VCSEL-MMF links show potential for extending link capabilities [117, 133]. Furthermore, there are a number of foundries producing CMOS components suitable for filters and amplifiers needed to deploy these high speed links. For example, GLOBALFOUNDRIES 45SPCLO CMOS process exhibits an f_T of 280GHz and supports 100Gbps NRZ TIAs [137].

In this section, we demonstrate, for the first time, >100Gbps PAM-2 NRZ signaling using 850nm VCSELs through OM5 multimode fiber. Equalization is employed using a transmitter based static equalizer and receiver based adaptive equalizer. Furthermore, a raised cosine (RC) pulse shape was implemented to minimize bandwidth limited impairments. Specifically, we demonstrate 102Gbps PAM-2 with BER below FEC threshold through 50m of OM5 fiber. We also demonstrate error-free data rates of 84Gbps over 100m OM5 and 90Gbps over 50m OM5. This is the fastest reported error-free PAM-2 direct modulation data rate for any laser to date and the first VCSEL-MMF transmission eclipsing 100Gbps using traditional NRZ signaling.

6.2.1 Experimental Setup

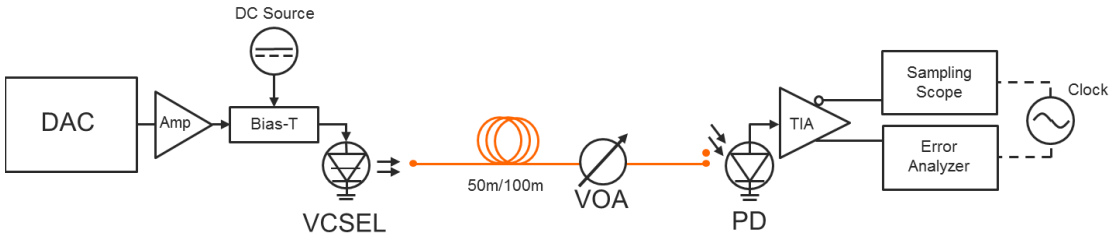

Fig. 6.8: Experimental Setup for PAM-2.

The electrical PAM-2 signal was created with a Keysight M8194A AWG. The channel response, from the DAC output to the real time scope, is depicted in Fig. 6.8 for the native and equalized channel. Equalization was constrained to the equivalent of 10 taps to ensure fabrication is feasible in current technologies. VCSELs used in this study were unpackaged 3rd generation VCSELs designed and fabricated at Chalmers University for 50G NRZ operation. The VCSELs had an aperture of 5μm, 26GHz 3dB bandwidth, and RIN <-150dB/Hz. OFS OM5 MMF with ≥5GHz-km effective modal bandwidth at 850nm was used for the transmission experiments.

The receiver was a Thor Labs DXM30BF photodiode with 33GHz bandwidth and 0.48A/W responsivity at 850nm connected to a SHF 807 amplifier. The received signal was captured using the real-time Keysight UXR1102A oscilloscope. The filter at the receiver was applied through the UXR and compensates for remaining channel distortions. Again, the filter was limited to 5 taps. Direct bit error rate counting was done using the SHF 11100A error analyzer for rates ≤60Gbps. Probability density function (PDF) analysis was implemented for data rates >60Gbps. The methods were shown to be equivalent for rates up to 60Gbps. We determined the maximum error-free rates achievable with and without pulse shaping. Additionally, we determined the rates achievable when low latency Reed-Solomon (544, 514, 15, 10) KP4 FEC is to be employed. Specifically when we achieve an uncorrected BER of $2 \cdot 10^{-4}$.

6.2.2 Equalization

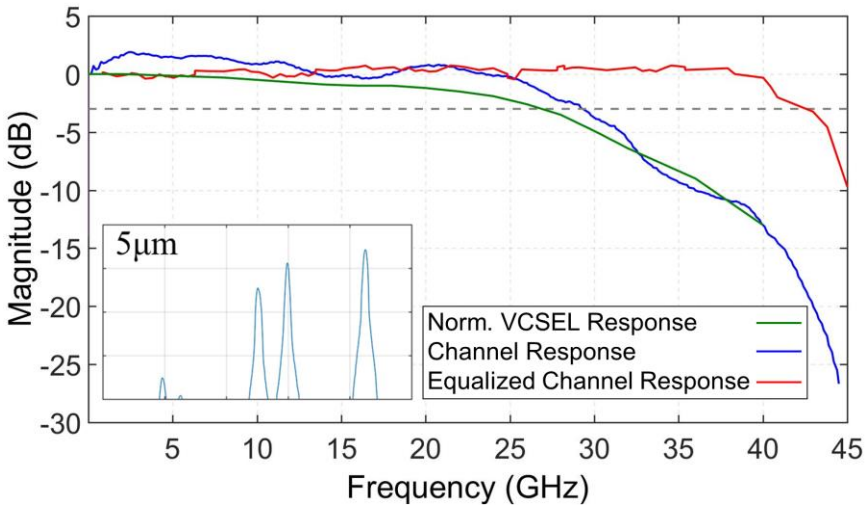

Fig. 6.9: Normalized VCSEL response, channel response, equalized channel response and 850nm optical spectrum.

The VCSEL-MMF channel response is primarily governed by the VCSEL and receiver responses, Fig. 6.9. Here, the steep channel response roll-off beyond 40GHz is due to the receiver bandwidth. The low RIN, and high fiber-coupled power allow the noise limited equalization to provide >10dB net gain boost. Thus, due to the slow channel response roll-off, linear equalization can effectively increase the channel bandwidth of VCSEL-MMF links by over 50%, Fig. 6.9. As a result, modest linear equalization proves to significantly increase the data rate. We note also the low modal dispersion of the fiber ensures the RIN is not significantly worsened due to mode decorrelation. At the receiver, we applied a 5-tap FFE filter optimized for each bit rate through the software of the UXR1102A. Additionally, a 9-tap RC pulse shape filter was applied at the transmitter with 0.3 roll-off to reduce spectral occupancy. We note that improvements in the receiver bandwidth will allow equalization to larger channel bandwidths.

6.2.3 Results

The VCSELs were biased at 4.0mA, yielding a RMS spectral width of ~0.49nm and ~3dBm of fiber coupled power. Fiber coupling via a lensed fiber was optimized for

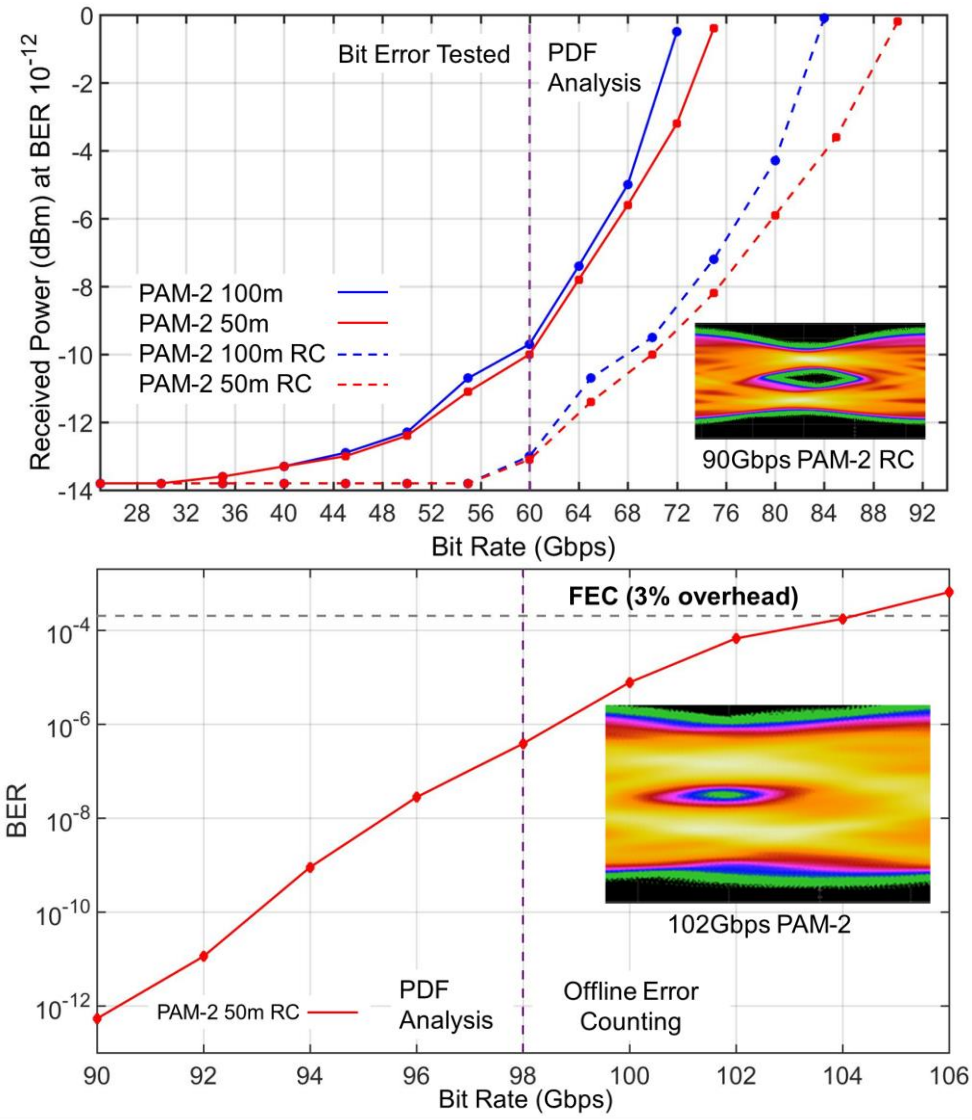

Fig. 6.10: (a) Received power for error-free transmission with PAM-2 on an equalized channel through 50m (red) and 100m (blue) OM5 fiber. Pulse shaping was added to the equalization to increase data rates (dashed); (b) Bit error rate (BER) of RC PAM-2 through 50m OM5 fiber. FEC limit marked by gray dashed line.

best receiver sensitivity. The BER PDF analysis (beyond 60Gbps) was done over $>1 \cdot 10^7$ (oversampled) symbols and did not show signs of any noise floor for all rates examined.

The VCSELs were first tested for their error-free rates with only linear equalization

applied. 72Gbps was achieved through 100m of fiber and 75Gbps was achieved through 50m of fiber, Fig. 6.10a. Furthermore, there was only a small increase in penalty for 100m compared to 50m at rates beyond 70Gbps. Both fiber lengths experienced minor power penalty increase until 60Gbps.

The RC filter was applied to compare maximum achievable data rates under the same conditions. At 0dBm, the error-free data rate increases by 12Gbps over 100m of fiber and 15Gbps over 50m of fiber, to 84Gbps and 90Gbps, respectively. Using linear equalization with RC filters, there is nearly no power penalty until 60Gbps. Beyond 90Gbps and over 50m of OM5, data rates were no longer error-free by PDF analysis, Fig. 6.10b. The BER steadily increased with data rate, rolling off at BERs $>1 \cdot 10^{-6}$. At 98Gbps, sufficient waveforms could be collected to count symbol errors offline with confidence. We counted an error rate of $1.02 \cdot 10^{-4}$ at 104Gbps PAM-2 over 50m OM5, sufficiently below the KP4 FEC limit for error-free performance. Based on data rate improvements from equalization, we estimate that a receiver bandwidth improvement of 20% will produce near error-free 100Gbps PAM-2. No burst errors were found in the waveforms analyzed, demonstrating the ability of VCSEL-MMF links to continue capacity growth.

6.3 168Gbps PAM-4 over 50m OM5 MMF

Increase in data center infrastructure to support growing cloud services has led to growing demand for energy-efficient, high-speed data links for server-to-server and server-to-rack interconnects. These links are dominated by Vertical-Cavity Surface Emitting Lasers (VCSELs) and multimode fiber (MMF) due to their excellent performance, low cost, low power, and high density form factor. The IEEE 802.3cm standard efforts support

50Gbps PAM-4 core rates in four (two lambda) and eight fiber configurations to support traffic up to 400Gbps. To continue extending data rate capacity, both faster data rates and increases in shortwave division multiplexing (SWDM) lambda will be required. Experimental VCSEL links have demonstrated 102Gbps OOK over 50m OM5 MMF, a 120Gbps PAM-4 Transceiver [138], and SWDM VCSEL links for 800Gbps/1.6Tbps solutions. The inclusion of equalization at the transmitter and receiver, as well as low-latency KP4 forward error correction (FEC) acceptance in IEEE standards, have allowed VCSEL MMF links to scale data rates competitively with silicon photonics and short reach coherent solutions while continuing to offer the most efficient bitrate in regards to cost and power consumption.

In this section, we demonstrate greater than 160Gbps PAM-4 signaling over 50m of OM5 MMF, using 850nm unpackaged VCSELs with allocation for FEC. Equalization is implemented at the transmitter as pre-emphasis and receiver as a static feed-forward equalizer (FFE). Additionally, we include raised cosine (RC) filtering to demonstrate the benefits of shaping the electric signal for a typical equalized VCSEL link channel. We study the maximum achievable error-free (BER $<10^{-12}$) data rates for PAM-4 and reach 146Gbps over 50m of OM5. We conclusively show VCSELs are capable of reaching over 160Gbps PAM-4, demonstrating the continued capability of VCSEL MMF links to scale line rates with demand.

6.*3.1* *Experimental Setup*

In this section, we study the performance of a new generation of anti-waveguiding VCSELs with increased bandwidth above 28GHz [139]. It was previously shown that this

generation of oxide-confined VCSELs operates at 60Gbps without pre-emphasis or signal processing in PAM-2 modulation and is expected to enable higher bit-rates if operated in combination with specialized electronics [140].

The VCSELs were driven by a 120GSa/s Arbitrary Waveform Generator (AWG) with 45GHz of analog bandwidth (Keysight Technologies M8194) with a PRBS-15 pattern. Details of the setup are shown in the figure in section 6.2.1. The VCSELs that were investigated had ~28GHz bandwidth. A peak-to-peak voltage swing of 650mV was used to drive each VCSEL with a DC bias of ~4mA. Details of the experiment are similar to our previous work [133] with a few alterations. In the case of investigating shaped pulses, a 9-tap T/2 spaced time-domain raised cosine (RC) filter with 0.35 roll off factor was used. The transmitter pre-emphasis was generated by the AWG in a limited form, by restricting the DAC to a 6-tap filter. The filter at the receiver was applied through a real-time Keysight UXR1102A oscilloscope and compensates for remaining channel distortions using a static

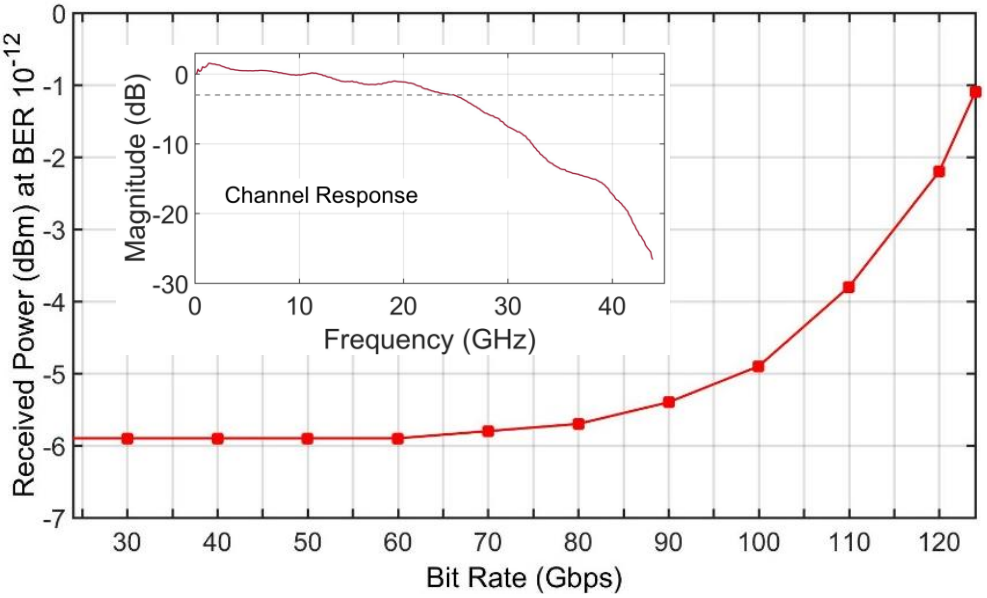

Fig. 6.11: Received power for error-free transmission with PAM-4 on an equalized channel through 100m (red) OM5 fiber with VCSEL channel response (inset).

5-tap FFE based on the baud rate. The optical signal was attenuated by 3dB to emulate the loss from a MUX/deMUX. The OM5 MMF was supplied by OFS. A Thor Labs DXM30BF Ultrafast Detector was used with an SHF 807 amplifier for the receiver. Direct bit error rate counting was done using the SHF 11100A error analyzer (BERT) for rates ≤120Gbps. For PAM-4, the error rate is evaluated by measuring the symbol error rate of each eye at identical sampling points, and then summing half the individual eye error rates. Probability density function (PDF) analysis was implemented for data rates >120Gbps using the real-time UXR. The BERT and PDF method was shown to be close to equivalent for rates up to 120Gbps. The BER PDF analysis was done over $>1 \cdot 10^{7}$ (oversampled) symbols. When the BER was $>10^{-6}$, offline error counting was done through the real-time scope.

6.3.2 *Transmitter Equalization and Error-Free PAM-4*

In order to keep equalization simple for analog implementation, a static UI-spaced 6-tap FFE filter response was applied based on the channel response, Fig. 6.11 inset. With regards to equalization, the channel response roll-off, the choice of filter length, optical power, extinction ratio, baud rate and RIN all contribute to the optimum equalized 3dB bandwidth. For experimental simplicity, we determined the optimum equalized 3dB bandwidth by maximizing link data rates for the VCSEL, which was >40GHz. As a result, the filter may not be optimum for low baud rates and the observed received power is slightly higher than that possible with a filter optimized for low baud rates.

The minimum optical power to achieve error-free PAM-4 through 100m OM5 fiber was experimentally measured by sweeping the bit rate to just beyond 120Gbps, Fig. 6.11. The minimum received power is consistent at ~-6dBm to 80Gbps, limited by the thermal

noise and responsivity of the receiver. Beyond 80Gbps, the residual ISI from the channel and nonlinearities of the PAM-4 eyes begin to exponentially increase the power penalty as the bitrate increases. Regardless, at 100Gbps the power penalty increase is less than 1dB, demonstrating that 100Gbps PAM-4 over 100m is achievable with a 6-tap FFE transmitter equalizer. As the data rate increase to 120Gbps, the power penalty increases to 3.6dB, still having some power margin. Beyond 120Gbps, PDF analysis was used to calculate the BER and the power penalty begins to increase >1dB for every 3Gbps improvement.

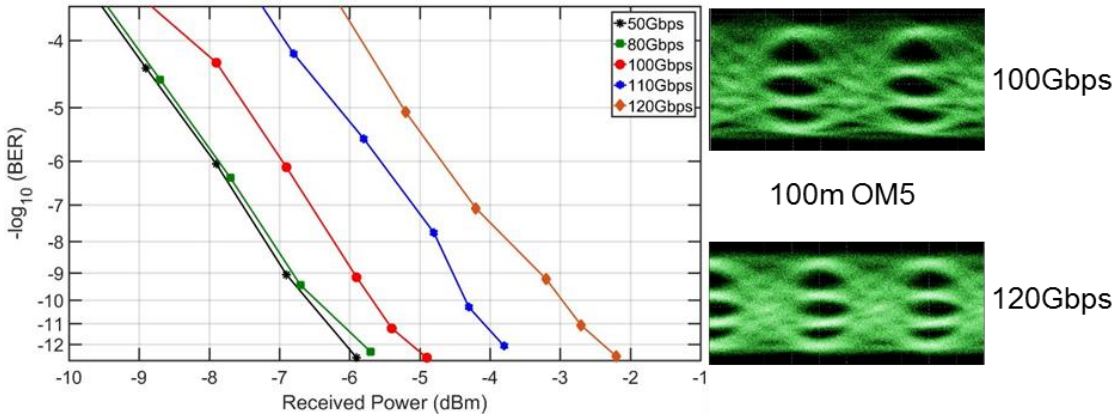

Fig. 6.12: BER vs. received power for PAM-4 for various bit rates on an equalized channel through 100m OM5 fiber; Eye diagrams (right) for equalized error-free 100Gbps and 120Gbps PAM-4 through 100m OM5 fiber.

Several BER curves were taken below 120Gbps for comparison, Fig. 6.12. No noise floor can be seen in any of the BER curves. At 50Gbps and 80Gbps, PAM-4 exhibits nearly the same shape. At 100Gbps and above, the BER curves have slightly varying shapes due to the non-optimal equalization resulting in some eye nonlinearity which be seen in the eyes, Fig. 6.12 (right). Note at 120Gbps there is less nonlinearity than at 100Gbps. Re-optimizing the equalization for a 100Gbps will significantly reduce the nonlinearity without the need for a Volterra filter.

6.3.3 RC Filtering, Receiver Equalization, and FEC with PAM-4

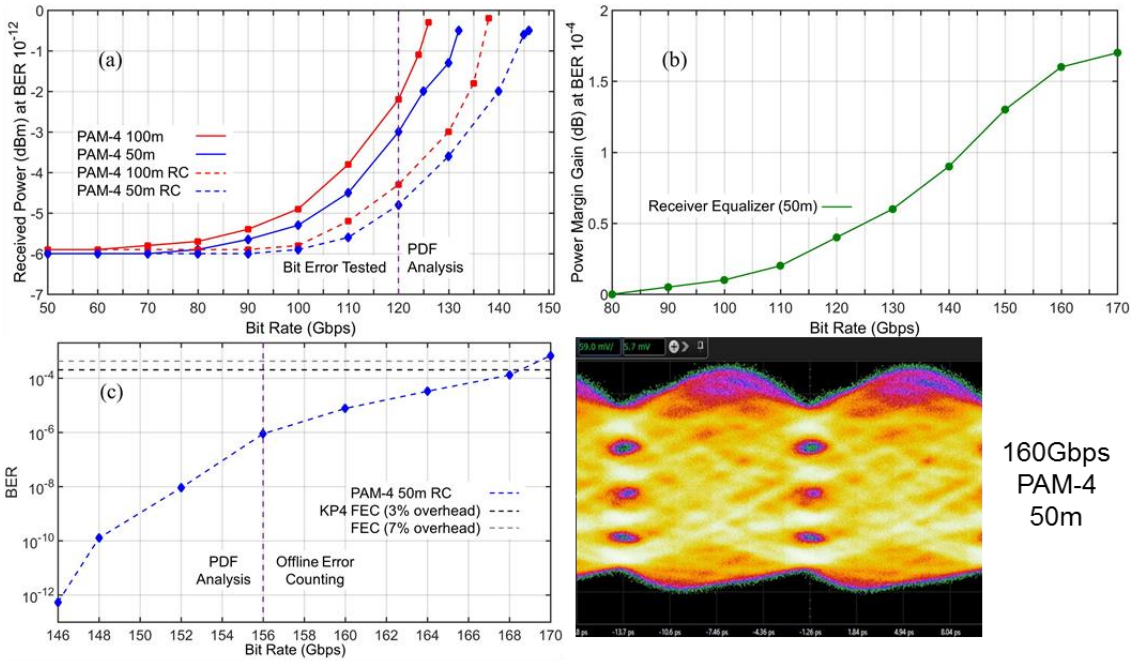

Fig. 6.13: (a) Received power for error-free transmission with PAM-4 on an equalized channel through 100m (red) and 50m (blue) OM5 fiber. Pulse shaping was added to the equalization to increase data rates (dashed); (b) Receiver equalizer power margin gain over 50m OM5 at 10^{-6} BER; (c) Bit error rate (BER) of RC PAM-4 through 50m OM5 fiber. FEC limit marked by black (3%) and gray (7%) dashed line; (bottom right) PAM-4 eye diagram at 160Gbps before receiver equalization.

An RC filter, as described in the experimental setup, is added for deliberate shaping of the drive signal to match the equalized channel and thereby reduce ISI. Through 100m OM5, the RC filter improves the bit rate by 12Gbps. The RC filter improves the bitrate by 15Gbps through 50m OM5, to an error-free 146Gbps. At high bit rates, the performance through 50m OM5 becomes significantly better than 100m due to dispersion effects. Compared to the maximum achievable error-free bitrates through 100m OM5, 50m OM5 provides 1.8dB and 2dB of extra power margin for non-filtered and RC filtered pulses, respectively. Considering the 100m OM5 has only ~0.1dB more loss than 50m OM5, this was a substantial reduction in the dispersion power penalty.

To extend the data rate, FEC and a receiver equalizer were added to the system. The static 5-tap T-spaced receiver equalizer consisted of 1 pre- and 3 post-taps and was

optimized for each bit rate, while overhead was allocated for the well-accepted KP4 FEC. We note that over the $>10^7$ symbols analyzed, no burst errors were found. The receiver equalizer steadily improved optical power margin to a 1.7dB maximal gain, Fig. 6.13b, due to the increase in residual ISI from the increasing bit rate. Combining both transmitter and receiver equalization with RC filtering, we measured the BER versus bit rate with allocation for FEC, Fig. 6.13c. At BERs $>10^{-6}$, the symbol errors were physically counted offline. Through 50m OM5, data rates reached 168Gbps with FEC allocation for an effective >163Gbps, conclusively demonstrating a >160Gbps VCSEL solution for data centers and continued growth in VCSEL MMF line rates.

6.4 2λ x 107Gbps PAM-4 Transmission over 1100m OM5

The majority of optical interconnects in a data center are <30m and consist of 850nm multimode vertical-cavity surface-emitting lasers (VCSELs) and multimode fiber (MMF) due to their energy efficiency, low cost, and high density form factor. These solutions are generally constrained to <150m due to chromatic and modal dispersion limitations. The effects of both dispersions can be efficiently mitigated by reducing the number of VCSEL modes, ideally to achieve single-mode (SM) operation [141]. At longer reaches, demonstrations of 54Gbps PAM-2 over 2200m MMF [142], 25Gbps over 1500m graded-index SMF [143], and 51.56Gbps PAM-4 over 2300m MMF [144], but required either extensive equalization (40 taps) or hard-decision forward error correction (HD-FEC) with 12% overhead. Improvements in SM VCSEL bandwidth and power have led to experimental demonstration 60Gbps PAM-2 over 800m MMF [145] with no equalization and KP4 FEC. Yet, it is important to establish that SM VCSELs can operate under IEEE 802.3cm standards set for multimode VCSEL MMF links (such as two-lambda SWDM,

transmitter and receiver equalization, PAM-4 modulation, low-latency KP4 FEC, etc.) to exhibit transition between SM and MM VCSELs that maintains the high-speed, low-power VCSEL link characteristics without having to redesign existing analog electronic drivers.

In this section, we demonstrate greater than 100Gbps PAM-4 signaling over 1100m of OM5 MMF and 50Gbps PAM-2 over 1550m OM5 MMF, using 850nm and 910nm unpackaged VCSELs with allocation for KP4 FEC. Equalization is implemented at the transmitter and receiver as a static feed-forward equalizer (FFE). Additionally, we include raised cosine (RC) filtering to demonstrate the benefits of shaping the electric signal for a typical equalized VCSEL link channel. Furthermore, we examine the maximum achievable error-free (BER $<10^{-12}$) reach for PAM-4 and PAM-2 and demonstrate error-free 120Gbps PAM-4 over 750m OM5, 107Gbps PAM-4 over 900m OM5, 70Gbps PAM-2 over 800m OM5, 60Gbps PAM-2 over 1100m OM5, and 53.5Gbps PAM-2 over 1300m OM5. We show SM VCSEL technology is capable of scaling to faster data rates, with multiple lambda, over >1000m fiber lengths to provide energy efficient optical interconnects for all demands within data centers.

6.*4.1* *Single Mode VCSEL Benefits, Equalization and Pulse Shaping, and PAM-2 Data Rate Tests*

The SM 850nm and 910nm VCSELs had one transverse mode with SSMR >30dB. Even with a single transverse mode, both VCSEL wavelengths produced >2.2dBm optical power at 3mA. The full width at half-maximum (FWHM) of the transverse mode was 0.021nm and 0.025nm of the 850nm and 910nm VCSEL, respectively. Typically, MM VCSEL MMF links are reach limited by chromatic dispersion, modal dispersion, and fiber

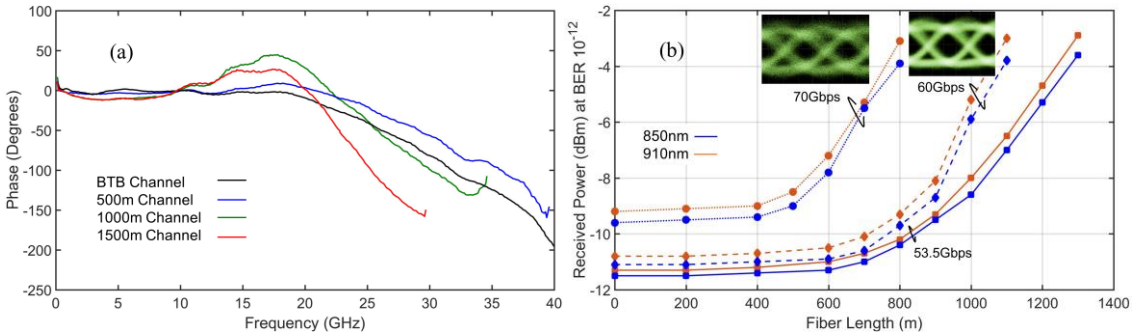

Fig. 6.14: Measured phase response through back-to-back (btb), 500m, 1000m, and 1500m channel; (b) Received power for error-free transmission with 53.5Gbps, 60Gbps, and 70Gbps PAM-2 on an equalized channel from 0m to 1400m of OM5 fiber with eye diagrams of 60Gbps and 70Gbps PAM-2 next to their respective curves.

effective modal bandwidth (EMBc). SM VCSELs are not as effected by dispersion due to their small spectral content and typical under filled launch conditions.

At the transmitter, a static UI-spaced 6-tap FFE filter response was applied based on the channel response. An RC filter, as described in the experimental setup, was added for deliberate shaping of the drive signal to match the equalized channel and reduce ISI. The static 5-tap T-spaced receiver equalizer consisted of 1 pre- and 3 post-taps. The bandwidth of the fiber plays a negligible role in limiting the bandwidth of the system, resulting in consistent channel bandwidth and slow change in phase over longer lengths of fiber, Fig. 6.14a.

53.5Gbps, 60Gbps, and 70Gbps PAM-2 were tested for maximum reach, Fig. 6.14b. BER was calculated by PDF analysis every 100m of OM5 length. The 850nm and 910nm VCSEL behaved similarly and differences in received powers for the same data and fiber distance were <0.5dB. The fiber attenuation increased by approximately 0.5dB/200m. At an error-free BER, 70Gbps reached 800m, 60Gbps reached 1100m, and 53.5Gbps reach 1300m. For 53.5Gbps and 60Gbps, significant power penalties for increasing distance are

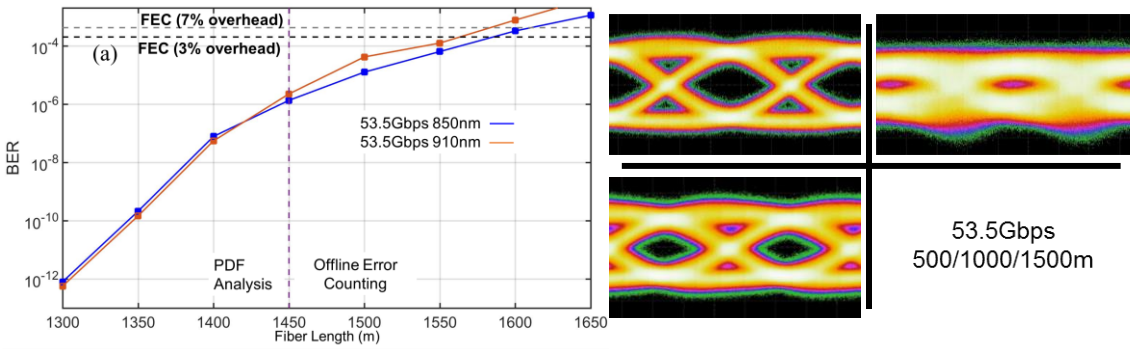

Fig. 6.15: (a) Bit error rate (BER) of RC PAM-2 from 1300m to 1650m of OM5 fiber. FEC limit marked by black (3%) and gray (7%) dashed line; (right half) 910nm VCSEL eye diagrams for 53.5Gbps PAM-2 through 500m OM5 (top left), 1000m through OM5 (bottom left), and 1500m through OM5 (top right) before receiver equalization.

not observed until after 800m OM5. At 70Gbps, large penalty increases are not discernable until 500m OM5. We note these penalties are most likely due to the receiver equalizer not being able to compensate for the phase completely as the fiber length increased. This effect will be exacerbated in faster data rates (70Gbps), where the receiver equalizer may be required to not only correct for channel phase, but also residual ISI from band limitations. By allocating overhead for FEC, fiber reach extended 250m, Fig. 6.15a. 7% overhead was included for two different types of low-latency FEC, but the target BER was for KP4 FEC (3% overhead). No burst errors were found when offline counting errors at BERs >10-6. Both 850nm and 910nm VCSELs reached 1550m OM5 with FEC allocation at 53.5Gbps PAM-2 for an aggregate 100Gbps throughput.

6.4.2 PAM-4 Analysis

PAM-4 is investigated to increase data throughput by increasing the bits transmitted per symbol. Compared to PAM-2 it incurs a 4.77dB sensitivity penalty for the addition of two more amplitude levels. 107Gbps and 120Gbps PAM-4 were tested for maximum error-free reach, Fig 6.16a. 120Gbps reached 750m OM5 while 107Gbps reached 900m OM5.

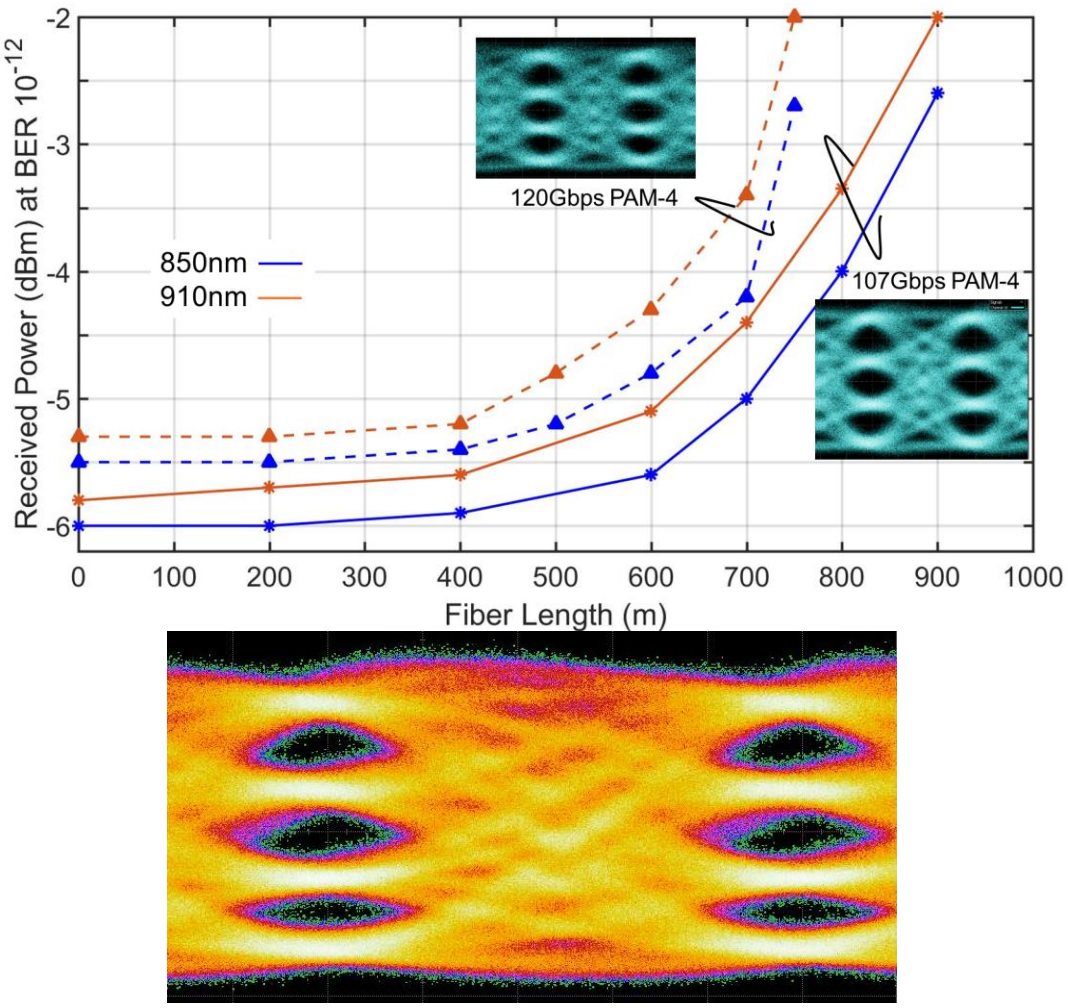

Fig. 6.16: (a) Received power for error-free transmission with 53.5Gbaud and 60Gbaud on an equalized channel from 0m to 1000m of OM5 fiber with eye diagrams of 53.5Gbaud and 60Gbaud PAM-4 next to their respective curves; (bottom) 850nm VCSEL PAM-4 eye diagram of 53.5Gbaud through 500m OM5 before receiver equalization.

Significant power penalties were not observed until beyond 500m OM5. With FEC allocation, fiber reach extends 200m, to 1100m, Fig. 6.17a. Similar to the PAM-2 case, no burst errors were found when offline counting errors. Both 850nm and 910nm VCSELs reached 1100m OM5 with FEC at 107Gbps PAM-4 for an aggregate 200Gbps throughput.

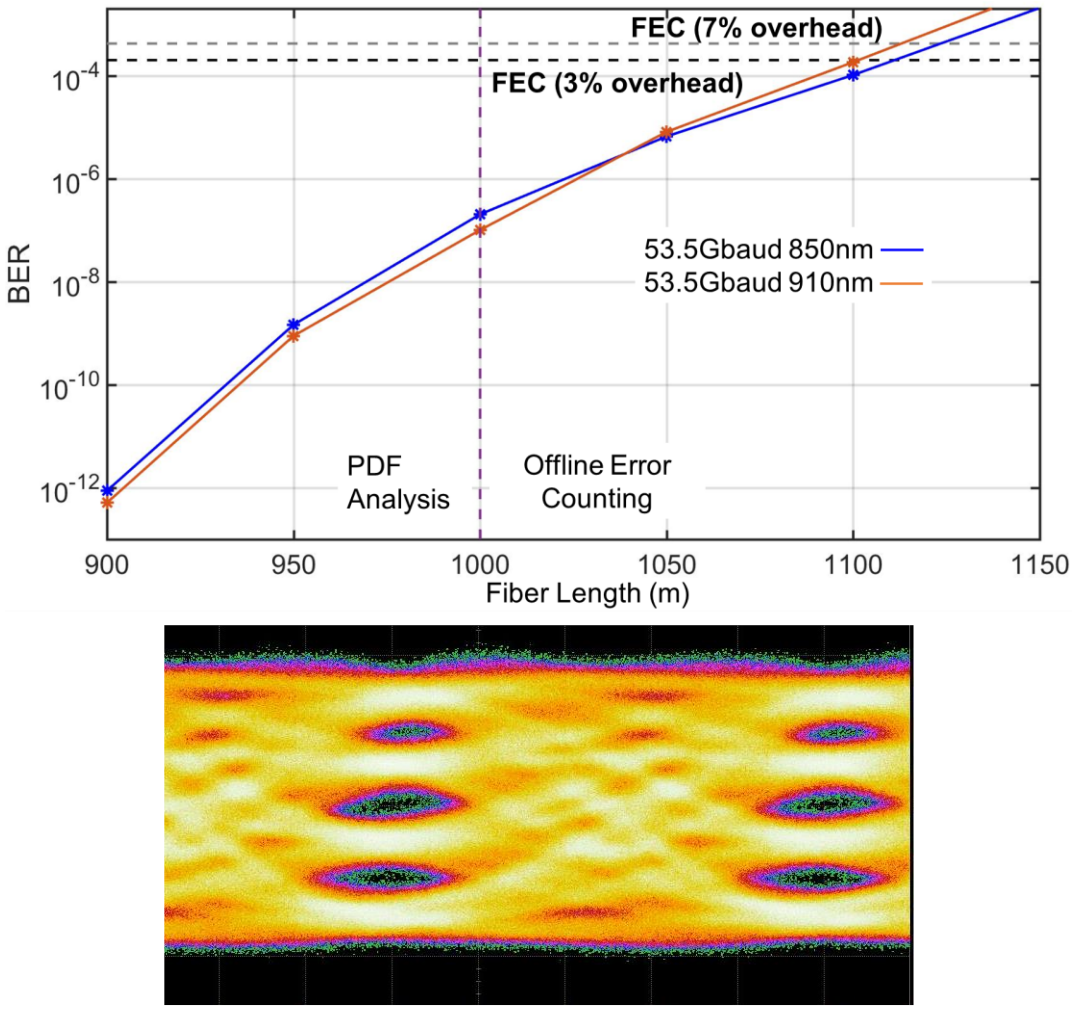

Fig. 6.17: (a) Bit error rate (BER) of RC PAM-4 from 900m to 1150m of OM5 fiber. FEC limit marked by black (3%) and gray (7%) dashed line; (bottom) 850nm VCSEL PAM-4 eye diagram of 53.5Gbaud through 1000m OM5 before receiver equalization.

CHAPTER 7. CONCLUSIONS

7.1 VCSEL-Based Fiber Optic Communication

To address the rapid growth in the bandwidth needs, the IEEE 802.3 standard work groups continue to evolve standardizing optical links with targets for 100Gbps PAM-4. Consequently, some of the impairments that are negligible at lower speeds start to become prominent which need further investigation. The research began by addressing the concern of data rate limitations due to RIN and MPN. We introduced the notion of a misunderstanding of VCSEL noise behavior in Chapter 3. For the first time, VCSEL transverse modes were isolated with enough power to make meaningful measurements of their noise, and thus capture the cross-correlations due to mode gain competition. We demonstrated that mode partition noise (MPN) had a minimal effect on the overall noise of the system for the lengths of fiber being considered for IEEE standards. We also discovered that relative intensity noise was dependent on the effects fiber dispersion have on the transverse mode cross-correlation. We showed that RIN enhancement can be detrimental to an optical link, and perhaps there is an optimum set of modes that provides the least amount of RIN enhancement over a 100m link. In Chapter 4, we demonstrated a progression of data improvement in part realized by Chapter 3. Through improvements on both the electrical and optical side we demonstrate the progression from 50Gbps PAM-4 with FEC to 100Gbps PAM-4 error-free. We detail the considerations and trade-offs when addressing channel impairments at the transmitter and receiver. And, we conclude with a section discussing the most cost-effective way to design a system for a target length or data rate given the bandwidth of the system. In Chapter 5, we expanded on the idea of wave

division multiplexing (SWDM) applying the data rates of Chapter 4 to more wavelengths in an effort to increase capacity from 100Gbps per fiber to 1Tbps per fiber. We demonstrated how a system of 4 lambda operated over new OM5 fiber. We also showed the effects of different transmitter and receiver equalization strategies, depending on the tap length or type of equalizer. Further research was presented proving that VCSEL wavelengths from 850nm to 1060nm could all operate over OM5 fiber enabling 8 lambda per fiber at over 100Gbps over 100m. Most importantly, we showed that the same equalization provided similar results across all the wavelengths. Finally, in Chapter 6, we demonstrated state-of-the-art data rates using the latest in electronic and optical equipment. We demonstrated with the newest generation of VCSELs >100Gbps NRZ and >160Gbps PAM-4 over 50m of OM5 fiber. We also demonstrated, using single mode VCSELs at 850nm and 910nm, the ability to transmit 50Gbps NRZ and 100Gbps PAM-4 over 1500m and 1100m of OM5 fiber, respectively. This demonstrates the continued ability of VCSEL interconnects to scale data rates and possibly reach 200Gbps PAM-4. We demonstrated the ability of VCSELs to reach over 1000m at 100Gbps as well, making VCSELs a potential option for all data center intraconnects.

7.2 Future Directions

Based off the work in Chapters 3-6, investigation is needed for near-term and long-term development and deployment of links. In the near-term, the next standard will most likely target 100Gbps PAM-4 and/or 50Gbps NRZ VCSEL links for data centers. At this stage in development, it is important to investigate how VCSELs from different vendors behave with PAM-4 signaling and how much equalization will be needed to allow for a general standard that fits most VCSEL vendors. Additionally, noise limitations for the laser

will need to be investigated as more complex equalization tends to lead to a higher noise enhancement of the electrical signal. Worst-case limitations will need to be developed for 100Gbps PAM-4 links with regards to older generations of VCSELs and noise enhancement through fiber.

For the long-term, increasing the number of wavelengths and increasing serial data rates needs to be investigated. There is some community notion that silicon photonics will take over for VCSELs in data center applications; however, this is not true due to VCSEL links low power and low cost when it is possible for a datacenter to have >250000 links that are <30m. To reduce the number of links, more investigation will be needed for efficient and low-area optical MUXs and deMUXs. To develop the data rates presented in Chapter 6, more research will be needed for equalization optimization and driver impedance matching to avoid electrical back reflections. The most research will be needed in the area of single mode VCSELs, especially since they are being considered for transmission through multimode fiber. Ideally, single mode fiber at 850nm would be best, but until it is taken up by industry for production, SM to MM coupling will need to be investigated. For future investigation, measuring the effects of off-center launches, overfilled launches, and transmission through fibers with kinks will be important. It is important to determine if the only tradeoff is optical power for a more confined optical spectra, resulting in reduced dispersion effects. Researching on all these fronts should provide path for continued growth in VCSEL optical interconnects for 10 to 15 years to come.

PUBLICATIONS

Journal Publications

J. Lavrencik, *et al.*, “Scaling VCSEL-MMF Links to 1 Tb/s Using Short Wavelength Division Multiplexing," *J. of Lightwave Tech.*, v. 36, n. 18, pp. 4138-4145, Sept. 15, 2018.

S. K. Pavan, **J. Lavrencik** and S. E. Ralph, “VCSEL-Based PAM-4 Links up to 62 Gbit/s Over OM3, OM4, and WB-MMF: Performance Comparison at 850 nm and 1050 nm," *J. of Lightwave Tech.*, v. 35, n. 9, pp. 1614, May 1, 2017.

S. K. Pavan, **J. Lavrencik** and S. E. Ralph, “New Model for Mode Partition Noise in VCSEL-MMF Links Based on Langevin-Driven Spatio-Temporal Rate Equations," *J. of Lightwave Tech.*, v. 34, n. 16, pp. 3733-3751, Aug. 15, 2016.

J. Lavrencik, S. K. Pavan, D. K. Haupt and S. E. Ralph, “Direct Measurement of VCSEL Transverse Mode Correlation and kmpn," *Photonics Tech. Letters*, v. 27, n. 19, pp. 2031-2034, Oct. 1, 2015.

Awarded

J. Lavrencik, *et al.*, “DSP-Enabled 100 Gb/s PAM-4 VCSEL MMF Links." *J. of Lightwave Tech.*, v. 35, n. 15, pp. 3189-3196, Aug. 1, 2017.

J. Lavrencik, *et al.*, “Noise in VCSEL-Based Links: Direct Measurement of VCSEL Transverse Mode Correlations and Implications for MPN and RIN," *J. of Lightwave Tech.*, v. 35, n. 4, pp. 698-705, Feb. 15, 2017.

Conference Publications

J. Lavrencik et al., “168Gbps PAM-4 Multimode Fiber Transmission through 50m using 28GHz 850nm Multimode VCSELs,” *Optical Fiber Communication Conference (OFC)*, San Diego, CA, 2020.

J. Lavrencik, *et al.*, “Error-Free 100Gbps PAM-4 Transmission over 100m OM5 MMF using 1060nm VCSELs,” *Optical Fiber Communication Conference (OFC)*, San Diego, CA, 2019.

S. Varughese, **J. Lavrencik**, and S.E. Ralph, “Probabilistic Shaping for VCSEL-MMF Links," *IEEE Avionics and Vehicle Fiber-Optics and Photonics Conference (AVFOP)*, Portland, OR, 2018.

J. Lavrencik, *et al.*, “Power Efficient Modulation Formats for Error-Free VCSEL MMF Links," *European Conference on Optical Communication (ECOC)*, Rome, Italy, 2018.

A. Melgar, V.A. Thomas, **J. Lavrencik**, and S. E. Ralph, “Multimode VCSEL Parameter Extraction for Optical Link Models," *European Conference on Optical Communication (ECOC)*, Rome, Italy, 2018.

J. Lavrencik, *et al.*, “Optimum VCSEL Apertures for High-Speed Multimode Fiber Links," *Optical Fiber Communications Conference and Exposition (OFC)*, San Diego, CA, 2018.

S. Varughese and **J. Lavrencik**, *et al.*, "Polybinary Coding for Low Complexity High Speed Error-Free VCSEL-MMF Links," *European Conference on Optical Communication (ECOC)*, Göteberg, Sweden, 2017.

J. Lavrencik, *et al.*, "Error-Free 100Gbps PAM-4 Transmission over 100m Wideband Fiber Using 850nm VCSELs," *European Conference on Optical Communication (ECOC)*, Göteberg, Sweden, 2017.

A. Melgar, V. A. Thomas, **J. Lavrencik**, S. Varughese, and S. E. Ralph, "Experimentally benchmarked fiber propagation model for 50Gbps PAM-4 MMF links employing multimode VCSELs," *Optical Fiber Communications Conference and Exhibition (OFC)*, Los Angeles, CA, 2017.

S. Varughese, **J. Lavrencik**, V. A. Thomas and S. E. Ralph, "Raised cosine pulse shapes for next generation MMF links," *IEEE Photonics Conference (IPC)*, Waikoloa, HI, 2016.

J. Lavrencik, *et al.*, "2λ × 100Gbps PAM-4 wideband fiber 100m links using 850nm and 940nm VCSELs," *IEEE Photonics Conference (IPC)*, Waikoloa, HI, 2016.

S. Varughese, **J. Lavrencik**, V. A. Thomas, and S. E. Ralph, "Raised Cosine Pulse Shapes for next Generation MMF Links," *IEEE Photonics Conference (IPC)*, Waikoloa, HI, 2016.

J. Lavrencik, *et al.*, "100Gbps PAM-4 Transmission over 100m OM4 and Wideband Fiber using 850nm VCSELs," *European Conference on Optical Communication (ECOC)*, Dusseldorf, Germany, 2016.

J. Lavrencik, S. K. Pavan, D. K. Haupt and S. E. Ralph, "Direct measurement of transverse mode correlation and MPN using 900nm VCSELs," *Optical Fiber Communications Conference and Exhibition (OFC)*, Los Angeles, CA, 2015.

S. K. Pavan, **J. Lavrencik** and S. E. Ralph, "Experimental demonstration of 51.56 Gbit/s PAM-4 at 905nm and impact of level dependent RIN," *European Conference on Optical Communication (ECOC)*, Cannes, France, 2014.

S. K. Pavan and **J. Lavrencik**, *et al.*, "50Gbit/s PAM-4 MMF transmission using 1060nm VCSELs with reach beyond 200m," *Optical Fiber Communications Conference and Exhibition (OFC)*, San Francisco, CA, 2014.

Invited

N. N. Ledentsov, V.A. Shchukin, V.P. Kalosha, N. Ledentsov Jr, L. Chorchos, J. P. Turkiewicz, U. Hecht, P. Kurth, F. Gerfers, **J. Lavrencik**, S. Varughese, and S. E. Ralph, "Optical Interconnects Using Single-Mode and Multi-Mode VCSEL and Multi-Mode Fiber," *Optical Fiber Communication Conference (OFC)*, San Diego, CA, 2020.

S. E. Ralph and **J. Lavrencik**, "High Capacity VCSEL Links," *Optical Fiber Communication Conference (OFC)*, San Diego, CA, 2019.

S. E. Ralph, **J. Lavrencik**, and A. Melgar, "VCSELs and 100G," *International Society for Optical Engineering (SPIE)*, San Francisco, CA, 2019.

S. E. Ralph, **J. Lavrencik**, and S. Varughese, "Terabit VCSEL Interconnects," IEEE Optical Interconnects, Santa Fe, NM, 2018.

S. E. Ralph, and **J. Lavrencik**, "VCSEL Modal Dynamics and Implications for 100Gbps Links," *International Society for Optical Engineering (SPIE)*, San Francisco, CA, 2017.

S. E. Ralph, and **J. Lavrencik**, “Requirements and results for practical VCSEL transmission using PAM-4 over MMF," *Optical Fiber Communications Conference and Exhibition (OFC)*, Anaheim, CA, 2016.

S. E. Ralph, S. K. Pavan, and **J. Lavrencik**, “Noise and high speed MMF links,” *POF International Conference on Plastic Optical Fibers*, Yokohama, Japan, 2014.

Awarded

J. Lavrencik et al., “102Gbps PAM-2 over 50m OM5 Fiber using 850nm Multimode VCSELs,” *IEEE Photonics Conference (IPC)*, San Antonio, TX, 2019.

J. Lavrencik, *et al*., “4λ × 100Gbps VCSEL PAM-4 transmission over 105m of wide band multimode fiber," *Optical Fiber Communications Conference and Exhibition (OFC)*, Los Angeles, CA, 2017.

REFERENCES

[1] Cisco Global Cloud Index: Forecast and Methodology, 2016–2021. [online]. https://www.cisco.com/c/en/us/solutions/collateral/service-provider/global-cloud-index-gci/white-paper-c11-738085.pdf.

[2] J. Petrilla. (2012, September). Example MMF Link Model. IEEE 802.3bm 40Gbps and 100Gbps Fiber Optic Task Force. [Online]. http://www.ieee802.org/3/bm/public/sep12/ExampleMMF_LinkModel_%2012_09_18.xlsx.

[3] IEEE 802.3 400Gbps over Multimode Fiber Task Force. [online]. http://www.ieee802.org/3/cm/index.html.

[4] IEEE P802.3bm 40Gbps and 100Gbps Fiber Optic Task Force. [online] http://www.ieee802.org/3/bm/.

[5] D. Cunningham, “Modifications To The Mode Partition Noise Penalty Calculation For Equalised 32GFC Links,” Proc. FC-PI-6, New Orleans, LA, (2011).

[6] K. Szczerba, "Multilevel modulation in short-range optical links," Department of Microtechnology and Nanoscience (MC2), Chalmers University of Technology, 2013.

[7] G.P. Agrawal, Fiber-Optic Communication Systems. Fourth Edition. Wiley, 2010.

[8] K. Balemarthy., "Electronic Equalization of High-Speed Multi-Mode Fiber Links," Ph.D. dissertation, Dept. of Elect. Eng., Georgia Tech., Atlanta, GA, 2007.

[9] J. Castro, et al., “Mode Partition Noise and Modal-Chromatic Dispersion Interaction Effects on Random Jitter”, J. Lightw. Technol, vol. 31, no. 15, pp 2629-2638, 2013.

[10] S. K. Pavan., "VCSEL-Based Multi-Mode Fiber Optical Link for 100Gbit/s Transmission: Advanced Simulation Tools and Experimental Link Studies," Ph.D. dissertation, Dept. of Elect. Eng., Georgia Tech., Atlanta, GA, 2016.

[11] L. A. Coldren, S. W. Corzine, and M. L. Mashanovitch. Diode lasers and photonic integrated circuits. Wiley, 2012.

[12] “IEEE standard for information technology telecommunications and information exchange between systems local and metropolitan area networks specific requirements,” available online http:// standards.ieee.org/findstds/standard/802.3ba-2010.html.

[13] K. Iga, S. Kinoshita, and F. Koyama, “Microcavity GalaAs/GaAs surface-emitting laser with Ith = 6 mA,” Electron. Lett., 23(3):134– 136, Jul. 1987.

[14] Florian Breyer, S.C. Jeffrey Lee, Sebastian Randel, Norbert Hanik, “Comparison of OOK- and PAM-4 Modulation for 10 Gbit/s Transmission over up to 300 m Polymer Optical Fiber”, Proc. Optical Fiber Communication (OFC/NFOEC) Conf., March 2008.

[15] M. Amann, “Semiconductor lasers: Tuning triumph,” Nature Photon., 2(3):134–135, Mar. 2008.

[16] P. Moser, J. A. Lott, P. Wolf, G. Larisch, H. Li, N. N. Ledentsov, and D. Bimberg, “56 fJ dissipated energy per bit of oxide-confined 850 nm VCSELs operating at 25 Gbit/s,” Electron. Lett., 48(20):1292–1294, 2012.

[17] P. Moser, W. Hofmann, P. Wolf, J. A. Lott, G. Larisch, A. Payusov, N. N. Ledentsov, and D. Bimberg, “81 fJ/bit energy-to-data ratio of 850 nm vertical-cavity surface-emitting lasers for optical interconnects,” Appl. Phys. Lett., 98(23):231106, 2011.

[18] N. Haghighi, P. Moser, and J. Lott, “Power, Bandwidth, and Efficiency of Single VCSELs and Small VCSEL Arrays,” IEEE Journal of Selected Topics in Quantum Electronics, 2019.

[19] R. Safaisini, K. Szczerba, E. Haglund, P. Westbergh, J. S. Gustavsson, A. Larsson, and P. A. Andrekson, “20 Gbit/s error-free operation of 850 nm oxide-confined VCSELs beyond 1 km of multimode fibre,” Electron. Lett., 48(19):1225–1227, 2012

[20] R. Safaisini, K. Szczerba, P. Westbergh, E. Haglund, B. K¨ogel, J. S. Gustavsson, M. Karlsson, P. Andrekson, and A. Larsson, “High-speed 850nm quasi-single-mode VCSELs for extended-reach optical interconnects,” J. Opt. Commun. Netw., 5(7):686–695, Jul 2013.

[21] E. Haglund, A. Haglund, P. Westbergh, J. S. Gustavsson, B. Kogel, and A. Larsson, "25 Gbit/s transmission over 500 m multimode fibre using 850 nm VCSEL with integrated mode filter," Electron. Lett., 48(9):517–519, 2012.

[22] "IEEE standard for ethernet," available online http://standards.ieee.org/about/get/802/802.3.html.

[23] J. A. Tatum, D. Smith, J. K. Guenter, and R. H. Johnson. "Highspeed characteristics of VCSELs," 1997.

[24] M.X. Jungo, D. Erni, and W. Bachtold, "VISTAS: a comprehensive system-oriented spatiotemporal VCSEL model," IEEE J Sel Top Quant Electron, 2003, 9: 939–948.

[25] J. Perchoux, A. Rissons, and J.C. Mollier, "Multimode VCSEL model for wide frequency-range RIN simulation," Opt. Commun, 2008, 281: 162–169.

[26] D. Lenstra and M. Yousefi, "Rate-equation model for multi-mode semiconductor lasers with spatial hole burning," Opt Express, 2014, 22: 8143–8149.

[27] W. Hamad, S. Wanckel, and W.H.E. Hofmann, "Small-signal analysis of ultra-high-speed multi-mode VCSELs," IEEE J Quant Electron, 2016, 52: 1–11.

[28] H.B. Wang, W.V. Sorin, S. Palermo, et al., "Comprehensive vertical-cavity surface-emitting laser model for optical interconnect transceiver circuit design," Opt Eng, 2016, 55.

[29] G. Belfiore, M. Khafaji, R. Henker et al., "A compact electro-optical VCSEL model for high-speed IC design," In: Proceedings of the 12th Conference on Ph.D. Research in Microelectronics and Electronics (PRIME), Lisbon, 2016.

[30] S. Entezam, A. Zarifkar, and M.H. Sheikhi, "Thermal equivalent circuit model for coupled-cavity surface-emitting lasers," IEEE J Quant Electron, 2015, 51: 1–8.

[31] A. Gholami, A. Toffano, A. Destrez et al., "Optimization of VCSEL spatiotemporal operation in MMF links for 10-Gb Ethernet," IEEE J Sel Top Quant Electron, 2006, 12: 767–775.

[32] S. Bottacchi. Multi-gigabit Transmission over Multimode Optical Fiber: Theory and Design Methods for 10 GbE Systems. 7th edition. New York: Wiley, 2006.

[33] G.R. Hadley, "Effective index model for vertical-cavity surface-emitting lasers," Opt Lett, 1995, 20: 1483–1485.

[34] B. E. A. Saleh and M. C. Teich. Fundamentals of photonics. Wiley, 1991.

[35] A. W. Snyder and J. Love. Optical Waveguide Theory. Springer, 1983.

[36] P. Pepeljugoski, S. E. Golowich, A. J. Ritger, P. Kolesar, and A. Risteski, "Modeling and simulation of next-generation multimode fiber links," IEEE J. Lightw. Technol., 21(5):1242–1255, May 2003.

[37] R. Pimpinella and A. Brunsting, "Differential mode delay (DMD) for multimode fiber types and its relationship to measured performance," in Proc. OFC, paper NWF2, Mar. 2005.

[38] L. Raddatz, I. H. White, D. G. Cunningham, and M. C. Nowell, "Increasing the bandwidth-distance product of multimode fibre using offset launch," Electron. Lett., 33(3):232–233, Jan. 1997.

[39] R. Olshansky, "Propagation in glass optical waveguides," Rev. Mod. Phys., 51:341–367, Apr, 1979.

[40] B. Franz and H. Bulow, "Experimental evaluation of principal mode groups as high-speed transmission channels in spatial multiplex systems," IEEE Photon. Technol. Lett., 24(16):1363–1365, 2012.

[41] R. E. Freund, C. Bunge, N. N. Ledentsov, D. Molin, and C. Caspar, "High-speed transmission in multimode fibers," IEEE J. of Lightw. Technol., 28(4):569–586, 2010.

[42] D. Gloge and E. A. J. Marcatili, "Multimode theory of graded-core fibers," Bell Syst. Tech. J, 52(9):1563–1578, 1973.

[43] D. Molin, M. Astruc, and P. Sillard, "Chromatic dispersion compensated multimode fibers for data communications," in Proc. ECOC, paper Tu.3.C.3, Sept. 2011.

[44] N. N. Ledentsov, J. A. Lott, J.-R. Kropp, V. A. Shchukin, D. Bimberg, P. Moser, G. Fiol, A. S. Payusov, D. Molin, G. Kuyt, A. Amezcua, L. Y. Karachinsky, S. A. Blokhin, I. I. Novikov, N. A. Maleev, C. Caspar, and R. Freund, "Progress on single mode VCSELs for data- and tele-communications," Proc. SPIE, 8276:82760K–82760K–11, 2012.

[45] M. Webster, L. Raddatz, I. H. White, and D. G. Cunningham, "A Statistical Analysis of Conditioned Launch for Gigabit Ethernet Links Using Multimode Fiber," IEEE Journal of Lightwave Technology, vol. 17, no. 9, pp. 1532–1541, September, 1999.

[46] 108 Fiber Model, IEEE 802.3aq (10G-LRM) Task Force. [Online]. Available: http://www.ieee802.org/3/aq/public/tools/108fiberModel (June, 2007).

[47] Monte Carlo Fiber Model, IEEE 802.3aq (10G-LRM) Task Force. [Online]. Available: http://www.ieee802.org/3/aq/public/tools/MonteCarlo/OM1/ (June, 2007).

[48] J. A. Buck. Fundamentals of Optical Fibers. New York: Wiley, 1995.

[49] J. M. Castro, R. Pimpinella, B. Kose, and B. Lane, "Investigation of the interaction of modal and chromatic dispersion in VCSEL-MMF channels," J. Lightw. Technol., vol. 30, no. 15, pp. 2532–2541, 2012.

[50] A. Gholami, D. Molin, and P. Sillard, "Compensation of chromatic dispersion by modal dispersion in MMF- and VCSEL-based gigabit ethernet transmissions," IEEE Photon. Technol. Lett., vol. 21, no. 10, pp. 645–647, 2009.

[51] A. Sengupta, "Comparison of min-EMBc and DMD template based qualification of high bandwidth multimode fibers," in Proc. IWCS, pages 154–160, 2007.

[52] A. Sengupta, "Calculated modal bandwidths of an OM4 fiber and the theoretical challenges," in Proc. IWCS, volume 9, pages 24–29, 2009.

[53] N. N. Ledentsov, J. A. Lott, D. Bimberg, A. Mutig, G. Fiol, S. A. Blokhin, A. M. Nadtochiy, V. A. Shchukin, J. Kropp, I. I. Novikov, L. Y. Karachinsky, and M. V. Maximov, "High-speed single-mode quantum dot and quantum well VCSELs," Proc. SPIE, 7952:79520J– 79520J–9, 2011.

[54] R. S. Quimby. Photonics and Lasers. Wiley, 2006.

[55] G. P. Agrawal. Lightwave technology: telecommunication systems. Wiley-Interscience, 2005.

[56] A. Valle and L. Pesquera, “Relative intensity noise of multitransversemode vertical-cavity surface-emitting lasers,” IEEE Photon. Technol. Lett., 13(4):272–274, Apr. 2001.

[57] K. Ogawa, “Analysis of mode partition noise in laser transmission systems,” IEEE J. Quantum Electron., vol. 18, no. 5, pp. 849–855, May 1982.

[58] K. Ogawa and R. S. Vodhanel, “Measurements of mode partition noise of laser diodes,” IEEE J. Quantum Electron., vol. 18, no. 7, pp. 1090–1093, Jul. 1982.

[59] G. P. Agrawal et al., “Dispersion penalty for 1.3- m lightwave systems with multimode semiconductor lasers,” J. Lightw. Technol., vol. 6, no. 5, pp. 620–625, May 1988.

[60] P. Pepeljugoski, “Dynamic behavior of mode partition noise in multimode fiber links,” J. Lightw. Technol., vol. 30, no. 15, Aug. 2012.

[61] J. M. Castro, R. Pimpinella, B. Kose, and B. Lane, “The interaction of modal and chromatic dispersion in VCSEL based multimode fiber channel links and its effect on mode partition noise,” in Proc. 61st IWCS, 2012.

[62] J. Karout, E. Agrell, K. Szczerba, and M. Karlsson, “Optimizing constellations for single-subcarrier intensity-modulated optical systems,” IEEE. Trans. Inf. Theory, 58(7):4645–4659, 2012.

[63] J. G. Proakis. Digital communication. McGraw-Hill, 2008.

[64] S. Hranilovic and F. R. Kschischang, “Optical intensity-modulated direct detection channels: signal space and lattice codes,” IEEE T. Inform. Theory, 49(6):1385–1399, Jun. 2003.

[65] J. M. Kahn and J. R. Barry, “Wireless infrared communications,” Proc. IEEE, 85(2):265–298, Feb. 1997.

[66] "MicropodTM optical transmitter and receiver modules," available online http://www.avagotech.com/pages/en/press/micropod.

[67] L. Schares, D. M. Kuchta, and A. F. Benner, "Optics in future data center networks," in Proc. HOTI, pages 104–108, August 2010.

[68] J. D. Ingham, R. V. Penty, and I. H. White, "10 Gb/s transmitter based equalization for extended-reach multimode-fiber data communication links," in Proc. OFC, paper, March 2007.

[69] D. M. Kuchta, C. L. Schow, A. V. Rylyakov, J. E. Proesel, F. E. Doany, C. Baks, B. H. Hamel-Bissell, C. Kocot, L. Graham, R. Johnson, G. Landry, E. Shaw, A. MacInnes, and J. Tatum, "A 56.1 Gb/s NRZ modulated 850nm VCSEL-based optical link," in Proc. OFC, paper OW1B.5, 2013.

[70] J. D. Ingham, R. V. Penty, and I. H. White, "10 Gb/s & 20 Gb/s extended-reach multimode-fiber data communication links using multilevel modulation and transmitter-based equalization," in Proc. OFC, paper, February 2008.

[71] I. H. White, J. D. Ingham, and R. V. Penty, "Systems aspects of optical technologies for use in data communications," in Proc. OFC, paper OMM1, March 2011.

[72] "Q:active active copper cables," available online http://www.intersil.com/signalintegrity/ ActiveCables.asp.

[73] S. Walklin and J. Conradi, "Multilevel signaling for increasing the reach of 10 Gb/s lightwave systems," IEEE J. Lightw. Technol., 17(11):2235–2248, Nov. 1999.

[74] J. K. Pollard, "Multilevel data communication over optical fibre," IEEE P-COMMUN, 138(3):162–168, Jun. 1991.

[75] J. L. Zerbe, C. W. Werner, V. Stojanovic, F. Chen, J. Wei, G. Tsang, D. Kim, W. F. Stonecypher, A. Ho, T. P. Thrush, R. T. Kollipara, M. A. Horowitz, and K. S. Donnelly, "Equalization and clock recovery for a 2.5-10-Gb/s 2-PAM/4-PAM backplane transceiver cell," IEEE J. Solid-St. Circ., 38(12):2121–2130, Dec. 2003.

[76] F. Breyer, S. C. J. Lee, S. Randel, and N. Hanik, "Comparison of OOK- and PAM-4 modulation for 10 Gbit/s transmission over up to 300 m polymer optical fiber," in Proc. OFC, paper OWR2, Feb. 2008.

[77] F. Breyer, S. C. J. Lee, S. Randel, and N. Hani, “PAM-4 signalling for gigabit transmission over standard step-index plastic optical fibre using light emitting diodes,” in Proc. ECOC, paper We.2.A.3, Sept. 2008.

[78] J. E. Cunningham, D. Beckman, X. Zheng, D. Huang, T. Sze, and A. V. Krishnamoorthy, “PAM-4 signaling over VCSELs with 0.13 μm CMOS chip technology,” Opt. Express, 14(25):12028–12038, Dec. 2006.

[79] J. D. Ingham, R. V. Penty, I. H. White, P. Westbergh, J. S. Gustavsson, ˚A. Haglund, and A. Larsson, “32 Gb/s multilevel modulation of an 850 nm VCSEL for next-generation datacommunication standards,” in Proc. CLEO, paper CWJ2, May 2011.

[80] T. Toifl, C. Menolfi, M. Ruegg, R. Reutemann, P. Buchmann, M. Kossel, T. Morf, J. Weiss, and M. L. Schmatz, “A 22 Gb/s PAM-4 receiver in 90-nm CMOS SOI technology,” IEEE J. Solid-State Circuits, 41(4):954–965, Apr. 2006.

[81] E. Agrell, J. Lassing, E. G. Ström, and T. Ottosson, “On the optimality of the binary reflected Gray code,” IEEE Trans. Inf. Theory, vol. 50, no. 12, pp. 3170–3182, Dec. 2004.

[82] K. Szczerba, P. Westbergh, J. Karout, J. S. Gustavsson, Å. Haglund, M. Karlsson, P. A. Andrekson, E. Agrell, and A. Larsson, “30 Gbps 4-PAM transmission over 200 m of MMF using an 850 nm VCSEL,” Opt. Express, vol. 19, no. 26, pp. B203–B208, Dec. 2011.

[83] J. Gimlett and N. Cheung, “Dispersion penalty analysis for LED/single-mode fiber transmission systems,” IEEE J. Lightw. Technol., 4(9):1381–1392, Sept. 1986.

[84] D. Cunningham, M. Nowell, D. Hanson, and L. Kazovsky, “The IEEE 802.3z worst case link model for optical physical media dependent specification,” available online http://www.ieee802.org/3/z/ public/presentations/mar1997/DCwpaper.pdf, 2013.

[85] “IEEE 802.3ae 10G Ethernet optical link budget spreadsheet,” available online http://ieee802.org/3/10G_study/public/email_ attach/All_1250v2.xls, 2013.

[86] John F. Bulzacchelli et al., “A 10-Gb/s 5-Tap DFE/4-Tap FFE Transceiver in 90- nm CMOS Technology”, IEEE J. Solid-state circuits, vol.41, No.12, Dec 2006.

[87] A. Momtaz, Member, IEEE, and Michael M. Green, Member, IEEE, "An 80 mW 40 Gb/s 7-Tap T/2-Spaced Feed-Forward Equalizer in 65 nm CMOS", IEEE journal of Solid-State Circuits, Vol. 45, No. 3, pp. 629-639, March 2010.

[88] C. Xia et al., “On the Performance of the Electrical Equalization Technique in MMF Links for 10-Gigabit Ethernet”, J. Lightw Technol., vol.23, No.6, pp.2001- 2011, June 2005.

[89] R. Gitlin and S. Weinstein, “Fractionally-spaced equalization: An improved digital transversal equalizer,” Bell Syst. Tech. J., vol. 60, no. 2, pp. 275–296, Feb. 1981.

[90] C. S. Fludger, T. Duthel, D. van den Borne, C. Schulien, E. D. Schmidt, T. Wuth, J. Geyer, E. D. Man, G. D. Khoe and H. de Waart, “Digital equalization of chromatic dispersion and polarization mode dispersion” J. Lightwave Technology, vol. 28, no. 11, pp. 1867-1875, Nov. 1980.

[91] X. Chen, S. Chandrasekhar, S. Randel, W. Gu, and P. Winzer, “Experimental quantification of implementation penalties from limited ADC resolution for Nyquist shaped higher-order QAM,” in Proc. Opt. Fiber Commun. Conf. Exhib., Anaheim, CA, 2016.

[92] I. Reed and G. Solomon, “Polynomial codes over certain finite fields,” J. Soc. Ind. Appl. Math., vol. 8, no. 2, pp. 300–304, Jun. 1960.

[93] W. Ebel and W. Tranter, “The performance of Reed-Solomon codes on a bursty-noise channel,” IEEE Trans. Commun., vol. 43, no. 234, pp. 298–306, Feb.–Apr. 1995.

[94] B. Sklar, Digital Communications: Fundamentals and Applications. Englewood Cliffs, NJ, USA: Prentice-Hall, 2001.

[95] “Investigation on Technical Feasibility of Stronger RS FEC for 400GbE,” available online:
http://www.ieee802.org/3/bs/public/adhoc/logic/dec02_14/wangx_01_1214_logic.pdf, 2014.

[96] T. Wipiejewski and T. Moriarty et al., "Gigabits in the home with plugless plastic optical fiber (POF) interconnects," Electronics System-Integration Technology Conference, Sept 2008.

[97] J. Tatum et al., "VCSEL-Based Interconnects for Current and Future Data Centers," J. Lightw. Technol. vol. 8, no. 33, 727-732, 2015.

[98] P. Pepeljugoski, et al., “Development of System Specification for Laser-Optimized 50-μm Multimode Fiber for Multigigabit Short-Wavelength LANs,’ J. Lightw. Technol., vol. 21, no.5, pp.1256-1275, May. 2003.

[99] M. B. Willemsen, et al., “Correlated fluctuations in the polarization modes of a vertical-cavity semiconductor laser,” Phys. Rev. A, vol. 60, pp. 4105–4113, 1999.

[100] J. P. Hermier, et al., ‘‘Noise characteristics of oxide-confined vertical-cavity surface-emitting lasers,’’ IEEE J. Quantum Electron. no. 37, 87–91, 2001.

[101] K. Szczerba, et al., “30 Gbps 4-PAM transmission over 200 m of MMF using an 850 nm VCSEL,” Optics Express, vol. 19, no. 26, pp. B203–B208, Nov. 2011.

[102] K. Szczerba, P. Westbergh, M. Karlsson, "60 Gbits error-free 4-PAM operation with 850 nm VCSEL". Electronics Letters, vol. 49(15), pp. 953-955, 2013.

[103] Y. Sun et al., "51.56 Gb/s SWDM PAM4 Transmission over Next Generation Wide Band Multimode Optical Fiber," in Optical Fiber Communication Conference, OSA Technical Digest. [online] (2016), paper Tu2G.3.

[104] R. Motaghian et al., "180 Gbps PAM4 VCSEL Transmission over 300m Wideband OM4 Fibre," in Optical Fiber Communication Conference, OSA Technical Digest. [online]. (2016), paper Th3G.2.

[105] J. Lavrencik, et al., “Error-Free 100Gbps PAM-4 Transmission over 100m Wideband Fiber Using 850nm VCSELs," European Conference on Optical Communication (ECOC), Göteberg, Sweden, 2017.

[106] D. Kutcha, A. Rylyakov, C. Schow, J. Proespel, F. Doany, C. W. Baks, B. H. Bissell, C. Kocot, L. Graham, R. Johnson, G. Landry, E. Shaw, A. MacInnes, and J. Tatum, “A 56.1Gb/s NRZ Modulated 850nm VCSEL-Based Optical Link”, OFC 2013, paper OW1B.5, 2013.

[107] J. D. Ingham, P. Westbergh, and A. Larsson, “32Gb/s Multilevel Modulation of an 850nm VCSEL for Next Generation Data communication Standards”, CLEO 2011, paper CWJ2, 2011.

[108] K. Szczerba, et al., “Intersymbol Interference Penalties for OOK and 4-PAM in Short-range Optical Communications”, Proc. Optical Fiber Communication (OFC/NFOEC) Conf., March 2013.

[109] H. Li and K. Iga, “Vertical-Cavity Surface-Emitting Laser Devices”, Springer-Verlag Berlin Heidelber 2003, ISBN: 978-3-642-08743-1.

[110] The IEEE 802.3z Worst Case Link Model for Optical Physical Media Dependent Specification, IEEE 802.3z Task Force, Jan. 1997.

[111] S. Varughese et al., “Raise cosine pulse shapes for next generation MMF links,” in Proc. IEEE Photon. Conf., Waikoloa, HI, USA, 2016, pp. 825–826.

[112] P. Khandelwal et al., “100Gbps dual-channel PAM-4 transmission over datacenter interconnects,” in Proc. DesignCon, CA, USA, Jan. 2016, W. 3F.

[113] J. Lavrencik, S. K. Pavan, A. Melgar, and S. E. Ralph, “Direct measurement of transverse mode correlation and fiber-enhanced RIN through MMF using 850 nm VCSELs,” in Proc. Opt. Fiber Commun. Conf., Anaheim, CA, 2016.

[114] M. Oerder and H. Meyr, “Digital filter and square timing recovery,” IEEE Trans. Commun., vol. 36, no. 5, pp. 605–612, May 1988.

[115] S. K. Pavan, “50 Gbit/s PAM-4 MMF transmission using 1060 nm VCSELs with reach beyond 200 m,” in Proc. Opt. Fiber Commun. Conf., San Francisco, CA, 2014.

[116] P. Westbergh. et al., "High-speed 850 nm VCSELs operating error free up to 57 Gbit/s". Electronics Letters, V. 49(16), pp. 1021-1022 (2013).

[117] D. M. Kuchta et al., "A 71-Gb/s NRZ Modulated 850-nm VCSEL-Based Optical Link," IEEE Photonics Technology Letters, V. 27, n. 6, pp. 577-580, March, 15 2015.

[118] C. Kottke, et al., "High Speed 160 Gb/s DMT VCSEL Transmission Using Pre-equalization," Optical Fiber Conf., W4I.7, Los Angeles CA, 2017.

[119] P. Westbergh, et al., “High-speed 850 nm VCSELs with 28 GHz modulation bandwidth operating error-free up to 44 Gbit/s,” Electron. Lett., V. 48, n. 18, pp.1145-1147, 2012.

[120] P. Westbergh, et al., “Impact of photon lifetime on high-speed VCSEL performance,” IEEE J. Sel. Top. Quantum Electron., V. 17, n. 6, pp.1603-1613, 2011.

[121] “The Need for 100Gb/s lane MMF PMDs,” [Online]. Available: http://www.ieee802.org/3/NGMMF/public/Jan1 8/ghiasi_NGMMF_01_jan18.pdf, Jan. 18, 2018.

[122] E. Simpanen et al., "1060 nm Single and multimode VCSELs for up to 50 Gb/s modulation," 2017 IEEE Photonics Conference, Orlando, FL, 2017, pp. 65-66.

[123] K. Szczerba et al., "Energy Efficiency of VCSELs in the Context of Short-Range Optical Links," IEEE Photonics Technology Letters, vol. 27, no. 16, pp. 1749-1752, Aug.15, 15 2015.

[124] S. Varughese et al., “Polybinary Coding for Low Complexity High Speed Error-Free VCSEL-MMF Links,” ECOC, Göteborg, Sweden, Sept. 2017.

[125] K. Szczerba et al., “4-PAM for High-Speed Short-Range Optical Communication,” Journal of Optical Communications Networks, vol. 4, no. 11, pp. 885-894, November 2012.

[126] R. Shubochkin et al., “Next Generation wideband multimode fiber for shortwave wavelength division multiplexing in datacom links,” International Cable & Connectivity Symposium (IWCS), Atlanta GA, 2015.

[127] “50 Gb/s, 100 Gb/s, and 200 Gb/s Ethernet Task Force.” [online]. http://www.ieee 802.org/3/cd/index.html.

[128] D. Kuchta et al., "64Gb/s transmission over 57m MMF using an NRZ modulated 850nm VCSEL," Optical Fiber Communications Conference and Exhibition (OFC), 2014, San Francisco, CA, 2014.

[129] F. Karinou et al., “112 Gb/s PAM-4 Optical Signal Transmission over 100m OM4 Multimode Fiber for High-Capacity Data-Center Interconnects,” European Conference on Optical Conference (ECOC), 2016, Düsseldorf, Germany, M.2.C.3.

[130] J. Im et al., "A 40-to-56Gb/s PAM-4 receiver with 10-tap direct decision-feedback equalization in 16nm FinFET," 2017 IEEE Intern. Solid-State Circuits Conference (ISSCC), San Francisco, CA, 2017, pp. 114-115.

[131] IEEE 802.3cm, “400 Gb/s over Multimode Fiber Task Force,” http://www.ieee802.org/ 3/cm/public/index.html.

[132] K. Balemarthy et al., “Next-generation wideband multimode fibers for data centers,” SPIE OPTO, San Francisco, CA, United States, 2016.

[133] J. Lavrencik et al., "Scaling VCSEL-MMF Links to 1 Tb/s Using Short Wavelength Division Multiplexing," JLT, V. 36(18), Sept.15, 2018.

[134] J. Castro, R. Pimpinella, B. Kose et al., "Investigation of 60 Gb/s 4-PAM Using an 850 nm VCSEL and Multimode Fiber," IEEE Journal of Lightwave Technology, vol. 34, no. 16, pp. 3825-3836, Aug. 15, 2016.

[135] N. Haghighi, G. Larisch, R. Rosales et al., "35 GHz Bandwidth with Directly Current Modulated 980 nm Oxide Aperture Single Cavity VCSELs," Proc. 2018 IEEE International Semiconductor Laser Conference (ISLC), Santa Fe, NM, 2018.

[136] D. M. Kuchta, "High capacity VCSEL-based links," Proc. Optical Fiber Conf. (OFC), Los Angeles, CA, 2017.

[137] M. Rakowski et al., “Hybrid 14nm FinFET - Silicon photonics technology for low-power Tb/s/mm2 optical I/O,” Proc. Symp. VLSI Technol., Honolulu, HI, USA, Jun. 2018, p. 221–222.

[138] U. Hecht et al., “120Gbit/s multi-mode fiber transmission realized with feed forward equalization using 28GHz 850nm VCSELs,” ECOC, Ireland, 2019.

[139] N. Ledentsov et al., "Anti–waveguiding vertical–cavity surface–emitting laser at 850 nm: From concept to advances in high–speed data transmission." Optics Express, v. 26, no. 1 (2018), p. 445-453.

[140] N. Ledentsov Jr. et al, "Energy efficient 850-nm VCSEL based optical transmitter and receiver link capable of 56 Gbit/s NRZ operation," Vertical-Cavity Surface-Emitting Lasers XXIII, vol. 10938, p. 109380J. International Society for Optics and Photonics (SPIE), 2019.

[141] H.J. Unold et al., “Single-mode VCSELs”, SPIE, 2002.

[142] G. Stepniak et al., "54 Gbit/s OOK transmission using single-mode VCSEL up to 2.2 km MMF," Electronics Letters, v. 52, n. 8, 2016.

[143] Kangmei Li et al., "High data rate few-mode transmission over graded-index single-mode fiber using 850 nm single-mode VCSEL," Opt. Express, 27, 21395-21404, 2019

[144] S. M. R. Motaghiannezam et al., "51.56 Gbps PAM4 Transmission over up to 2.3 km OM4 Fiber using Mode Selective VCSEL," OFC, San Diego, 2018.

[145] N. Ledentsov et al., "850 nm single-mode VCSEL for error-free 60 Gbit/s OOK operation and transmission through 800 m of multi-mode fiber," OFC, San Diego, 2019.